X-ray Reflectivity Studies of Solid Supported Model Biomembranes

DISSERTATION

zur Erlangung des akademischen Grades

Doktor der Naturwissenschaften

(Dr. rer. nat.)

vorgelegt von

M. Sc. (Hons.) Monika Khurana

Geboren am 03.08.1979

In Muktsar, Indien

eingereicht beim

Fachbereich Chemie

der Universität Dortmund

Dortmund 2006

Erstgutachter:	Prof. Dr. R. Winter
Zweitgutachter:	Prof. Dr. J. P. Pohl
Tag der mündlichen Prüfung	29.03.06

Acknowledgments

First and foremost, I would like to thank my supervisor Prof. Dr. R. Winter for his constant support and guidance throughout my PhD work. It is indeed an honor to have carried out my doctoral research under his supervision. I am also thankful to him for introducing me to the field of model biomembranes.

My special thanks to Dr. C. Czeslik for creative guidance, invaluable help and friendly discussions during the work. He has been the best teacher and role model I could hope for.

I thank Prof. J. P. Pohl and Dr. C. Czeslik for being in my examination committee.

I wish to thank Dr. O. Seeck (HASYLAB, Hamburg) and Dr. T. Geue (Paul Scherrer Institute, Switzerland) for giving me the permission to perform my experiments at their beamlines and help for the data evaluation.

I thank Prof. P. L.-G. Chong, (Department of Biochemistry, Temple University School of Medicine, Philadelphia, Pennsylvania, USA) for providing the PLFE lipid.

I am also grateful to my teachers Dr. P. Venugopalan and Prof. H. Singh for their helpful guidance during my early stages of the research work.

I would like to thank Mechanical workshop people for their help in the construction of the sample cell for X-ray reflectivity measurements.

I would like to thank especially, in no particular order, Supriya Subramanian, Berti Schuppan, Karsten Vogtt, Dr. Guido Jackler, Raghunadha Reddy Burri, Gurpreet Singh, Ewa Powalska, Nagarajan Periasamy, Vytautus Smirnovas, Nadeem Javid, for their kind help. Special thanks to Karsten Vogtt for writing Zusammenfassung.

I thank all the staff members of the Physical Chemistry I department for their kind assistance.

I wish to thank Dr. J. Roetter for her support and International Max-Planck Research School for the financial assistance.

Last but not the least, I owe my immense gratitude to my parents and family members for their continuous support, blessings and their encouragement throughout my research work.

Table of Contents

1 Introduction 1

2 Lipid Membranes 5

2.1 The Structure and Properties of Membrane Lipids 6

3 Basic Principles of X-ray Reflectivity 12

3.1 Reflectometry 12
3.1.1 The Index of Refraction 13
3.1.2 The Critical Angle of Reflection 14
3.2 Direct Analysis of X-ray Reflectivity Patterns for Biomembrane Systems 15
3.2.1 An Estimation of Thickness 15
3.3 Reflectivity Calculations 16
3.3.1 Reflectivity from an Ideal Surface: Fresnel Reflectivity 16
3.4 Reflectivity from Ideal Interfaces 17
3.4.1 Definitions 17
3.4.2 Fresnel Reflectivity from a Single Layer 18
3.4.3 Fresnel Reflectivity from a Multilayer 18
3.5 Differential Scanning Calorimetry and Pressure Perturbation Calorimetry (DSC/PPC) 19
3.5.1 Basics of Differential Scanning Calorimetry (DSC) and Pressure Perturbation Calorimetry (PPC) 21
3.5.2 Lipid-Phase Transitions 22

4 Experimental Data 24

4.1 Materials and Sample Preparation 24
4.2 X-ray Reflectivity Experiments 26
4.3 Preparation of Samples for X-ray Reflectivity Measurements 26
4.3.1 Cleaning of Substrates 26
4.3.2 Bilayer Deposition 26
4.3.3 Sample Environment 27
4.4 Differential Scanning and Pressure Perturbation Calorimetry 28
4.4.1 Differential Scanning Calorimetry (DSC) 28
4.4.2 Pressure Perturbation Calorimetry (PPC) 28
4.5 Preparation of Samples for DSC and PPC Measurements 29
4.5.1 Isolation and Purification of PLFE Lipid 29
4.5.2 PLFE Liposomes 29
4.5.3 Lipid Raft Liposomes 30
4.6 Fourier-Transform Infrared Spectroscopy (FT-IR) 30
4.6.1 Sample Preparation 30
4.7 Small-Angle Neutron Scattering (SANS) 31
4.7.1 Sample Preparation 31
4.8 Set-up for X-ray Reflectivity Measurements 33

4.8.1 Sample Chamber 35
4.9 X-ray Reflectivity Measurements at the In-house Diffractometer 37
4.10 Measurements at Synchrotron HASYLAB/DESY in Hamburg 38
4.11 Measurements at the Spallation Neutron Source in Switzerland 40

5 Results and Discussion 44

5.1 One Component System DPPC 44
5.2 Archaebacterial Lipid PLFE 52
5.2.1 X-Ray Reflectivity Measurements 54
5.2.2 DSC and PPC Measurements 60
5.2.3 DSC Thermograms Measured at pH 7.0 for PLFE MLVs Derived From Cells Grown at 65 °C 61
5.2.4 PPC Scans Measured at pH 7.0 and 2.1 for PLFE MLVs Derived from Cells Grown at 65 °C 62
5.2.5 Temperature Dependence of Thermal Expansion Coefficient (α) in PLFE MLVs 64
5.2.6 DSC Thermograms Measured in Pure Water for PLFE MLVs Derived from Cells Grown at 65 °C 66
5.2.7 PPC Scans Measured in Pure Water for PLFE MLVs Derived from Cells Grown at 65 °C 68
5.2.8 Temperature Dependent FT-IR Spectroscopic Measurements of PLFE in D_2O 71
5.3 The Two Component System DPPC/Ergosterol 74
5.3.1 X-ray Reflectivity Measurements 75
5.3.2 Small-Angle Neutron Scattering (SANS) Experiments 80
5.4 The Three component System POPC/SM/Chol ("Lipid Raft" Mixture) 90
5.4.1 X-ray Reflectivity Measurements 92
5.4.2 Differential Scanning and Pressure Perturbation Calorimetry (DSC/PPC) 94
5.4.3 Comparison of DSC and PPC Data of Ternary Raft Mixtures Containing an Equimolar Mixture of POPC/SM/Chol and DOPC/SM/Chol 97
5.4.4 The Effect of Gramicidin D Incorporation 98

6 Summary 100

7 Zusammenfassung 103

8 References 107

List of Abbreviations

Chol	Cholesterol
$CHCl_3$	Chloroform
CH_3OH	Methanol
DOPC	1, 2-Dioleoyl-*sn*-Glycero-3-Phosphocholine
DPPC	1, 2-Dipalmitoyl-*sn*-Glycero-3-Phosphocholine
DPPC-d_{62}	1, 2-Dipalmitoyl-d_{62}-*sn*-Glycero-3-Phosphocholine
DSC	Differential Scanning Calorimetry
ergo	Ergosterol
GD	Gramicidin D
l_o	Liquid-Ordered
l_d	Liquid-Disordered
MLVs	Multilamellar Vesicles
mol%	Mole Percent
NMR	Nuclear Magnetic Resonance
PLFE	Polar Lipid Fraction E
POPC	1-Palmitoyl-2-Oleoyl-*sn*-Glycero-3-Phosphocholine
PPC	Pressure Perturbation Calorimetry
RH	Relative Humidity
RPM	Revolutions per Minute
SANS	Small-Angle Neutron Scattering
SAXS	Small-Angle X-ray Scattering
Si	Silicon
SM	Sphingomyelin (Brain Porcine)
s_o	Solid-Ordered
TFE	Trifluoroethanol
ULVs	Unilamellar Vesicles
v/v	Volume by Volume
wt%	Weight percent
XRR	X-Ray Reflectivity

1 Introduction

Cells and sub-cellular components such as nuclei and mitochondria are confined by their surrounding surfaces; these surfaces are biological membranes. The integrity and characteristic features of these vital components are to a large extent preserved and protected by these membranes. Though they are restrictive in nature, their basic structure permits the transport of essential components across the membrane in both ways, often controlled by concentration or charge gradient or both from the exterior to the interior. The basic structure common to all biological membranes is the lipid bilayer. These membranes are composed of a two-dimensional lipid bilayer supporting peripheral and integral proteins.

Though the basic structural features are common to all biological membranes, the subtle variations in their structure and composition makes each of them unique to the cellular component to which it is associated. Understanding the exact details of a specific structure and its variations from others (both similarities and differences) are extremely important to delineate their specific mode of activity. Such an endeavour becomes often complex and elaborate and one generally resorts to relatively simple model systems. In this context supported planar lipid membranes have attracted much attention since they can provide a model system for investigating the properties and functions of a cell membrane. For example, lipid membranes are useful models to gain insight into the processes occurring at the cell membrane such as molecular recognition and signal transduction [Sackmann 1996]. Apart from the role that lipid bilayers play in the organization of the biological cells, they are also expected to become a key component of novel bio-molecular materials. In particular, solid supported lipid bilayers may provide a way to biofunctionalize solid state and semiconductor surfaces, providing a compatible interface between the inorganic and biomolecular world.

The most extensive and reported systems to study membrane physical interactions are multilamellar vesicles in aqueous medium and characterization of these bulk studies were mainly done by various techniques such as calorimetry, SAXS, flourescence spectroscopy, and NMR.

In our studies, stacks consisting of hundreds of bilayers deposited on solid silicon substrates and hydrated by contact with water vapor have allowed more detailed structural studies since the broad orientation distribution that is present in multilamellar vesicles is suppressed.

Solid supported membranes are of contemporary interest because these membranes can be used as biomimetic systems to study the structure as well as various biochemical and biophysical aspects of interaction between membranes and membrane-active biomolecules under well-controlled conditions [Sackmann 1996]. These membranes with incorporated receptors also have a great potential in biosensor applications.

It is well known that other complementary methods like various kinds of scanning tunnelling (STM), atomic force (AFM), and high resolution transmission electron (TEM) microscopy are used to characterize biomembranes, in almost all cases it is quite useful to investigate surfaces with such complementary probes. For the particular case of liquid surfaces or buried layers, scattering methods have clear advantages over microscopic techniques (AFM, TEM etc). X-ray scattering from solid surfaces can be explained quantitatively by a rather simple kinematical scattering theory whereas other techniques need a complex dynamical treatment [Tolan 1999]. Hence, to characterize solid supported membranes, X-ray reflectivity is used as a major tool in our studies. X-ray reflectivity is a unique probe to obtain structural information. With X-ray scattering we can investigate surfaces on Angstrom scales. Using this method, even complex multilayer structures can be investigated and characterized with high accuracy.

Supported membranes are self-assembling two-dimensional (2D) fluid systems; the bilayer membrane consists of two opposed leaflets of phospholipids molecules and is the basic structure, central to all living cell membranes. Bilayers on solid supports were originally developed for studies of interactions between living cells, where they have proven highly useful [McConnell 1986, Watts 1987].

The preparation and characterization of solid-supported bilayers is therefore of great importance. There are several methods of preparing solid-supported lipid bilayers

[Brian 1984, Tamm 1985]. The commonly used methods to prepare lipid bilayers are the Langmuir Blodgett technique [Tamm 1985, Merkel 1989, Fragneto 2001] and vesicle fusion [Brian 1984, Kalb 1992] on an appropriate hydrophilic surface such as oxidized silicon [Brian 1984, Sackmann 1996]. The interactions between membranes and the surface involve electrostatic and hydration forces as well as attractive contributions from long-range Van der Waals forces. Supported bilayers are typically separated from the solid substrate by a thin (~ 10-20 Å) film of water [Bayerl 1990, Koenig 1996] and retain many of the properties of free membranes, including lateral fluidity. The fluidity is long range, with mobile components of both leaflets of the bilayer freely diffusing over the entire surface of the substrate.

The disadvantage of using these methods is the formation of only a monolayer or a single supported bilayer. We use the method of spreading by organic solution [Seul, 1990] and spin coating [Mennicke 2002] to deposit lipid bilayers on a silicon surface. The advantage of these methods over the first one is to get a stack of bilayers in hundreds. With spin coating, well-aligned and controlled number of lipid bilayers can be obtained depending, upon on the concentration of the lipid solution and rotational frequency of the spin coater. The advantage in getting multilayers is to obtain more detailed structural aspects of each molecule.

Such thick-stacked multibilayers have the drawback that only the properties arranged over hundreds of bilayers can be determined. On the other hand, single adsorbed bilayers interact strongly with the substrate. For a detailed investigation of this system, a compromise could be the formation of only few bilayers that are likely to be more stable in bulk water and are sufficiently thin that the characteristics of each bilayer can be determined separately, e.g. their structure with Å resolution, by techniques like X-ray reflectivity. Compared to single supported bilayers, multilamellar arrangements may also provide important advantages in some applications. If functional proteins are incorporated, the yield is sensing, catalytic, light harvesting or drug delivery applications that in most cases can be expected to vary linearly with the volume of the bilayers. The interaction of the phospholipids of lipid membranes with water is critical to the formation, maintenance, and function of

each of these important biological complexes. So the studies were carried out at different relative humidity levels and at different temperatures to get an insight into the thermal properties of phospholipid molecules by X-ray reflectivity.

Our studies reported in this thesis contribute towards identifying optimal conditions for the formation of model membranes on solid supports. The results can provide a useful membrane model for studying biomolecular interactions that occur at the cell membrane. Furthermore, with additional developments, the membranes used in the studies may have potential as biosensor surfaces. In all the investigations, solid supported biomembranes have been used as model systems to enhance our understanding of the structure-function relationships of cell membranes.

In this work, measurements have been performed using specular reflectivity of one component system (e.g. 1, 2-Dipalmitoyl-*sn*-Glycero-3-Phosphocholine, DPPC), two-component systems (e.g., 1, 2-Dipalmitoyl-*sn*-Glycero-3-Phosphocholine, DPPC and Ergosterol), three-component systems (1-Palmitoyl-2-Oleoyl-*sn*-Glycero-3-Phosphocholine, POPC, Sphingomyelin (Brain, Porcine) and Cholesterol) and on archaebacterial lipid PLFE (polar lipid fraction E) derived from thermoacidophilic archaeon *Sulfolobus acidocaldarius* on silicon substrates. Depending on the temperature and water contents, lipid membranes undergo different lyotropic phase transitions. Therefore, the samples were kept in a hydration and temperature controlled chamber during the measurement; the sample chamber will be described in the next chapter. The X-ray reflectivity measurements were carried out at an in house X-ray diffractometer and at the wiggler beamline W1.1 of HASYLAB/DESY in Hamburg. The reflectivity curves obtained contain a lot of information also between the Bragg peaks and are sometimes difficult to analyse in detail. The difficulty arises from intermembrane potentials, fluctuations, interactions with the substrate and the surrounding air, which results in an asymmetry of the profile in the membrane stack which is invisible in thick samples and dominating in single membrane systems. Detailed analysis of the curves has been performed successfully on stacks of DPPC bilayers at different relative humidity levels.

2 Lipid Membranes

The membrane surrounding of the living cell serves several functions, such as control of solute permeability and recognition events. These membranes are composed of a two-dimensional lipid bilayer supporting peripheral and integral proteins. In 1972, Singer and Nicholson, [Singer 1972] presented a fluid mosaic model of the cell membrane which showed the membrane as a fluid-like bilayer in which proteins are able to move freely (Fig. 2.1). The authors proposed that the main part of the lipid bilayer is neutral and a passive solvent that has little influence on membrane protein functions, while there was a small portion of specific lipids that might be more tightly coupled to the protein. It is now clear that this lipid environment has a major effect on recognition events taking place at the cell membrane.

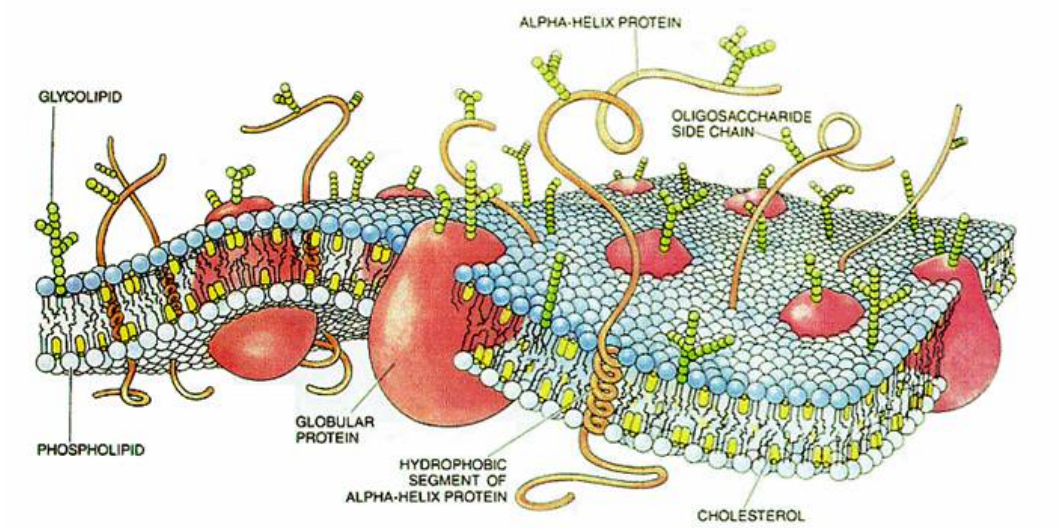

Figure 2.1: A Schematic picture of the cell membrane composed of a lipid bilayer and integral proteins.

Studies using model membranes have shown that lipids surrounding receptor molecules have a profound effect on the interaction between biomolecules [Crook 1986, Stewart 1993]. For example, lipids of increasing chain length decrease the binding capacity and may affect the exposure of binding moieties.

Many interactions at the cell membrane occur through polyvalent binding. This complex binding with several binding sites involved simultaneously, require flexible interacting molecules. It is now evident that microdomains, which consist of a unique protein and lipid composition, known as lipid rafts, exist in the plasma membrane of almost all mammalian cells as well as in model membranes [Tillack 1982, Simons 2000, Harder 2003, Pike 2003]. These microdomains contain, for instance, a large number of molecules that are involved in specific interactions which mediate signal transduction. These rafts can change in size and composition as a response to intra- or extracellular stimuli and can regulate the signaling cascade.

2.1 The Structure and Properties of Membrane Lipids

Lipids are amphiphilic molecules, which consist of a polar head group and an attached hydrophobic hydrocarbon chain (Fig. 2.2). In an aqueous solution, these molecules spontaneously assemble with their hydrophilic part in contact with water and their hydrophobic part in the interior of the structures, as in bilayers and micelles. The forces that hold these structures together are weak van der Waals, hydrophobic, hydrogen-bonding and electrostatic interactions. The weak nature of these forces also makes them flexible. It is the geometric properties of the molecules such as the volume of the hydrocarbon chain, chain length and the optimal area of the polar headgroup that determines which structure the molecules can assemble into. Single chain amphiphilic molecules form micelles because of the relatively large polar head when compared to the non-polar tail. Reverse micelles can be formed if the polar head is smaller compared to the non-polar section, and a bilayer is formed if the geometry of the lipids is cylindrical, such as, for phosphatidylcholines [Cevc 1993].

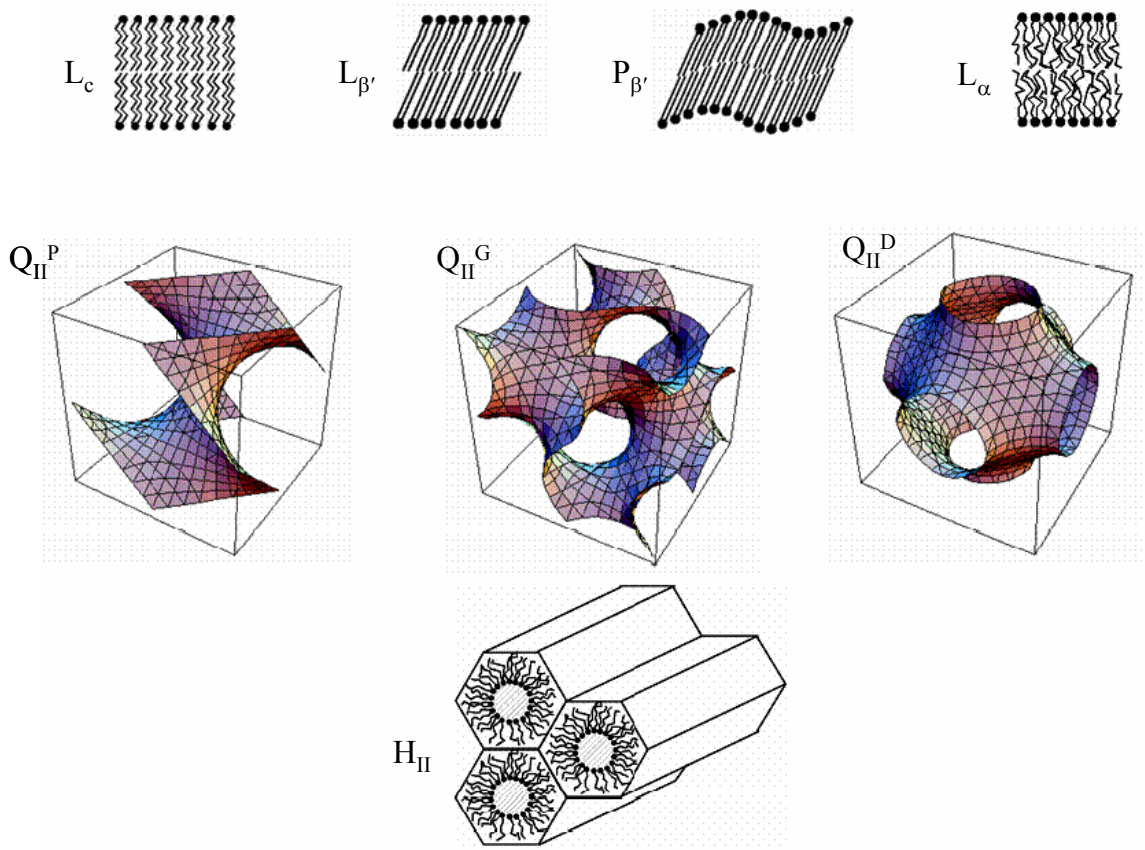

Figure 2.2: A schematic drawing of lipid-water phases (L_c, lamellar crystalline; $L_{\beta'}$, $P_{\beta'}$, lamellar gel; L_α, lamellar liquid crystalline; Q_{II}^G, Q_{II}^D, Q_{II}^P, inverse bicontinuous cubics; H_{II}, inverse hexagonal). The cubic phases are represented by the G, D and P minimal surfaces, which locate the mid-planes of fluid lipid bilayers (adapted from [Winter 2004]).

These structures are sensitive to changes in the surrounding medium, such as pH, ionic strength and temperature, which can affect the intermolecular forces in these structures resulting in a modification of their size and shape [Israelachvili 1992]. Eukaryotic cellular membranes consist of a variety of lipid molecules, which provide a permeability barrier between the exterior and interior of the cell and its different compartments. Phospholipid molecules are the major structural components of most membranes, including phosphatidylcholine (PC), phosphatidylethanolamine (PE), phosphatidylserine (PS) and phosphatidylinositol (PI) [Vance 1996]. These molecules, also called glycerophospholipids, consist of a phosphate-containing head group with saturated or unsaturated hydrocarbon chains connected to a glycerol via ester bonds (Fig. 2.3).

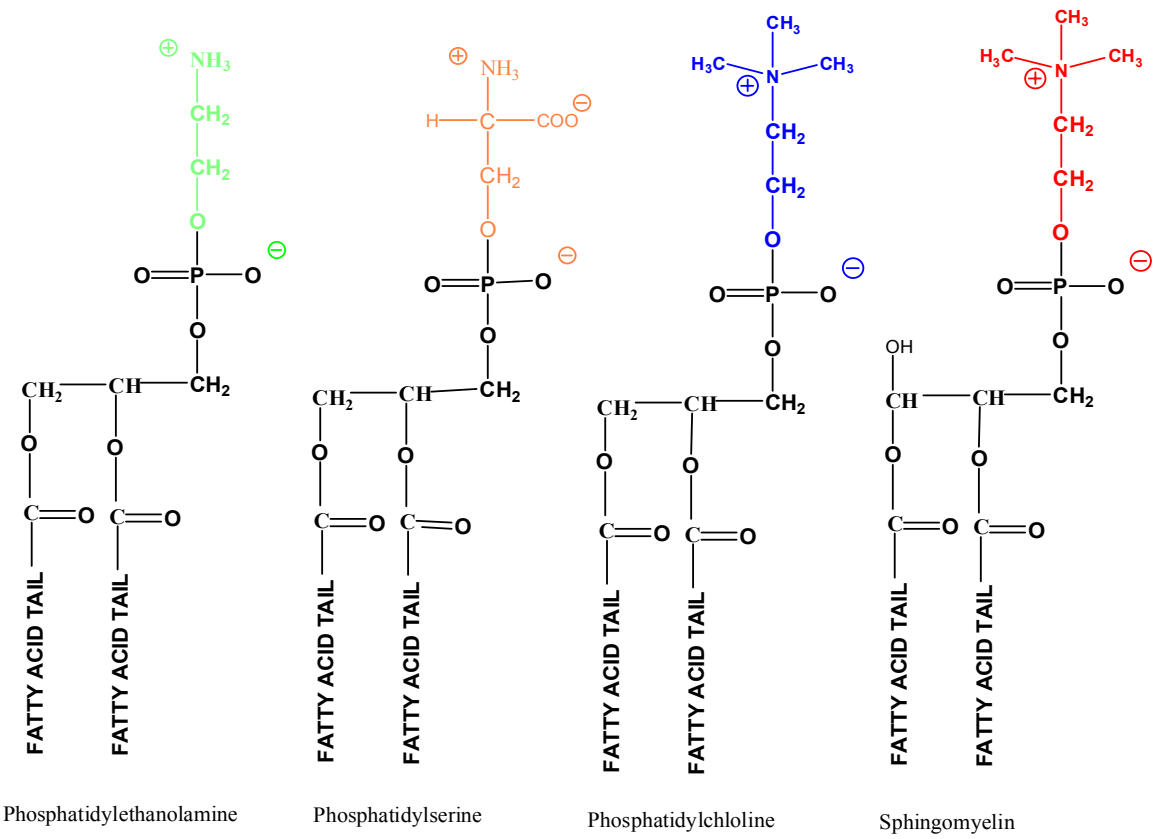

Figure 2.3: Four major phospholipids in mammalian plasma membranes. Different head groups are represented by different colors. All the lipid molecules shown are derived from glycerol except for sphingomyelin, which is derived from serine.

Glycosphingolipids, another class of lipids in the membrane, include cerebrosides and gangliosides, and in these molecules the lipid chains are attached to sphingosine instead of glycerol as in phospholipids (Fig. 2.3). Cerebrosides are neutral glycosphingolipids while gangliosides contain one or more units of the negatively charged sialic acid. Lipids within the lipid bilayer can exist in an ordered gel phase or fluid liquid crystalline phase depending on the lipids involved and the temperature. The midpoint of the gel to liquid-crystalline transition for a distinct lipid is often referred to as a melting temperature. Below this transition temperature, the hydrocarbon chains are tilted in a nearly all-*trans* conformation (Fig. 2.2) with strong contacts achieved by van der Waals forces. Above this temperature, the organisation

of the chains becomes more disordered and adopts a gauche conformation which weakens the van der Waals chain contacts. This will also change the hydration and polar interaction of the phospholipid head groups [Mason 1998]. The role of cholesterol within the membrane has been extensively studied [Scott 2002, Mason 2003, Silvius 2003]. It is known that cholesterol modifies the structure and dynamic properties of the membranes by changing the packing properties within the bilayer. In mammalian cell membranes the amount of cholesterol is relatively high, varying approximately between 20 % to 50 % [Scott 2002]. Increasing amounts of cholesterol lead to more structurally ordered membranes at temperatures above the phase transition temperature and to less ordered membranes at temperatures below phase transition. These changes are most pronounced at temperatures near the phase transition of the lipids. The interaction between cholesterol and lipids are thought to be crucial for the formation of rafts in the cell membrane. It has also been shown that cholesterol interacts more strongly with saturated high-melting phospho- and spingolipids than with the highly unsaturated lipids [Silvius 2003].

DPPC

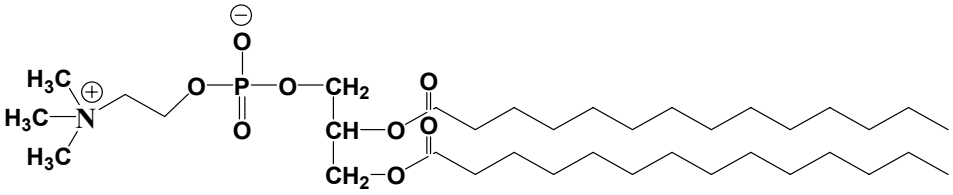

DPPC-d_{62}

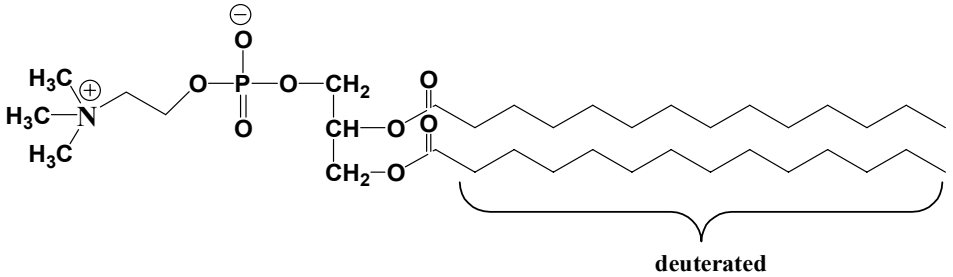

POPC

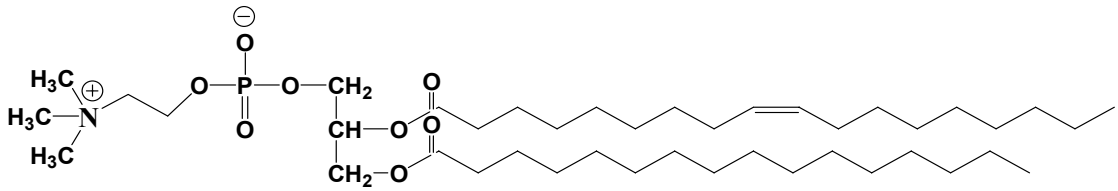

Spingomyelin (SM)

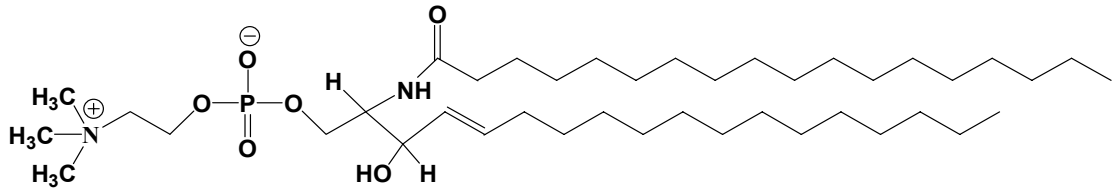

Cholesterol

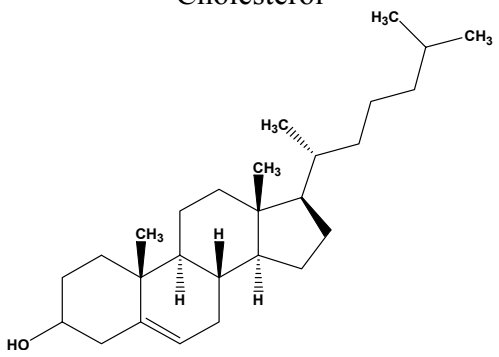

Ergosterol

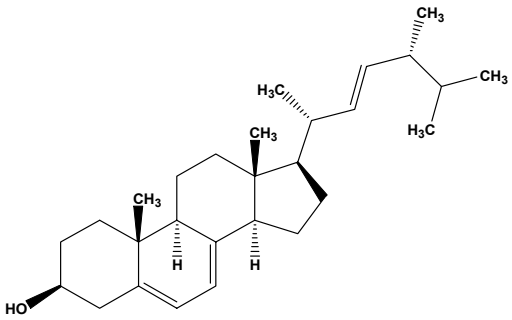

PLFE

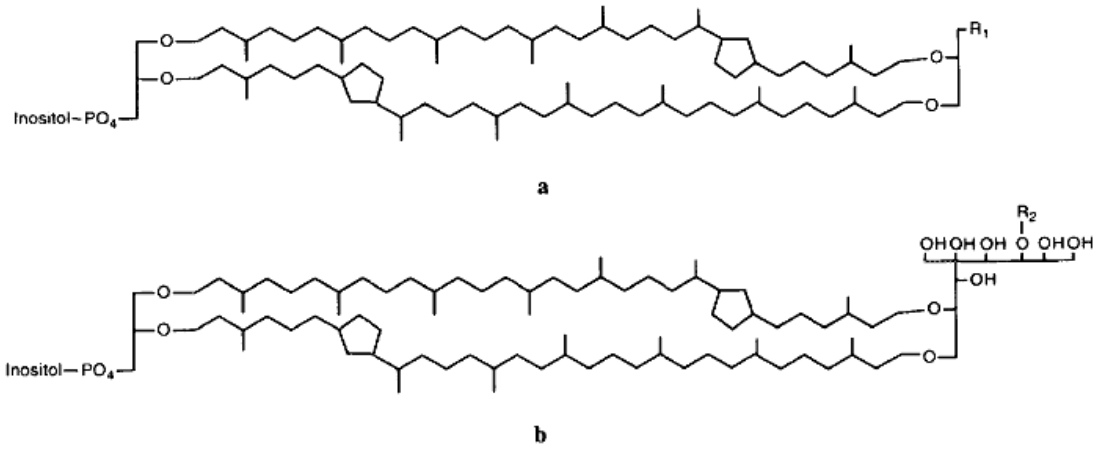

Figure 2.4: Structures of the lipids and sterol investigated in this work. The structures of PLFE consist of (a) a symmetric glycerol dialkyl glycerol tetraether (GDGT) skeleton with phosphatidylinositol on one end and R_1=β-D-glucopyranose and (b) a glycerol dialkyl nonitol tetrether (GDNT) skeleton with phosphatidylinositol on one end and R_2=β-D-galactopyranosyl-β-D-glucopyranose (adapted from [Chang 1994]).

The above mentioned lipids (Fig. 2.4), which are important components of lipid membranes are used in various experiments reported in this thesis and can act as model lipid bilayers. Once they are supported on solid supports like silicon wafers, their structural properties can be investigated by X-ray reflectivity and by other biophysical techniques. X-ray reflectivity can provide detailed information regarding their thickness, organization and interaction with proteins or peptides. The thesis reports a detailed investigation of these lipids by X-ray reflectivity, differential scanning and pressure perturbation (DSC/PPC) calorimetry, Fourier-transform infrared spectroscopy (FT-IR) and small-angle neutron scattering (SANS) techniques.

3 Basic Principles of X-ray Reflectivity

X-ray reflectivity has become an invaluable tool to study the structure and the organization of materials, which are grown as thin films at atomic scales. In recent years, several scattering techniques have been developed for probing the surface structure of materials. These include neutron and X-ray reflectometry and X-ray grazing incidence diffraction (GID). In each of these surface-sensitive scattering methods, one takes advantage of the wave properties of the probe (electromagnetic radiation or the neutron) near the condition of perfect reflection from the sample. These techniques can be successfully implemented for studying structures of organic, ultra-thin, layered molecular arrays at various interfaces with Å resolution [Russell 1990, Als-Nielsen 1994].

Structural studies of bulk, layered, polycrystalline molecular assemblies provide information about characteristic repeat distances, molecular conformations, chain packing properties, magnitude of the molecular motion or surface roughness of the layers, hydration and inter-layer arrangements [Janiak 1976, Janiak 1979].

3.1 Reflectometry

When a wave is incident on an interface between two materials in which the characteristics of propagation of the wave - the refractive indices - are different, a fraction of the wave will be reflected from the interface (Fig. 3.1). The reflectivity of a surface is defined as the ratio of the intensities of the reflected and incident beams.

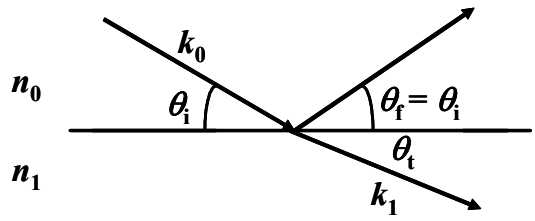

Figure 3.1: A plane electromagnetic wave with wavevector k_0 impinging on to an interface at an incidence angle θ_i. The wave splits into a reflected ($\theta_f = \theta_i$) and a refracted wave transmitted at an angle θ_t.

When measured as a function of wave vector transfer, the reflectivity curve contains information regarding the sample-normal profile of the in-plane average of the coherent scattering cross-sections.

3.1.1 The Index of Refraction

X-rays are part of the broad spectrum of electromagnetic waves. X-rays can be produced by the acceleration or deceleration of electrons in vacuum (synchrotrons) and at metallic targets (sealed tubes). The most widely used X-rays in materials science have a typical wavelength, λ, of the order of 0.1 nm. This wavelength is associated with a very high frequency of the order of 10^{19} Hz, which is at least four orders of magnitude greater than the eigen frequency of an electron bound to a nucleus. As a consequence, the interaction of X-rays with matter can be well described (in a classical way for a first approach) by an index of refraction which characterizes the change of direction of the X-ray beam when passing from air to a material. Consider a plane wave travelling in medium 0 incident on the surface of medium 1 (Fig. 3.1); the associated wave vectors in each medium are k_0 and k_1 (where $k_0 = 2\pi / \lambda$). This refractive index can commonly be written as

$$n = 1 - \delta - i\beta \tag{3.1}$$

With the dispersion term δ being

$$\delta = \left(\frac{\lambda^2}{2\pi}\right) r_e N_a \rho \left(\frac{Z + f'}{A}\right) = \left(\frac{\lambda^2}{2\pi}\right) r_e \rho_e, \tag{3.2}$$

and the absorption term β being

$$\beta = \left(\frac{\lambda^2}{2\pi}\right) r_e N_a \rho \left(\frac{f''}{A}\right) = \left(\frac{f''}{Z + f'}\right) \delta = \frac{\lambda \mu}{4\pi}, \tag{3.3}$$

where λ is the X-ray wavelength, $r_e = 2.818 \times 10^{-5}$ Å, the classical electron radius, N_a the Avogadro's number, Z the atomic number, A the atomic mass, ρ the mass density, ρ_e the electron density, μ the linear absorption coefficient, f' and f'' are real (dispersion) and imaginary (absorption) part of the dispersion corrections, respectively.

The magnitude of δ and β are simply related to the electron density of the material, and are on the order 10^{-6} to 10^{-8} [Tolan 1998].

3.1.2 The Critical Angle of Reflection

For X-rays, the refractive index of a material is slightly less than unity. Passing from air $(n_0 = 1)$ to the reflecting material $(n_1 < 1)$, it is possible to totally reflect the beam if the incident angle θ_i (which is the angle between the surface of the sample and the incident beam) is small enough. This is known as the total external reflection of X-rays. For this to occur, the incident angle must be smaller than the critical angle θ_c given as

$$\cos\theta_c = n_1 = 1 - \delta. \tag{3.4}$$

Since n_1 is very close to unity, this angle is very small and a Taylor approximation in θ_c yields

$$\theta_c^2 = 2\delta = \frac{r_e \lambda^2}{\pi} \rho_e \tag{3.5}$$

Hence, the position of the critical angle θ_c shown in Fig. 3.2 gives the average electron density of the system under study.

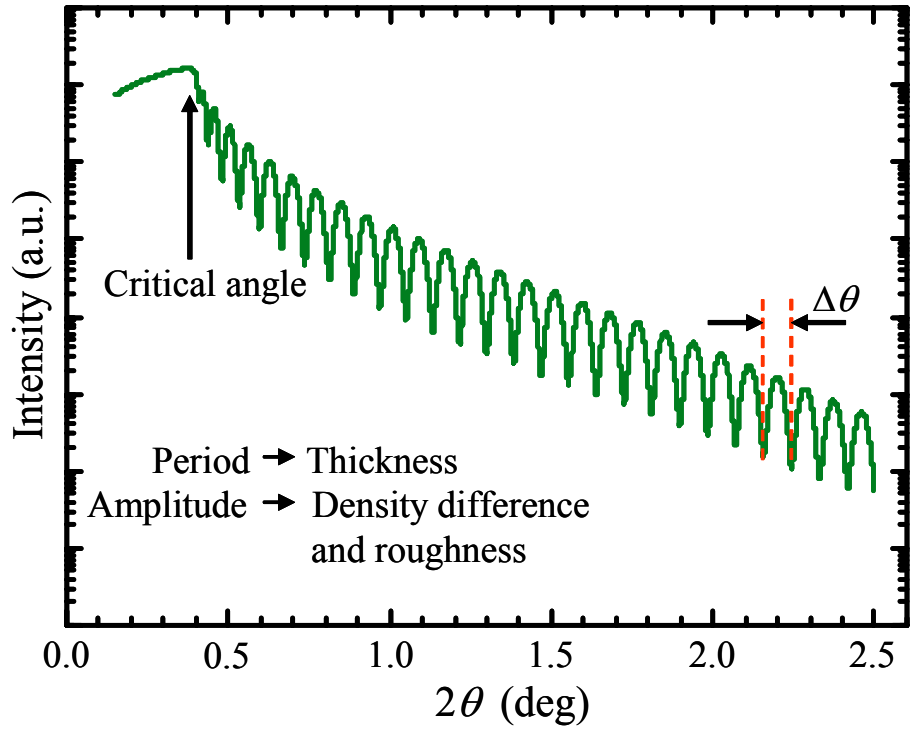

Figure 3.2: A calculated X-ray reflectivity Pattern for a 500 Å Cu layer on SiO_2 substrate (adapted from [Huang 2005]).

3.2 Direct Analysis of X-ray Reflectivity Patterns for Biomembrane Systems

3.2.1 An Estimation of Thickness

A typical X-ray reflectivity profile is shown in Fig. 3.2. This profile contains interference fringes whose period $\Delta\theta$ gives the total thickness. The roughness value of the air/film and the film/substrate interfaces can be extracted from the fitting analysis of the profile.

For a clearly identified single periodicity, the film thickness d can be roughly estimated from the fringe spacing $\Delta\theta$ at high angles ($\geq 4\theta_c$) by

$$d \approx \frac{\lambda}{2\Delta\theta} \approx \frac{2\pi}{\Delta Q}. \tag{3.6}$$

where $\Delta Q = \frac{4\pi}{\lambda}\Delta(\sin\theta) \approx \frac{4\pi}{\lambda}\Delta\theta$

3.3 Reflectivity Calculations

3.3.1 Reflectivity from an Ideal Surface: Fresnel Reflectivity

The Fresnel reflection coefficient for the interface between the air and a matter with a refractive index of $n = 1 - \delta - i\beta$ is

$$r = \frac{\theta_i - \sqrt{\theta_i^2 - 2\delta}}{\theta_i + \sqrt{\theta_i^2 - 2\delta}}, \tag{3.7}$$

where θ_i is the angle of incidence with respect to the film surface. Accordingly, the Fresnel reflectivity is given by

$$R = \left|\frac{\theta_i - \sqrt{\theta_i^2 - 2\delta}}{\theta_i + \sqrt{\theta_i^2 - 2\delta}}\right|^2. \tag{3.8}$$

For incidences at $\theta_i > 3\theta_c$ Eq. (3.8) can be approximated by

$$R \approx \left|\frac{\theta_c}{2\theta_i}\right|^4 \propto \frac{1}{\theta_i^4} \tag{3.9}$$

Therefore, at high incidence angles, the reflectivity decays as θ_i^{-4}.

3.4 Reflectivity from Ideal Interfaces

3.4.1 Definitions

For a multilayered film structure consisting of n layers, the total number of interfaces involved is $n+1$. Starting from the air/film interface (the film surface), these interfaces are labelled successively as interface 0, 1 ….. , n (Fig. 3.3).

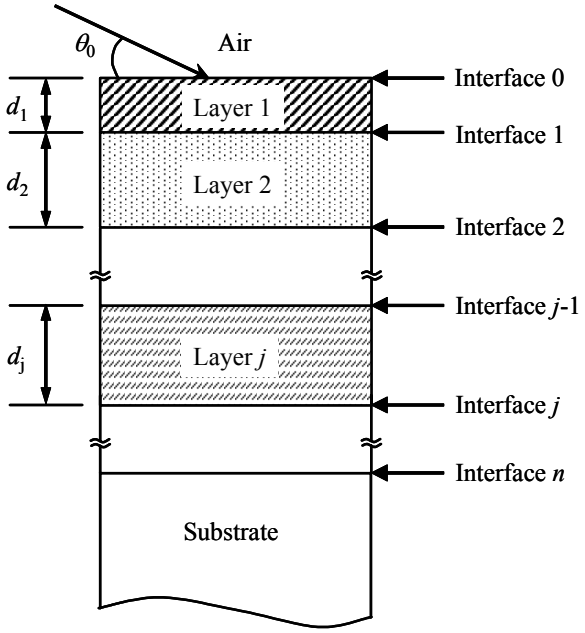

Figure 3.3: A schematic diagram showing a stack of multilayered system on Si substrate (adapted from [Huang 2005]).

Hence, layer j is bound by the interfaces $j-1$ and j, the refractive index with respect to the vacuum for the layer j is defined as n_j given by

$$n_j = 1 - \delta_j - i\beta_j. \tag{3.10}$$

The Fresnel reflection coefficient from interface j is given by [Parratt 1954]:

$$r_j = \frac{Q_j - Q_{j+1}}{Q_j + Q_{j+1}}, \qquad \text{(see Eq. (3.7))} \tag{3.11}$$

$$Q_j = n_j \frac{4\pi}{\lambda} \mathrm{Sin}\theta_\mathrm{j} \tag{3.12}$$

3.4.2 Fresnel Reflectivity from a Single Layer

The Fresnel reflectivity for a single layer bonded on a semi-infinite substrate is [Daillant 1999]:

$$R = \left| \frac{r_0 + r_1 \exp(-iQ_1 d_1)}{1 + r_0 r_1 \exp(-iQ_1 d_1)} \right|^2, \tag{3.13}$$

where r_0 is the Fresnel reflection coefficient of the free surface (air/film interface), r_1 the Fresnel reflection coefficient of the film/substrate interface, Q_1 is given by Eq. (3.12), and d_1 is the layer thickness [Holy 1999]. Note that the denominator of Eq. (3.13) differs from unity by a term which corresponds to multiple reflections in the layer [Daillant 1999].

3.4.3 Fresnel Reflectivity from a Multilayer

The reflectivity for a system having n thin layers can be obtained by a recursive method attributed to Parratt, who showed that, for an arbitrary layer j that is bound by interfaces $j-1$ and j, the total reflection coefficient at the two interfaces, r'_{j-1} and r'_j, are related to r_{j-1} by [Parratt 1954, Bahr 1993].

$$r'_{j-1} = \frac{r_{j-1} + r'_j \exp(-iQ_j d_j)}{1 + r_{j-1} r'_j \exp(-iQ_j d_j)}. \tag{3.16}$$

In Eq. (3.16), r_{j-1} and Q_j can be found from Eqs. (3.11) and (3.12), while r_j' is the total reflection coefficient at interface j, defined as the ratio of outgoing to incoming electric wave amplitudes. Note that except at the interface n (the film/substrate interface), r_j' is different from r_j in that the former is composed of the superimposed reflections from interface j and all the interfaces beneath.

The boundary condition for Eq. (3.16) is found at interface n where $r_n' = r_n$, since the substrate is semi-infinite [Parratt 1954]. Therefore, starting from $j = n$, each r_{j-1}' down to r_0' can be found by a recursive application of Eq. (3.16). The reflected intensity R measured by the detector can be found by $R = |r_0'|^2$.

For a semi-infinite substrate, Eq. (3.7) is recovered by noting $n = 0$ and $r_0' = r_0$. For a homogeneous layer bonded to a semi-infinite substrate (n = 1), it immediately follows that $r_1' = r_1$ and

$$r_0' = \frac{r_0 + r_1 \exp(-iQ_1 d_1)}{1 + r_0 r_1 \exp(-iQ_1 d_1)}. \tag{3.17}$$

Accordingly, Eq. (3.13) is recovered. The Parratt formalism possesses several notable advantages. Among them, the most remarkable one is its absence of approximations, which makes it applicable for all the scattering regions that span from less than the critical angle to high incidences [Zable 1994]. In addition, it takes into account the absorption, and can deal with an infinite number of layers ($n = 0$ to $n = \infty$) [Zable 1994].

3.5 Differential Scanning Calorimetry and Pressure Perturbation Calorimetry (DSC/PPC)

Calorimeters measure the heat consumed or released by a sample upon re-equilibration after a perturbation. Such perturbations can be caused by a change in

temperature (DSC), addition of material (ITC), a change in pressure (PPC) or in water activity (sorption calorimetry).

Differential scanning calorimetry (DSC) is used to study processes, which go along with consumption or release of energy, like phase transitions in membranes or protein denaturation. Data obtained from DSC gives us information about the thermodynamics of these processes.

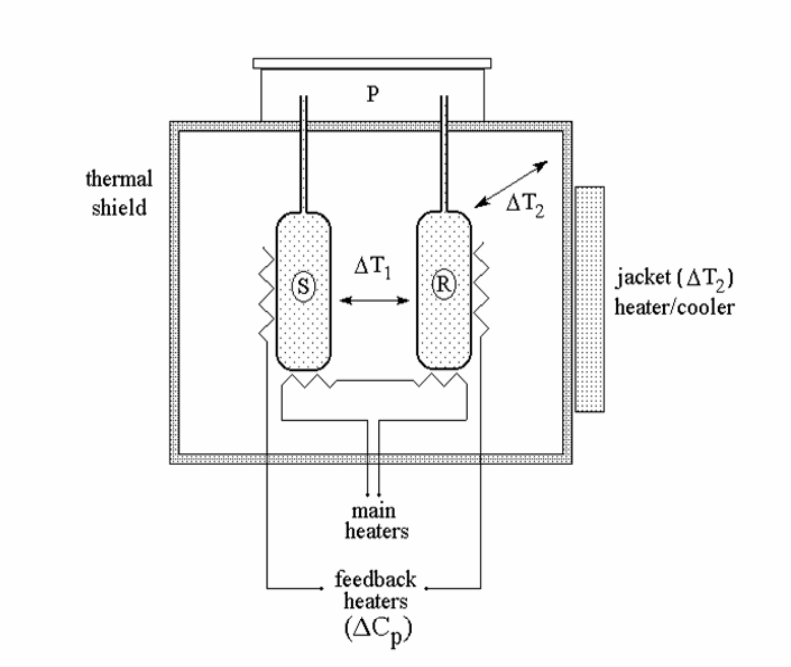

Figure 3.4: A schematic diagram of a differential scanning calorimeter

A differential scanning calorimeter (the one which is used to carry out experiments is described by [Plotnikov 1997]) consists of two coupled cells, which are isolated from the environment by adiabatic shielding (Fig. 3.4). One of these cells is filled with the sample solution and the second one with a reference substance, usually the same solution, in which the sample in the sample cell is diluted. During a DSC scan, both cells are heated simultaneously, keeping the temperature difference between the cells zero. The sample cell can take more heat or less heat according to the thermodynamic process in the sample substance [Heerklotz 2002b]. This excess heat ΔQ is measured

and recorded as a function of time *t* and temperature *T*. Using these data; one can calculate the heat capacity of the sample. The instrument used for the experiments reported in this thesis is a VP-DSC calorimeter from MicroCal (Northampton/MA USA) which has scan rates from 20-90 deg/h, a good signal to noise ratio and a stable base line. The coin-formed cells in this calorimeter are made of tantalum, which has corrosion properties similar to glass. Peltier elements are used to heat or cool the cells. This calorimeter is a very sensitive and easy to handle tool.

3.5.1 Basics of Differential Scanning Calorimetry (DSC) and Pressure Perturbation Calorimetry (PPC)

The heat of a reversible process, $\mathrm{d}Q_{\mathrm{rev},}$, is related to the entropy change, $\mathrm{d}S$, at the temperature T,

$$\mathrm{d}Q_{\mathrm{rev}} = T\mathrm{d}S. \tag{3.18}$$

Differentiation with respect to pressure, p, yields

$$\left(\frac{\partial Q_{\mathrm{rev}}}{\partial p}\right)_T = T\left(\frac{\partial S}{\partial p}\right)_T. \tag{3.19}$$

From $\mathrm{d}G = V\mathrm{d}p - S\mathrm{d}T$, it follows that

$$\left(\frac{\partial S}{\partial p}\right)_T = -\left(\frac{\partial V}{\partial T}\right)_p. \tag{3.20}$$

Eq. (3.20) can thus be rewritten as

$$\left(\frac{\partial Q_{\text{rev}}}{\partial p}\right)_T = -T\left(\frac{\partial V}{\partial T}\right)_p . \tag{3.21}$$

The thermal expansion coefficient of volume V is defined as

$$\alpha_{\text{v}} = \frac{1}{V}\left(\frac{\partial V}{\partial T}\right)_p , \tag{3.22}$$

And can thus be determined from an isothermal measurement of the heat consumed or released upon a small pressure change:

$$\alpha_{\text{v}} = -\frac{\Delta Q_{\text{rev}}}{TV\Delta p}. \tag{3.23}$$

In the present experiments, ΔQ_{rev} is the heat difference between the sample cell containing lipid in buffer, and the reference cell, containing buffer only, upon a pressure change, Δp. For the evaluation of the α_{V} of the lipid itself in lipid dispersions, the contribution of the buffer must be subtracted. This is done by the instrument software on the basis of the volume fraction of the lipid in the cell (calculated from the lipid concentration and the partial specific volume) and the temperature-dependent α_{V} of the pure buffer. The latter is determined by an additional experiment with buffer in the sample cell and water in the reference cell.

3.5.2 Lipid-Phase Transitions

Lipid-water systems are characterized by the formation of various mesophases. Transitions between these phases can be induced by temperature, lipid concentration, salt concentration, etc. The best-known example is the gel-to-liquid-crystalline (fluid) transition, observed for a large variety of synthetic lipids and studied extensively with

X-ray diffraction [Luzzati 1962, Janiak 1979, Nagle, 2000] and DSC [van Deenen 1965, Chapman 1967, de Kruijff 1972, Albon 1978, Koynova 1998].

Mesomorphic first order phase transitions are characterized by enthalpy changes, ΔH, and volume changes, ΔV. Monitoring the phase transition with DSC shows a drastic increase in the heat capacity at the phase transition. The area under the DSC peak at the phase transition yields the corresponding change in enthalpy, ΔH,

$$\Delta H = \int_{T<T_m}^{T>T_m} C_p \mathrm{d}T. \tag{3.24}$$

The relative volume change, $\Delta V/V$, can be derived analogously by measuring the thermal expansion coefficient as a function of temperature,

$$\frac{\Delta V}{V} = \int_{T<T_m}^{T>T_m} \alpha_v \mathrm{d}T. \tag{3.25}$$

Alternatively to measure ΔV, it may be obtained from the Clausius-Clapeyron equation by measuring the pressure depend shift of the phase transition temperature as described by the equation (3.26) [Anthony 1981, Landwehr 1994],

$$\frac{\mathrm{d}T_m}{\mathrm{d}p} = \frac{\Delta V}{\Delta S} = T_m \frac{\Delta V}{\Delta H}. \tag{3.26}$$

Accordingly, the temperature shift, $\Delta T_{m,}$ upon a pressure change, Δp, can be used to calculate ΔV, provided the transition enthalpy is also measured.

The DSC and PPC data in this thesis were analyzed from the above equations used by the MicroCal software provided with the instrument to calculate the enthalpy changes and the relative volume changes at the phase transitions of the lipids used in these studies.

4 Experimental Data

The experimental part described in this chapter is mainly carried out in the laboratories at the University of Dortmund and at the synchrotrons of HASYLAB/DESY in Hamburg. In this chapter, the materials and methods and the set up of the X-ray reflectivity method is explained.

4.1 Materials and Sample Preparation

Lipids: 1-palmitoyl-2-oleoyl-*sn*-glycero-3-phosphatidylcholine (POPC), 1,2-dipalmitoyl-sn-glycero-3-phosphocholine (DPPC), 1,2-dioleoyl-*sn*-glycero-3-phosphocholine (DOPC), 1,2-dimyristoyl-*sn*-glycero-3-phosphocholine (DMPC), sphingomyelin (Brain, Porcine), were purchased from Avanti Polar Lipids (Birmingham, AL), cholesterol (Chol), and gramicidin D from Sigma-Aldrich (Steinheim, Germany). The solvents and salts used for various experiments are listed below in Table 4.1. All these chemicals were used without further purification. All these chemicals are of highest purity available.

Table 4.1: The list of chemicals used and the companies they were purchased from

Chemicals	Abbreviations	Purity	Company
Calcium Chloride	$CaCl_2$	90%	Merck Darmstadt Germany
Chloroform	$CHCl_3$	>99.8%	Sigma-Aldrich Steinheim, Germany
Citric acid anhydrous	_	>99%	Sigma-Aldrich Steinheim, Germany
Doubly distilled water	H_2O	18.2 mΩcm	Elga (Siershahn, Germany)
Deuterium oxide	D_2O	>99.9 atom % D	Sigma-Aldrich Steinheim, Germany
Hydrochloric acid	HCl	37%	Sigma-Aldrich Steinheim, Germany

Chemicals	Abbreviations	Purity	Company
Hydrogen peroxide	H_2O_2	30%	Merck Darmstadt Germany
Lithium chloride monohydrate	LiCl. H_2O	>99%	Merck Darmstadt Germany
Magnesium chloride hexahydrate	$MgCl_2$. $6H_2O$	>99%	Merck Darmstadt Germany
Magnesium nitrate hexahydrate	Mg $(NO_3)_2$ $6H_2O$	>99%	Merck Darmstadt Germany
Methanol	CH_3OH	>99.9%	Sigma-Aldrich Steinheim, Germany
Potassium chloride	KCl	>99%	Merck Darmstadt Germany
Potassium Nitrate	KNO_3	>99%	Merck Darmstadt Germany
Potassium Sulphate	K_2SO_4	99%	Sigma-Aldrich Steinheim, Germany
Silicon Wafer	Si-wafer	99.9 %	Wacker Siltronic Burghausen
Sodium chloride	NaCl	>99.5 %	Sigma-Aldrich Steinheim, Germany
Sodium citrate tribasic dihydrate	_	>99.9%	Sigma-Aldrich Steinheim, Germany
Sodium deuteroxide	NaOD	99.5 atom % D	Sigma-Aldrich Steinheim, Germany
Sodium hydroxide	NaOH	98%	Sigma-Aldrich Steinheim, Germany
Sodium phosphate dibasic anhydrous	_	99%	Sigma-Aldrich Steinheim, Germany
Sulphuric acid	H_2SO_4	95-98%	Merck Darmstadt Germany
Trifluoroethanol	TFE	>99%	Merck Darmstadt Germany

4.2 X-ray Reflectivity Experiments

The X-ray reflectivity measurements presented here were carried out at the Seifert diffractometer XRD 3000 TT and at the wiggler beamline W1.1 of the synchrotron source of HASYLAB/DESY in Hamburg. The sample chamber was mounted on the *z*-axis diffractometer, and the reflected beam was measured by a position sensitive detector.

4.3 Preparation of Samples for X-ray Reflectivity Measurements

4.3.1 Cleaning of Substrates

Samples were prepared from commercially available silicon wafers having diameters of 150 mm and a thickness of approximately 0.7 mm cut into a size of about 15 × 15 mm^2. The substrates were carefully cleaned by heating at 90 °C in a mixture of 30% H_2O_2 in H_2SO_4 (30:70 v/v) for 30 min (Caution! 'Piranha solution' reacts violently with many organic solvents and can not be stored for a long time), followed by rinsing with ultrapure water (Millipore resistivity ≥ 18.2 MΩcm). After cleaning, the substrates were dried with a flow of nitrogen. They retain a high degree of hydrophilicity [Wasserman 1989].

4.3.2 Bilayer Deposition

(a) *By organic Solution Spreading*

Bilayers were deposited by pipetting 100 μL lipid solution on the desired substrate, permitting the solution to spread spontaneously and the solvent to evaporate. After the deposition, the substrates were kept in a closed chamber placing excess of solvent near the samples for 12 hours. Then the substrates were kept under vacuum for 24 hours to remove all traces of solvent.

(b) *Spin Coating*

Using the spin-coating method, a certain amount of solution (approximately 200 μL) was carefully pipetted onto the solid substrate. After spreading of the solvent onto the

whole surface, the substrate was rotated at a high frequency of 3000 rpm. During the rotation process, the solvent is evaporated, leading to purple coloured substrates with aligned lipid bilayers on it. To remove all traces of solvent, the substrates were kept 24 h under vacuum. The samples were kept refrigerated until use. The lipid and the corresponding solvents used for depositing bilayers are listed in Table 4.2.

Table 4.2: List of investigated lipid systems

Lipids	Solvent	Size of Si wafer, mm^2	Amount, µL	Rotational frequency, rpm
DPPC	TFE	15×25	100-200	3000
POPC/SM/Chol	chloroform/methanol (4:1)	15×25	100-200	3000
DPPC/Ergosterol	chloroform/methanol (4:1)	15×25	100-200	3000
PLFE	chloroform/methanol/water (4.5:4.5:1)	15×25	100-200	300

4.3.3 Sample Environment

The solid supported membranes were hydrated in a homemade temperature and humidity controlled sample cell (described in detail in section 4.8.1) with water vapor atmosphere. The sample cell consists of two parts, an inner chamber made of stainless steel and an outer chamber made of aluminium metal equipped with Mylar windows that can be cooled or heated by a flow of water connected to a temperature-controlled reservoir (Lauda Germany). The samples were mounted on a sample support made up of stainless steel inside the inner chamber of the sample cell. By placing different saturated salt solutions in the reservoir, the humidity of the sample in the sample chamber can be varied. The various salts used to vary the humidity are listed in Table 4.3, which give the relative humidity within an accuracy of ± 2% [Lide 1995]. The

temperature of the outer sample chamber is kept 3-4 degrees higher than the inner chamber to avoid the condensation of water vapors at the windows of the sample cell.

Table 4.3: Various salts and their corresponding relative humidity used in hydration dependent X-ray reflectivity measurements [Lide 1995]

Salts	Relative humidity (RH) % 25 °C
$LiCl.H_2O$	11
$MgCl_2.6H_2O$	33
$Mg\ (NO_3)_2.6H_2O$	53
NH_4Cl and KNO_3	71
NaCl	75
KCl	84
$ZnSO_4.7H_2O$	90
KNO_3	92
K_2SO_4	97

4.4 Differential Scanning and Pressure Perturbation Calorimetry

4.4.1 Differential Scanning Calorimetry (DSC)

The measurements were performed on a VP DSC calorimeter from MicroCal, (Northampton, MA). The sample cell of the calorimeter was filled with ~0.5 mL of solution of the required concentration, while the reference cell was filled with a matching aqueous solution. All the measurements were measured at a scan rate of 20 °C/h. C_p values are given with respect to the reference cell.

4.4.2 Pressure Perturbation Calorimetry (PPC)

PPC measurements were performed on the same sample after the DSC measurements, using the MicroCal pressurizing cap (Northampton, MA). A nitrogen gas pressure of

~ 5 bar was applied to the samples during all PPC cycles [Dzwolak 2003, Ravindra 2004]. The effective scan rate was 20 °C/h. Under the same experimental conditions, a set of reference sample-buffer, buffer-buffer and water-water measurements were carried out each time. For calculation of the relative volume changes, a partial specific volume of 1 cm^3 g^{-1} was used.

4.5 Preparation of Samples for DSC and PPC Measurements

4.5.1 Isolation and Purification of PLFE Lipid

S. acidocaldarius cells (strain DSM639, ATCC, Rockville, MD) were grown aerobically and heterotrophically at 65 °C, pH 2.5-3.0. PLFE lipids were isolated from *S. acidocaldarius* dry cells by Soxhlet extraction with chloroform/methanol (1:1, v/v) for 48 h [Lo 1990, Chong 2005]. In brief, the crude lipids were fractionated by reversed-phase column chromatography using C-18 PrepSep columns eluted first with methanol:water (1:1, v/v) (filtrate A) and then with chloroform:methanol:water (0.8:2:0.8, v/v/v) (filtrate B). Filtrate B was further separated by thin-layer chromatography (TLC) (PLK5 silica gel 150A, Whatman, NJ) using a mobile phase of chloroform:methanol:water (65:25:4, v/v/v). The PLFE fraction (R_f ~ 0.2) was scraped from silica TLC plates and eluted with chloroform:methanol:water (1:2:0.8, v/v/v). Finally, PLFE was purified by cold methanol precipitation 2-3 times. The PLFE lipid isolated by using above method was obtained from the lab of Prof. Dr. Parkson L.-G. Chong, Department of Biochemistry, Temple University School of Medicine, Philadelphia, Pennsylvania, USA.

4.5.2 PLFE Liposomes

PLFE liposomes were prepared by dissolving PLFE lipids in chloroform/methanol/water (65:25:10, v/v/v), vortex-mixing the solution in sealed containers and drying the solution first under a stream of nitrogen gas and then under vacuum for at least 16 h. The dried lipid was dispersed in D_2O or citrate buffer/H_2O

and the pH was adjusted to the desired value. Measurements in D_2O as solvent were carried out to compare the data with literature results from Fourier-transform infrared spectroscopic and small-angle X-ray scattering data. The hydrated mixture was heated in a closed vessel to a temperature of 70 °C and vortex-mixed for at least 5 min to yield multilamellar vesicles (MLVs). MLVs were subjected to five to six freeze-thaw cycles prior to the DSC or PPC measurements.

4.5.3 Lipid Raft Liposomes

The lipid mixtures POPC/Sphingomyelin/Cholesterol in different molar ratios were prepared by first dissolving the required amounts of lipids in chloroform/methanol (4:1). The solvent was then completely removed under vacuum using a Speed Vac Sc 110 (Savant, Farmingdale, NY, USA). The dried lipid mixture obtained was then suspended in 150 mM NaCl, 100 mM sodium phosphate buffer at pH 7.4 by gentle vortexing. Large unilammellar vesicles were produced by five freeze-thaw cycles followed by 25 passages through two stacked Nucleopore polycarbonate membranes of 100-nm pore size in a miniextruder. The samples were kept at 70 °C during the extrusion procedure.

4.6 Fourier-Transform Infrared Spectroscopy (FT-IR)

4.6.1 Sample Preparation

Infrared spectra were collected on a Nicolet 5700 Fourier-transform infrared spectrometer with a liquid-nitrogen-cooled cadmium telluride detector. For the temperature dependent FTIR experiments, a solution of 4 wt% of PLFE MLVs in D_2O was used. To prepare MLVs, first the lipid at the desired concentration was dissolved in chloroform/methanol/water (4.5:4.5:1 v/v/v). The solvent was then completely removed under vacuum using a Speed Vac Sc 110 (Savant, Farmingdale, NY, USA). The dried lipid obtained was then hydrated with D_2O and the hydrated mixture was heated in a closed vessel to a temperature of 70 °C and vortex-mixed for at least 5 min

to yield multilamellar vesicles (MLVs). MLVs were subjected to five to six freeze-thaw cycles. For conventional time-resolved FTIR spectra, CaF_2 transmission windows and 50 μm Teflon spacers were used. The temperature in the cell was controlled through an external water circuit. To achieve thermal equilibration, a 20 min wait was adopted at each new temperature before data were taken. For each spectrum, 256 interferograms were co-added, at a spectral resolution of 2 cm^{-1}. The sample chamber was purged with dry, carbon dioxide free air during data collection in order to minimize spectral contributions from atmospheric gases. From each sample's spectrum, a corresponding D_2O spectrum was subtracted. All of the data analysis, including determination of the vibrational wavenumbers was done with the OMNIC software developed by Nicolet Instruments.

4.7 Small-Angle Neutron Scattering (SANS)

4.7.1 Sample Preparation

The deuterated lipid dipalmitoyl-phosphatidylcholine (DPPC-d_{62}) was obtained from Avanti Polar Lipids (Birmingham, AL), and ergosterol (ergo) was obtained from Sigma-Aldrich (Steinheim, Germany). Lipid mixtures (10 wt% lipid dispersions) with 18 to 24 mol% of ergosterol were prepared by dissolving the appropriate weighed amounts of the two components in a mixture of chloroform:methanol (4:1). The mass of lipids taken and solvent used for the preparation of SANS samples are listed in Table 4.4. The solvent was then removed using a rotary evaporator. The dried lipid obtained was hydrated with a mixture of D_2O/H_2O as a solvent and the hydrated mixture was heated in a closed vessel to a temperature of 60 °C and vortex-mixed for at least 5 min to yield multilamellar vesicles (MLVs). MLVs were subjected to five to six freeze-thaw cycles. For the measurements, the samples were mounted in a sealed quartz cuvette (Hellma, Germany) with 1 mm path length. The temperature dependent studies were performed at four different selected temperatures and an equilibration time of half an hour was adopted at each new temperature.

Table 4.4: Values used for the preparation of samples for SANS measurements of DPPC/ergosterol systems at a concentration of 10 wt%

DPPC-d_{62}:ergosterol /mol%	82:18	80:20	78:22	76:24
DPPC-d_{62} /g	0.1	0.1	0.1	0.1
ergosterol /g	0.0109	0.0125	0.0140	0.01157
Mass of lipid (DPPC-d_{62}+ergosterol) /g	0.1109	0.1125	0.1140	0.1157
Scattering length density ρ /Å^{-2}	4.63×10^{-6}	4.57×10^{-6}	4.51×10^{-6}	4.45×10^{-6}
D_2O /Vol%	74.9	74.0	73.2	72.3
Volume of solvent (D_2O+H_2O) /mL	0.9285	0.9426	0.9559	0.9710
D_2O /mL	0.6956	0.6984	0.7002	0.7028
H_2O /mL	0.2329	0.2441	0.2557	0.2682

Neutron small-angle scattering (SANS) experiments were performed at the SANS II diffractometer at the Swiss spallation neutron source at the Paul Scherrer Institute. The wavelength of neutrons used for the measurements was 6.37 Å with $\Delta\lambda/\lambda = 0.1$ and the sample to detector distance was 5.0 m, corresponding to a scattering vector in the Q range from 0.005 to 0.05 Å^{-1}. The scattering cross-section density of the D_2O/H_2O solvent mixture is adjusted to that of the desired DPPC/ergo mixtures assuming the components are randomly distributed. Under these so-called matching conditions, the scattering is determined by large-scale concentration fluctuations in the plane of the lipid bilayer, only. The measured intensity distributions were corrected for absorption, sample thickness, inelasticity, and background.

4.8 Set-up for X-ray Reflectivity Measurements

The aim of the work was to study the supported multilamellar stack of membranes at full hydration and at different temperatures to get insight into the mesomorphic behavior of lipid membranes. The lipid membranes are only stable in water and exhibit an immense polymorphism at different temperatures. So, a closed sample chamber, which can control the temperature and relative humidity in the sample cell, is essential to study the detailed mesomorphic behavior of lipid membranes. The design of such a sample chamber fulfilling these conditions was conceived and efforts were undertaken to build it in-house. The sample chamber was constructed for studying fully hydrated and oriented samples by X-ray reflectivity. This sample chamber can successfully control the temperature and relative humidity.

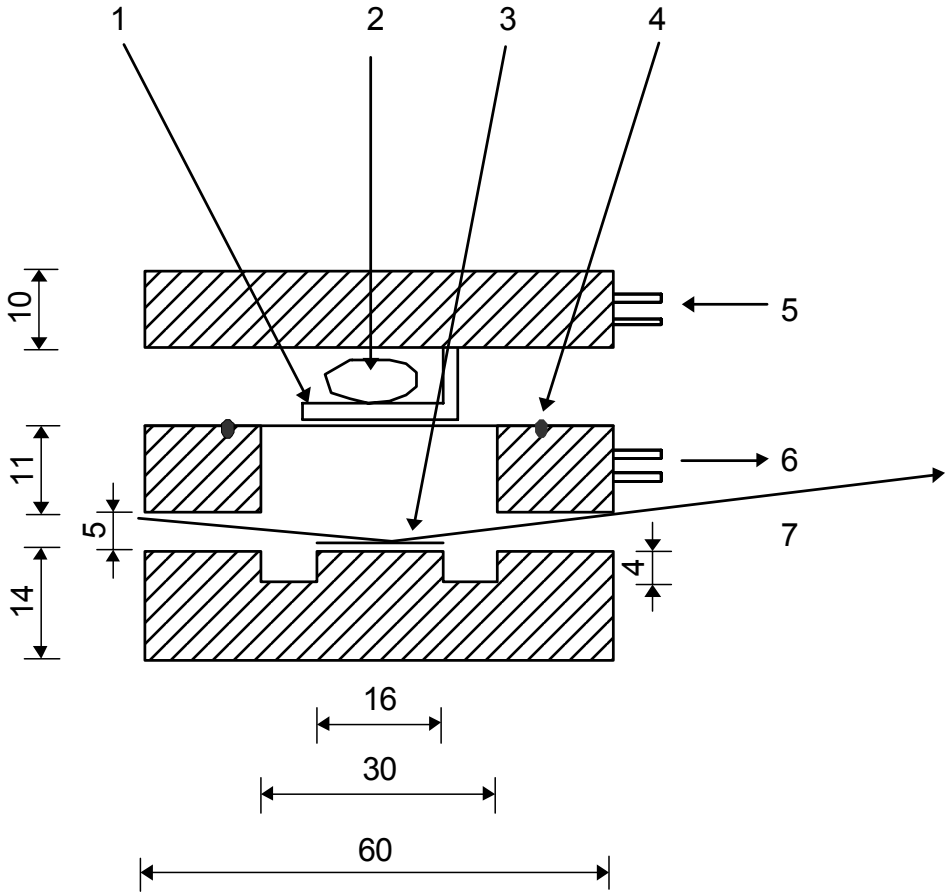

Figure 4.1(A): A schematic diagram of the inner sample chamber of the temperature and humidity controlled sample cell for X-ray reflectivity measurements (1 Support for sponge, 2 Sponge, 3 Sample, 4 O-ring, 5 & 6 Tubing to the thermostat, 7 Reflected X-rays). All the dimensions are on a mm scale.

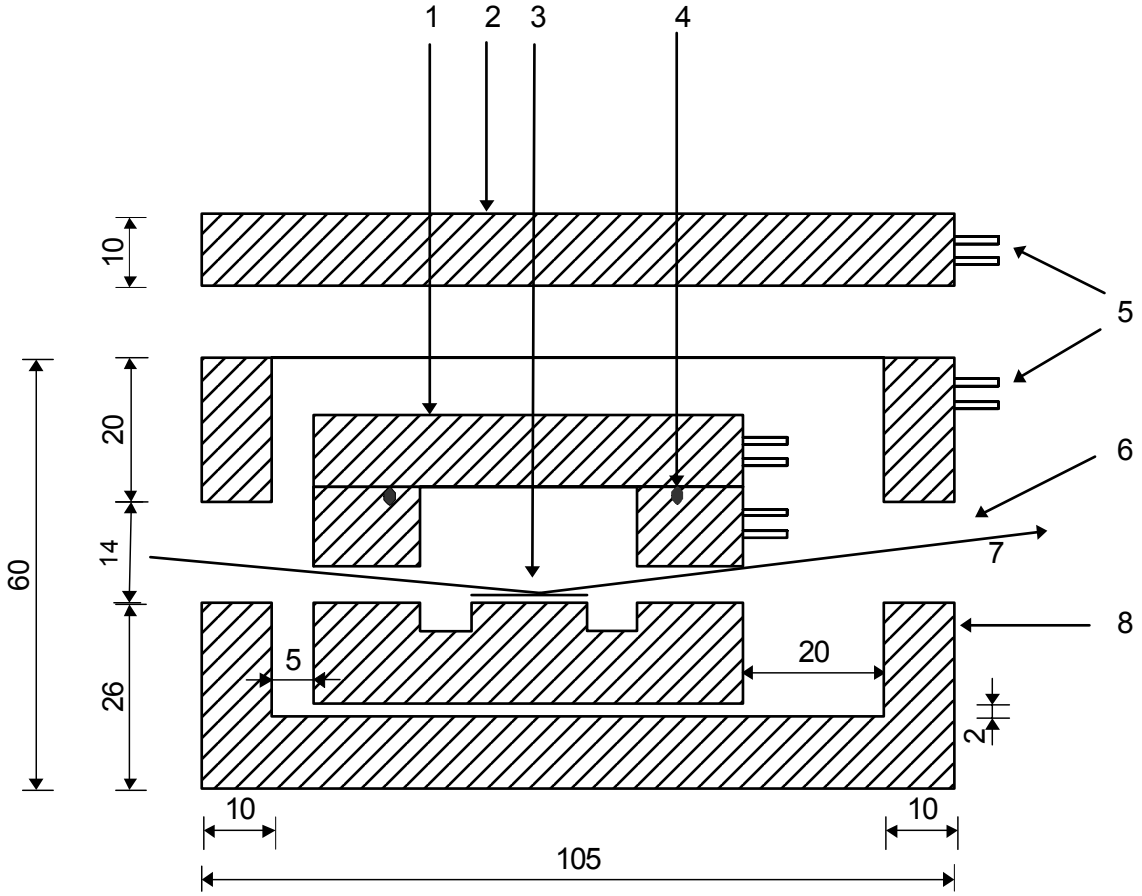

Figure 4.1(B): A schematic diagram of the temperature and humidity controlled sample cell (inner and outer chamber) for X-ray reflectivity measurements (1 Inner sample chamber, 2 Cover of the outer sample chamber, 3 Sample, 4 O-ring, 5 Tubing of the outer sample chamber to the thermostat, 6 Window, 7 Reflected X-rays, 8 Outer sample chamber). All the dimensions are on a mm scale.

The studied range of temperature is 10 °C-75 °C and humidity in the range from 11% to 100%. The temperature was controlled by a flow of water connected to the thermostat and the humidity was controlled by keeping various saturated salt solutions [O'Brien 1948] in the reservoir of the inner sample chamber. The details of different humidity levels adjusted by saturated salt solutions are given in Table 4.3 with an error of ± 2% [Lide 1995]. A schematic diagram of such a sample cell is depicted in Fig. 4.1A & B. With this sample chamber in hand, the solid supported lipid membranes can be studied to get the thermal induced phase transitions at full hydration and at partial hydration.

4.8.1 Sample Chamber

The sample chamber (Fig. 4.1A and B and Fig. 4.2) is double walled, consisting of an inner chamber and an outer chamber. The outer chamber is made of aluminium metal and the inner chamber is made of a high grade stainless steel (Material No. 1.4571) because this material is rust free and can withstand aggressive salt solutions and solutes. The sample was mounted on a sample support inside the inner chamber of the sample cell. The sample chamber has a pair of entrance windows and a pair of exit windows, covered with 6-µm thick mylar sheet (transparent) as indicated in Fig. 4.2. The mylar windows are used because the mylar material has very little scattering and it is often used as window material for the X-ray scattering experiments. So, these windows are completely fixed on both sides of the inner and outer sample chamber so that the leakage of water vapor is fully prevented. Pure water is placed in the reservoir of the inner sample chamber and a porous absorbent sponge saturated with water is placed in closed proximity (~3 mm) of the sample (Fig. 4.1 and Fig. 4.2), so that the samples get close contact to the excess water vapor and attain full hydration.

The temperature of the outer chamber and the inner chamber was individually controlled via two water thermostats (Lauda, Germany). To attain full hydration and to avoid temperature gradients, the sample chamber is tightly closed with the help of an O-ring (Material: 72 NBR 872) placed on top of the inner chamber. The temperature of the outer chamber is kept 3-4 °C higher as compared to the inner chamber to avoid the condensation of water vapor at the inner windows. So, the construction of the sample chamber leads to good temperature stability. To confirm the stability, the temperature of the sample cell was measured over time of 10 hr after adjustment to a new temperature and the error is less than 0.03 °C measured with the thermal element and to get this thermal equilibration state a long equilibration time of 1 hr is needed.

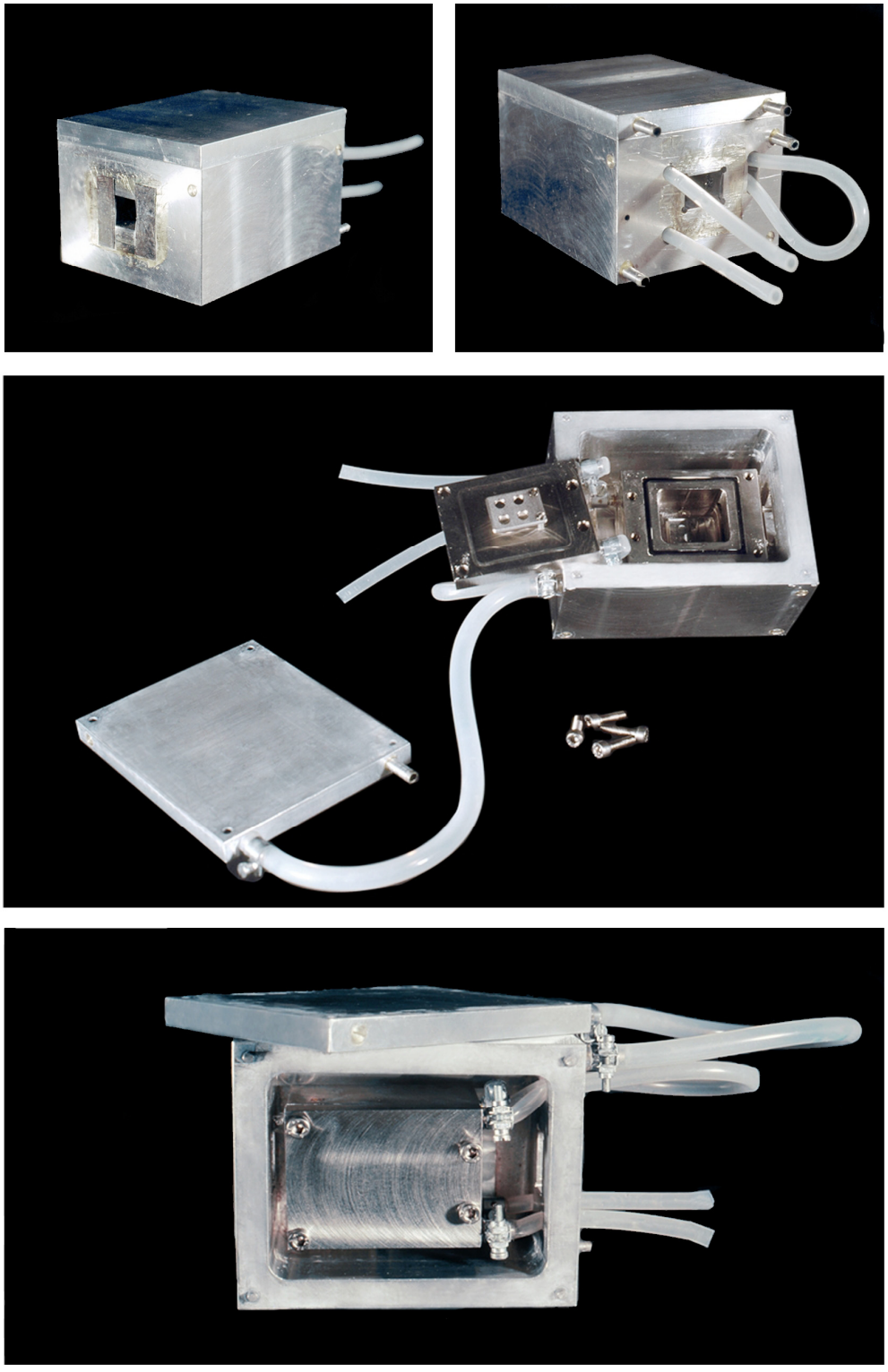

Figure 4.2: A photographed picture of the side and top view of the sample cell used for the X-ray reflectivity experiments

4.9 X-ray Reflectivity Measurements at the In-house Diffractometer

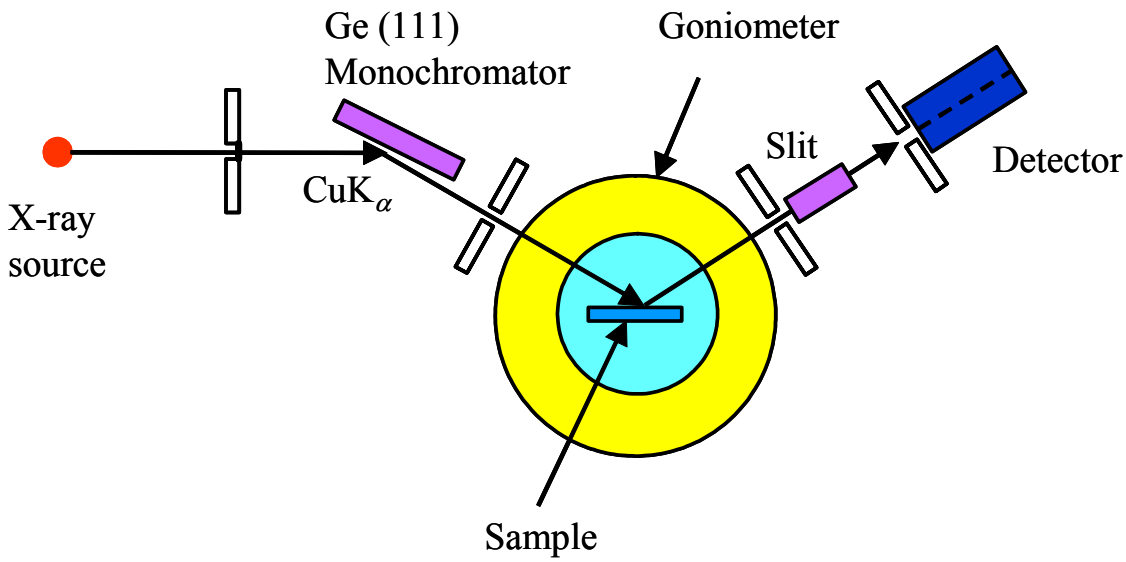

Figure 4.3: A schematic diagram of the X-ray reflectivity set-up of the in-house diffractometer XRD 3000 Theta/Theta from the company Rich. Seifert & Co.

X-ray reflectivity measurements were carried using our in-house diffractometer XRD 3000 Theta/Theta from the company Rich. Seifert & Co. The experimental arrangement is schematically shown in Fig. 4.3. To study the reflectivity of solid samples, the samples must remain horizontal and be as free from vibrations as possible. X-rays are produced in the sealed X-ray tube by the photons that are generated by energetic electron processes, gamma rays by transitions within atomic nuclei. The basic principle is that electrons are accelerated in order to collide with a metal target (Cu in this case). Here the electrons suddenly decelerate upon colliding with the metal target and if enough energy is contained within the electron, it is able to knock out an electron from the inner shell of the metal atom and as a result electrons from higher energy levels then fill up the vacancy and X-ray photons are emitted. This causes the spectral line part of the wavelength distribution. There is also a continuum Bremsstrahlung component given off by the electrons as they are shattered by the strong electric field near the high Z (proton number) nuclei. The X-rays thus generated first pass through two collimating slits (Fig. 4.3), which define the

dimensions and direction of the incident beam. The collimated X-rays then pass on to a double reflection channel-cut germanium monochromator. This monochromator is made by taking a single crystal of germanium and cutting a channel through which the X-rays can pass. The X-ray beam emerging from the channel-cut crystal is monochromatic, comprised of parallel rays of X-rays and displaced vertically or horizontally from the initial beam. The diffractometer has a double circle goniometer which controls the movement of the X-ray tube and detector which can be moved freely so that the incidence angle θ can be varied. The X-ray beam impinges on the sample in the sample cell which is mounted on *z*-axis of the diffractometer that moves the sample cell assembly vertically to compensate for the change in position of the incident beam. The X-rays reflected or scattered from the sample are collected and counted by the detector.

4.10 Measurements at Synchrotron HASYLAB/DESY in Hamburg

X-ray reflectivity measurements were also carried out at the W1.1 beamline of HASYLAB in DESY Hamburg. The X-rays produced at the synchrotron by the electrons that are emitted by an electron gun are first accelerated in a linear accelerator (linac) and then transmitted to a circular accelerator (booster synchrotron), where they are accelerated to reach high energy levels, e.g. billions of electron-volts. These high energy electrons are then injected into the DORIS III and PETRA II storage rings where they circulate in a vacuum environment at a constant energy, for many hours. These electrons in a storage ring are then forced to travel in a curved path by the bending magnets of the DORIS storage ring or by special magnetic structures known as wigglers and undulators. The radiation produced possesses many properties which simply can not be achieved using conventional radiation sources such as sealed X-ray tubes. The measurements are carried out at the beamline ROEW1. The main attribute of the ROEW1 beamline is its high versatility combined with a high photon flux.

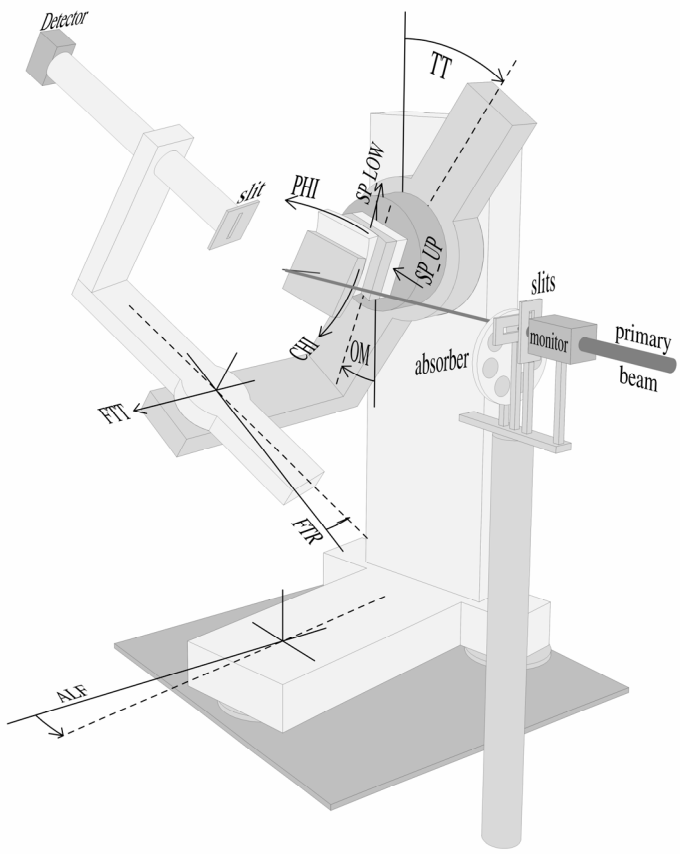

Figure 4.4: A Schematic diagram of the wiggler beamline W1.1 of the HASYLAB/DESY at Hamburg synchrotron.

The geometry of the reflectivity set-up used at the beamline is shown in Fig. 4.4. In front of the first monochromator crystal, located 24 m from the source point, the white beam is collimated by a computer controlled slit system. The monochromator box is evacuated (pressure $< 10^{-2}$ Pa). The first monochromator crystal reflects the beam downwards, the second upwards. Si (111) and Si (311) crystals (size 50×50 mm^2) symmetrically cut are available, covering an energy range from 4 to 20 KeV. The fine adjustment of the Bragg angle of the first crystal is performed by means of the MOSTAB feedback system with a piezo element. After the second crystal another remote controlled slit system is installed. The monochromatic beam may enter the experimental hutch directly or can be reflected upwards and focused by a gold-coated

toroidal mirror (7 mrad incidence angle). The resulting focus size in the experimental hutch is 2×4 mm^2 with a cutoff energy of 10.5 keV.

4.11 Measurements at the Spallation Neutron Source in Switzerland

The small angle neutron scattering measurements are carried out at the Swiss spallation neutron source SINQ at the Paul Scherrer institute in Switzerland. This source provides a neutron flux of about 10^{14} n/cm^2/s.

At this neutron source, the neutrons are produced by spallation reactions. First, protons are accelerated and injected into a target by a particle accelerator (protons at 500 MeV are traveling at 75% of the speed of light) and make multiple collisions with nucleons in a nucleus causing spallation (an intranuclear cascade). The high energy particles, such as neutrons and protons, emitted in the course of this process then collide with other nuclei, causing similar reactions (an extranuclear cascade). The residual nuclei of the cascade are in an exited state, and give off more neutrons (evaporated neutrons). In these processes, about ten fast neutrons are emitted for each proton. From the view point of energy output, the quantity of neutrons thus produced is about one hundred times that of a photonuclear reaction and about ten times that produced by fission in a nuclear reactor. The neutron source at the Paul Scherrer Institute consists of a target, moderators and reflectors (Fig. 4.5). The fast neutrons created in the target are slowed down by the moderator to an average speed of 2000 m/s to make them useful for materials and biological research. The reflectors are surrounding the target and the moderators, whose role is to focus the fast neutrons effectively on the moderator. A biological shield, made of steel and concrete, covers the neutron source assembly, which keeps the radiation exposure in the experimental area at a low level. The geometrical set-up, which is used at SANS-II at the Paul Scherrer Institute for the measurements of small angle neutron scattering on two-component DPPC/ergosterol systems is shown in Figure 4.6.

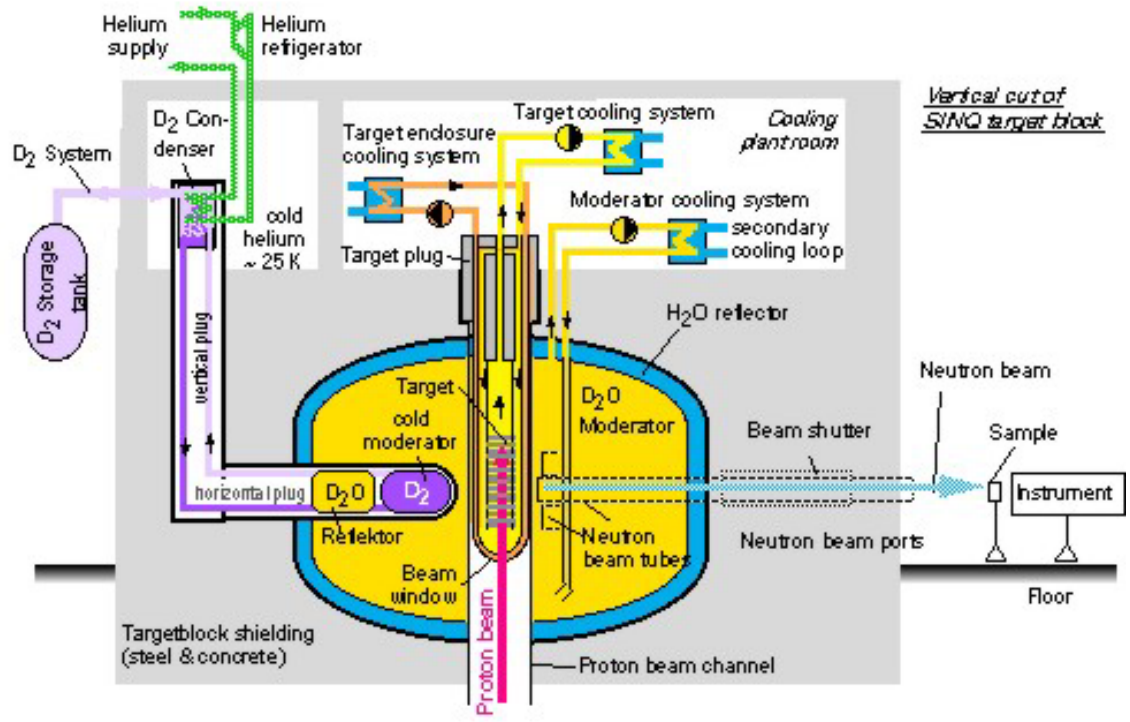

Figure 4.5: The diagram schematically shows the Spallation Neutron Source (SINQ) at the Paul Scherrer Institut (PSI), Villigen, Switzerland.

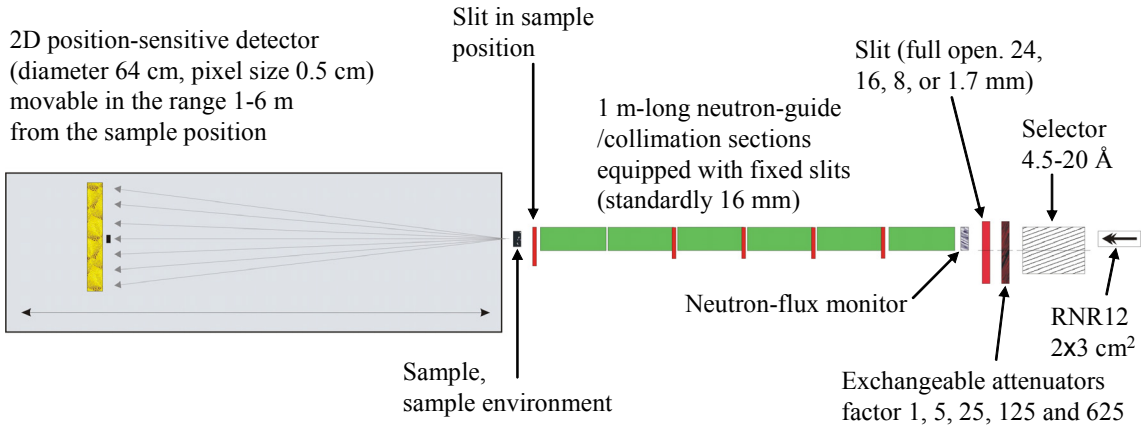

Figure 4.6: Schematic diagram of the SANS II instrument at the Spallation Neutron Source (SINQ) at the Paul Scherrer Institut (PSI), Villigen, Switzerland.

The incoming neutrons are monochromatized by a mechanical velocity sector. Collimation is performed in the six meter long collimation section. It consists of one fixed and five moveable one-meter sections in which nickel-coated neutron guides can be inserted individually by computer-controlled pneumatic cylinders, allowing the neutron source pin-hole to be moved from one to six meters in steps of one meter away from the sample position. The whole system, i.e. collimators, sample chamber and detector tank, can be operated in a single vacuum system without windows in order to lower the background. In that case, a 7-position sample exchanger (with temperature control in the range 6-80 ºC), or a 2-position furnace (up to 300 ºC) can be employed. The sample chamber can be, however, also fully removed and a turn-table can be installed instead. This option enables the use of bulky and heavy equipment such as a cryomagnet or shear devices. The area-sensitive multi-wire proportional neutron detector (Fig. 4.6 and Fig. 4.7) has been developed at Risø National Laboratory.

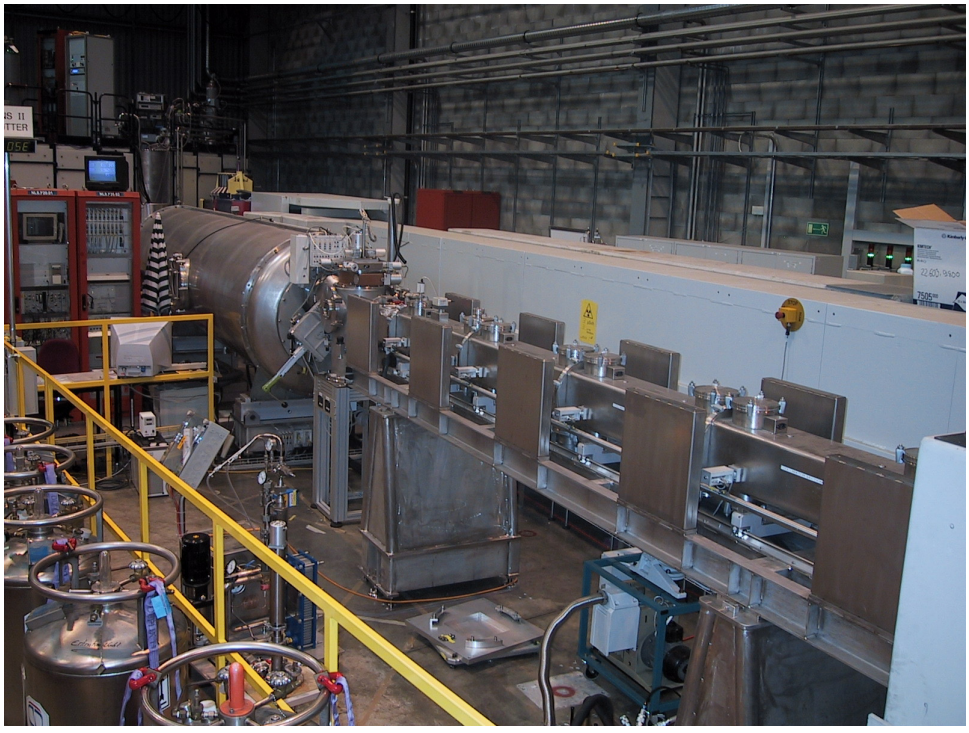

Figure 4.7: A SANS II instrument used for the small angle neutron scattering measurements at the Spallation Neutron Source (SINQ) at the Paul Scherrer Institut (PSI), Villigen, Switzerland.

The active volume is 64 cm in diameter and 4.5 cm thick and the total gas volume is 15.2 liters. The normal filling is 1 atmosphere ^{3}He plus 1.5 atmosphere argon and methane, which combines high efficiency and high spatial resolution. The gas is purified by convective circulation through an activated alumina filter, which is mounted in an enclosed space on the back of the detector together with the preamplifiers. The detector can be used in an evacuated space. The *xy*-positioning of the detected neutron is based on the difference in rise-times for pulses arriving at the two ends of the wire-grids. The anode grid is used for one coordinate and the two cathode grids, coupled in parallel after the preamplifiers, are used for the other coordinate.

The detector can be moved continuously from one to six meters away from the sample position. The *Q*-range used for the measurements was 0.005-0.05 Å^{-1}.

5 Results and Discussion

The phase behavior of lipid systems is intimately linked with the parameters like temperature and the extent of hydration. A change in one of these separately or simultaneously can have a profound effect on their structural organization. Understanding of the structural changes are possible through temperature and/or hydration dependent studies with appropriate biophysical techniques and correlating these data with rationally designed models that are built upon our existing knowledge of lipid membrane systems.

In this chapter, the phase behavior of different lipid systems as a function of temperature and hydration is discussed. Different types of data sets were measured by X-ray reflectivity (XRR), differential scanning calorimetry and pressure perturbation calorimetry (DSC/PPC), Fourier-transform infrared spectroscopy (FT-IR) and small-angle neutron scattering (SANS) techniques. Parts of these measurements were carried out at the W1.1 beamline of HASYLAB/DESY in Hamburg and at the SANS-II instrument at the Paul Scherrer Institute, Switzerland, and others at the Physical Chemistry I department. The following discussion is divided into sections depending upon the nature of the physical method used or the type of membrane system investigated.

5.1 One Component System DPPC

X-ray reflectivity measurements were carried out on DPPC lipid membranes to gather information on the phase behavior, lamellar repeat distance *d*, and structural organization as a function of temperature and relative humidity. These experiments were carried out using an in-house X-ray diffractometer equipped with CuK_{α} radiation and a highly oriented monochromator. The set-up of the experiments is explained in detail in section 4.9. The measurements on the lipid DPPC were carried out with a newly constructed humidity and temperature controlled sample cell (details of the design and construction have been described in section 4.8). In a reflectivity experiment, the specular reflection is determined as a function of momentum transfer

vector Q, perpendicular to the surface: $Q = (4\pi / \lambda)\sin\theta$ (λ=1.54 Å, wavelength of the radiation used, 2θ is the scattering angle). When there are no lipid bilayers deposited on the substrate, the typical reflectivity curve of a clean hydrophilic silicon substrate is as shown in Fig. 5.1. As expected, there is a smooth decrease of reflectivity with increase in scattering angle without showing any Bragg peaks. However, once the lipid bilayers are deposited onto this substrate, the reflectivity pattern changes depending upon the nature and structure of the deposited bilayers. Such a variation is recorded in Fig. 5.2. The reflectivity curves shown were recorded from three different DPPC samples at nearly full hydration and at room temperature (25 °C). In these reflectivity curves (Fig. 5.2), one can clearly observe the Bragg peaks when DPPC lipid bilayers were deposited onto the substrate. From the intensity oscillations between the Bragg peaks (Kiessig fringes), one can determine the total thickness of the lipid layer on the substrate. The observation of the Kiessig fringes indicates a well-defined film thickness and thus a well defined number of bilayers [Mennicke 2002]. The uppermost black curve in Fig. 5.2 clearly represents the highest film thickness and the calculations reveal the presence of more than 100 bilayers.

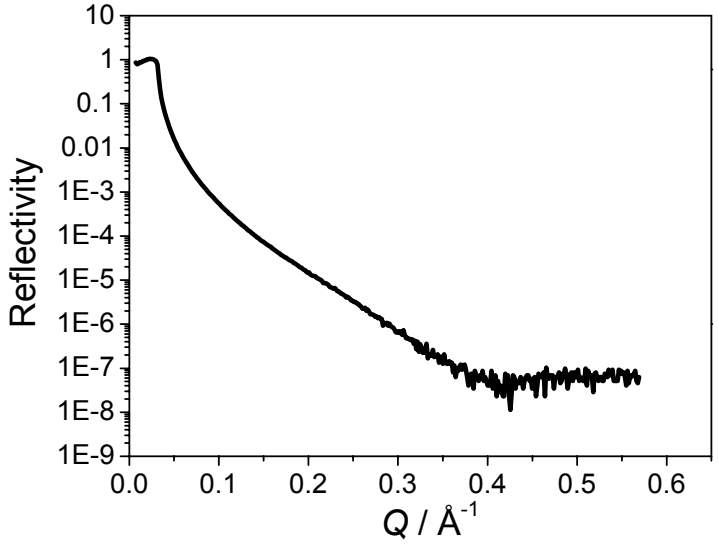

Figure 5.1: A reflectivity curve of bare silicon substrate hydrated by water vapor, measured at the Seifert diffractometer XRD 3000 TT.

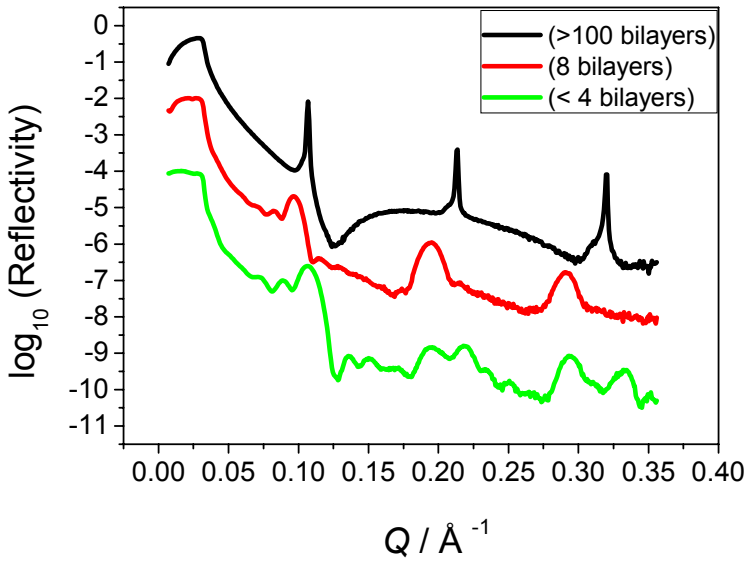

Figure 5.2: X-ray reflectivity measurements of three DPPC samples prepared from lipid solutions of a concentration of 5 mg/mL by spreading an organic solution (black curve). The red and green curves were measured from concentration of 10 mg/mL and 5 mg/mL by spin-coating at 300 rpm and 3000 rpm. All curves were measured at ≈ 100% RH and at 25 °C. The curves are shifted vertically for clarity.

As the thickness of the deposited bilayers decreases, the intensity of the Bragg peaks decreases and the peaks broaden (red and green curve of Figure 5.2). The red reflectivity curve was obtained from a stock solution of 10 mg/mL DPPC in trifluoroethanol (TFE) spin coated at 300 rpm and shows 8 bilayers. The green curve was measured from a DPPC stock solution of 5 mg/mL at 3000 rpm and is based on < 4 bilayers on the substrate. The rough estimation of the number of deposited bilayers is calculated from the simulations using the Parratt program [Parratt 1954].

Development of an adequate experimental procedure to control the thickness of the stacked bilayers is very important. The achievement of a desired thickness and the procedure to vary them (in a controlled way), endows one to understand their phase behavior at different experimental conditions. In this context, the curves in Fig. 5.2 clearly show the variation in thickness of the stack of bilayers indicated by the changes in the shape and intensity of the Bragg peaks. This amply demonstrates that by the spin-coating method, one can to a large extent control and vary the number of

stacked bilayers. The number of bilayers can be controlled by varying the concentration of the lipid solution and the rotational frequency of the spinning substrate (Fig. 5.2).

The position of the Bragg peaks is related to periodic distances within the lyotropic lipid mesophase. From the position of the Bragg peaks, the lamellar repeat distance *d* can be calculated by using the formula $d = n2\pi / Q$, (where *n*= 1, 2, … is the order of reflection, and *d* is the sum of the water and lipid layer thicknesses). For DPPC bilayers at 100% RH, a lamellar repeat distance of ~64 Å was obtained at a temperature of ~27 °C (which is in well agreement with the literature data [Quinn 1989]) as shown in Figure 5.3.

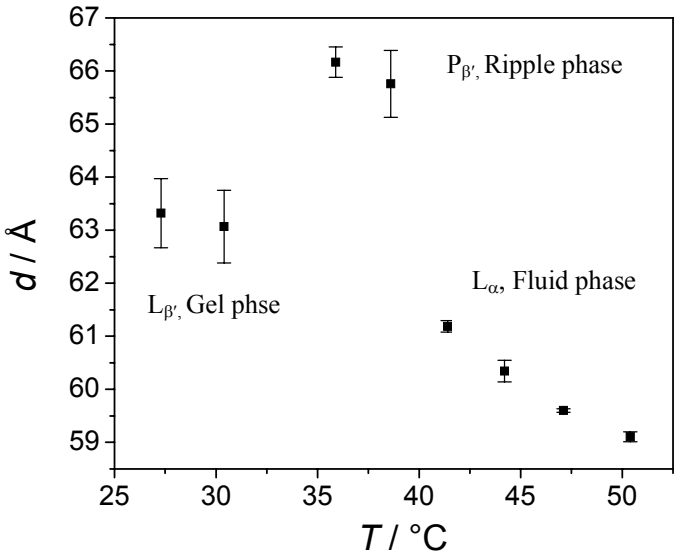

Figure 5.3: Structural transitions of dipalmitoylphosphatidylcholine (DPPC) showing the relationship between temperature and lamellar repeat distance at a relative humidity of 100%.

The DPPC bilayers exhibit different lyotropic phases as a function of temperature (Fig. 5.3). Clearly, the pretransition as well as the main lipid phase transition were observed at about 36 °C and 42 °C, respectively. The lamellar repeat distance increases from ~64 Å in the $L_{\beta'}$ phase to ~67 Å in the $P_{\beta'}$ ripple gel phase, and further decreases to a lamellar repeat distance of ~59 Å due to the highly disordered chains in

the fluid L_α phase. To yield further structural information on the DPPC bilayer, the fit of the reflectivity curves at different relative humidities and at a temperature of ~25 °C (details are given in section 4.3.3) was performed by using the Parratt program [Parratt 1954], which is shown in Figure 5.4. Parratt is a computer software to calculate the reflectivity of neutrons or X-rays from flat surfaces. From the calculated reflectivity, an electron density profile of the system can be determined. To fit the data, first the model for the layer system has to be setup. Some standard set of parameters (e. g., thickness and electron density of water, silicon substrate etc.) are already present in the program which are loaded automatically on start-up. For every layer in the model, at least two values have to be entered. The two essential values are: the layer thickness in Angstrom (d /Å) and the real part of the electron density (ρ /Å^{-2}). The four other parameters are the imaginary part of the electron density (Im (ρ /Å^{-2})), the roughness of the layer (σ /Å), and the magnetic contribution to the electron density (R (mag), I (mag), in Å^{-2}).

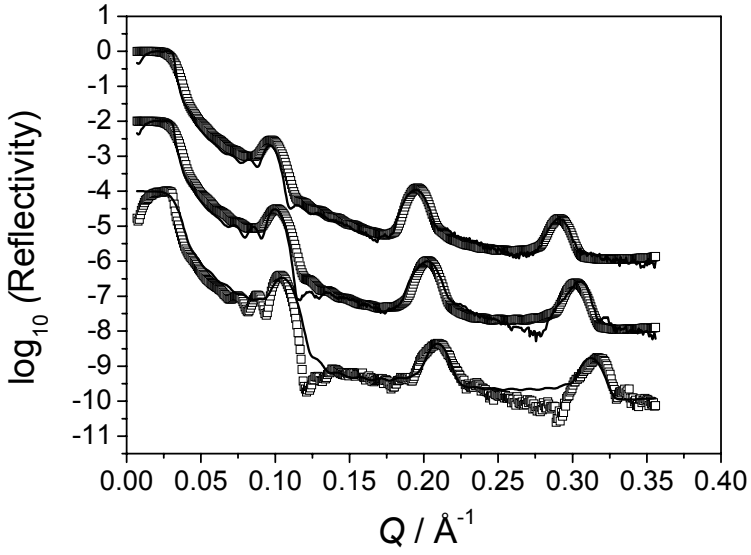

Figure 5.4: X-ray reflectivity measurements of spin coated DPPC samples containing 8 bilayers prepared from a solution of 10 mg/ml rotating at 300 rpm (top to bottom, hollow symbols) along with simulations (solid lines) by the Parratt program. The top curve, middle curve and lower curve were measured at ~100%, 90% and 70% RH from water vapors and at room temperature (T ~25 °C). All the curves are shifted vertically for clarity.

A reasonable value of the thickness and electron density (from literature [Petrache 1998]) of each layer was entered and the fit of the reflectivity curves and electron density profiles for DPPC bilayers were determined.

A good fit of the data was obtained only when the thickness of each component of the bilayer, electron density and roughness, were allowed to vary across the sample (Fig. 5.4, solid line). In this Figure, one can clearly observe that the Bragg peaks have shifted to larger Q values at lower humidity, which indicates a smaller repeat distance (d = 62.3 Å at 90% and d = 60.1 Å at 70% RH) and less hydration of the sample. This further demonstrates that, as the relative humidity in the sample decreases, the thickness of the stack of the bilayer also decreases, leading to a smaller water layer thickness (d_W). This can also be deduced from the fit of the reflectivity curve giving a water layer thickness of 6.8 Å and 4.9 Å at ~90% and ~70% RH respectively (Table 5.1A). From the fit, an electron density profile and other structural parameters were also obtained as shown in Figure 5.5A and are recorded in Table 5.1A.

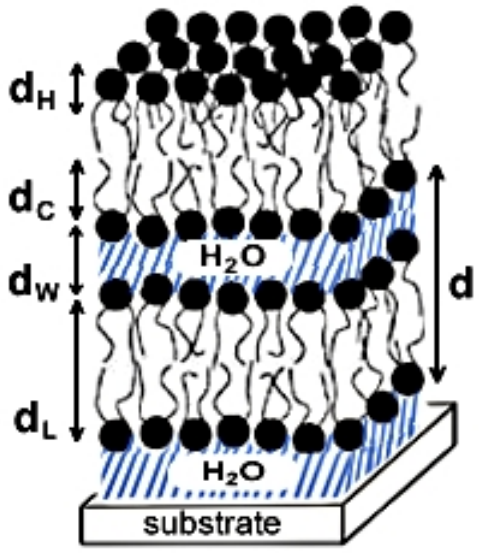

Figure 5.5A: Schematic diagram of the supported bilayer on silicon substrate. The size of the membrane is exaggerated to illustrate its structure; actual membranes are typically 50 Å thick and are separated from the surface by a ~10 Å layer of water. The parameters d_H (headgroup thickness), d_C (chain thickness), d_W (water layer thickness), d_L (lipid bilayer thickness), and d (lipid bilayer thickness and water layer thickness). In the text, these parameters are given in italics.

Table 5.1A: Structural results for the DPPC bilayer at 25 °C

Fit Parameter (DPPC)	At RH 100%	At RH ~90%	At RH ~70%
d /Å	64.7	62,3	60,1
d_H /Å	9.66	9.58	9.53
d_C /Å	16.2	16.25	16.20
d_W /Å	9.0	6.8	4.95
d_G /Å	4.0	3.87	3.77
d'_W /Å	24.0	24.0	24.0
ρ_H /Å^{-2}	1.16E-05*	1.24E-05	1.28E-05
ρ_C /Å^{-2}	0.89E-05*	0.92E-05	0.93E-05
ρ_G /Å^{-2}	0.48E-05*	0.48E-05	0.51E-05
ρ_W /Å^{-2}	0.95E-05*	0.91E-05	0.90E-05
ρ_{sub} /Å^{-2}	2.01E-05	2.01E-05	2.01E-05
σ_{sub} /Å	5.1	5.1	5.1
σ'_W /Å	7.13	7.13	7.13
σ_H /Å	2.0	2.0	2.0
σ_C /Å	2.0	2.0	2.0

The parameters: d (lipid bilayer thickness and water layer thickness), d_H (headgroup thickness), d_C (chain thickness), d_W (water layer thickness), d_G (thickness of the gap of the bilayer), d'_W (water layer thickness separating the lipid bilayer and substrate), ρ_H (electron density of headgroup), ρ_C (electron density of chain), ρ_G (electron density of the gap), ρ_W (electron density of water layer), ρ_{sub} (electron density of silicon substrate), σ_{sub} (roughness of the silicon substrate), σ'_W (roughness of the water layer separating the lipid bilayer and substrate), σ_H (roughness of the headgroup), σ_C (roughness of the chain)

Table 5.1B: Literature values [Petrache 1998] of electron density for comparison with measured * values in Table 5.1A

Electron density of DPPC bilayer	At RH 100%
ρ_H /Å^{-2}	1.29E-05
ρ_C /Å^{-2}	0.90E-05
ρ_G /Å^{-2}	0.56E-05
ρ_W /Å^{-2}	0.78E-05

The electron density profiles obtained by fitting the DPPC reflectivity data at different relative humidity levels and at ~25 °C are shown in Figure 5.5B.

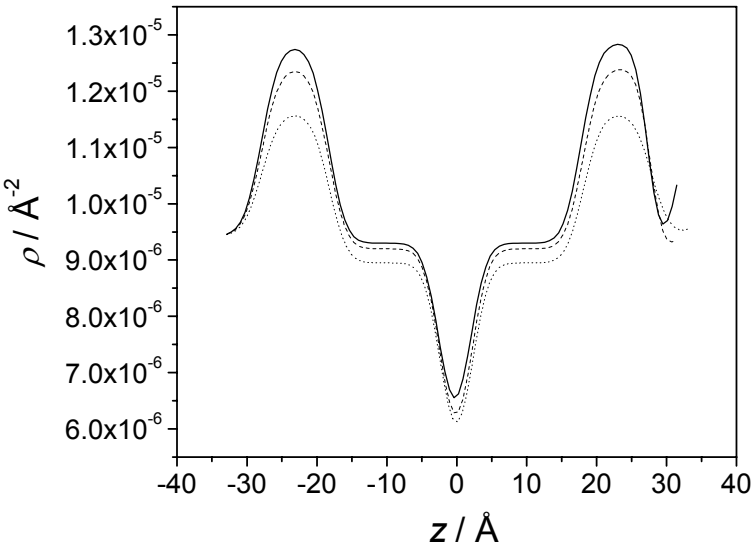

Figure 5.5B: Electron density profiles of DPPC at ~70% RH (solid), at ~90% RH (dashed), and at 100% RH (dotted) and at 25 °C in units of electrons/Å^{-2} as a function of z along the bilayer normal with the center of the bilayer at $z = 0$, obtained from the Parratt program.

The total repeat distance of the DPPC bilayer system is deduced from the Bragg peak positions and is found to be 64.7 Å at 100% RH with a headgroup thickness (d_H) of 9.66 Å, chain thickness (d_c) of 16.2 Å and intervening water layer thickness of 9 Å (Table 5.1). The roughness of the layers obtained is about 2 Å. The number of bilayers obtained was found to be eight from the width of the Bragg peaks and simulation of the curves by the Parratt program.

In these studies, a thin and thick stack of DPPC bilayers was obtained by using spin-coating and spreading by the organic solution method. It has been demonstrated that the variation in the thickness of the stack can be controlled by the deposition parameters and rotational frequency of the spin coater.

5.2 Archaebacterial Lipid PLFE

The thermoacidophilic archaebacterium *Sulfolobus acidocaldarius* lives at high temperatures (normally 65–80°C) and in acidic environments (pH 2–3) (Fig. 5.6), while its intracellular compartment is nearly neutral. The ability of the organism to sustain such harsh growth conditions has definite relation with the specific properties of its plasma membrane lipids.

Figure 5.6: Hyperthermophilic bacteria at terrestrial geysers/hot springs (max. 100 °C)

The major components of the plasma membrane of *S. acidocaldarius* are bipolar tetraether lipids (~90% of the total lipids) [de Rosa 1986]. Among them, the polar lipid fraction E (PLFE) is the main constituent [Lo 1990]. Approximately 90% of PLFE lipids are a glycerol dialkylnonitol tetraether (GDNT) containing phosphatidylmyoinositol on one end and β-glucose on the other (Fig. 5.7). About 10% are glycerol dialkylglycerol tetraether (GDGT) with phosphatidylmyoinositol attached to one glycerol and β-D-galactosyl-D-glucose attached to the other (Fig. 5.7). Both GDGT and GDNT consist of a pair of 40-carbon phytanyl hydrocarbon chains. Each

of the biphytanyl chains contains up to four cyclopentane rings, and the number of these rings increases with increasing growth temperature [de Rosa 1988].

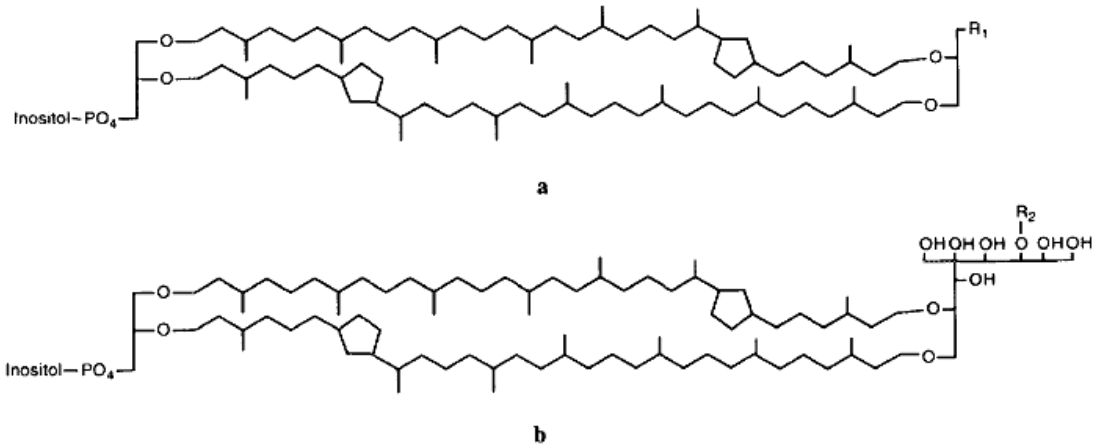

Figure 5.7: The structures of PLFE consists of (a) a symmetric glycerol dialkyl glycerol tetraether (GDGT) skeleton with phosphatidylinositol on one end and R_1=β-D-glucopyranose and (b) a glycerol dialkyl nonitol tetrether (GDNT) skeleton with phosphatidylinositol on one end and R_2=β-D-galactopyranosyl-β-D-glucopyranose (adapted from [Chang 1994]).

In aqueous solution, PLFE lipids extracted from *S. acidocaldarius* form stable multilamellar liposomes with vortexing, and unilamellar vesicles (diameters, 60-800 nm) with extrusion [Lo 1990, Elferink 1992, Komatsu 1998]. These liposomes exhibit no or only broad and small-magnitude endothermic phase transitions in the temperature range of 10–70 °C. Electron microscopy showed that in PLFE liposomes, the lipids span the entire lamellar structure, forming a monomolecular membrane [Elferink 1992]. PLFE liposomes exhibit high thermal stability, which has been attributed to the rigid and tight membrane packing in PLFE liposomes [Komatsu 1998]. The tightness of membrane packing increases with increasing number of cyclopentane rings in the phytanoyl chain of PLFE lipids [Gabriel 2000].

PLFE liposomes have been used as a model for thermoacidophilic archaeal membranes. In addition, due to their remarkably high stability against high temperature, acidic/alkaline pH, oxidation, and the actions of phospholipases, bile salts, and serum proteins, PLFE and other bipolar tetraether liposomes have been used

in technological development, such as sterilization, immunoassays and vaccine or drug delivery [Chong 2003]. In our studies, X-ray reflectivity, differential scanning and pressure perturbation calorimetry (DSC/PPC) along with Fourier-transform infrared spectroscopy (FT-IR) techniques were used to further characterize membrane packing and phase behavior of PLFE lipid.

X-ray reflectivity gave us information on the lamellar repeat distance, *d*, as a function of temperature and hydration and the phase behavior of nonlamellar structures of the archaebacterial membranes at full hydration. PPC allowed for the determination of the thermal volume expansion coefficient, α, as a function of temperature. From the plot of α versus *T*, the phase transitions (that involve significant volume changes) can be detected and the relative volume changes ($\Delta V/V$) associated with these phase transitions can be calculated. In addition to PPC, differential scanning calorimetry (DSC) was employed to detect the phase transitions involving significant enthalpy changes (ΔH) [Chong 2005]. FT-IR spectroscopy was used to yield further information about the conformational and molecular order of the acyl chains as well as structural changes of archaebacterial lipid (PLFE).

5.2.1 X-Ray Reflectivity Measurements

X-ray reflectivity studies were carried out on PLFE lipid to report the lamellar repeat distance, *d*, and the diffraction patterns of non-lamellar structures at different temperatures and at different relative humidity. The X-ray reflectivity experiments were performed at the wiggler beamline W1.1 at HASYLAB/DESY in Hamburg. The experimental setup has already been described in detail in section 4.10. The reciprocal spacings of the reflections of indices *hkl*, is defined by: $s_{hkl} = (2/\lambda)\sin\theta$, where λ =1.18 Å is the wavelength of radiation and 2θ is the scattering angle. The momentum transfer vector Q can also be defined as $Q = 2\pi s$, and the range of scattering vector covered is 0.01-0.55 $Å^{-1}$. The positions of Bragg peaks are related to periodic distances within lyotropic lipid mesophases, their sharpness or width reflects the extent of this periodicity over large distances.

In the case of cubic lipid phases, Bragg peaks may be observed at

$$Q = \frac{2\pi}{a}\sqrt{h^2 + k^2 + l^2}$$

where *a* is the cubic lattice constant. The Miller indices *h*, *k*, *l* depend on the lattice type (primitive, body-centered, face-centered) and the symmetry elements of the cubic structure. In Table 5.2, the relative Bragg peak positions of the three most common bicontinuous cubic lipid-water phases are shown. The bicontinuous cubic phases of type II (Q_{II}) can be visualized in terms of a highly convoluted lipid layer, which subdivides three dimensional space into two disjointed polar labyrinths separated by an apolar septum.

Table 5.2: Inverse cubic lipid-water mesophases and expected Bragg peak position ratios at low angles[a]

Lipid-water phase	Space group	Peak position ratio
Q_{II}^{D}	Pn3m	$\sqrt{2}:\sqrt{3}:\sqrt{4}:$ …
Q_{II}^{P}	Im3m	$\sqrt{2}:\sqrt{4}:\sqrt{6}:$ …
Q_{II}^{G}	Ia3d	$\sqrt{6}:\sqrt{8}:\sqrt{14}:$ …

[a] The cubic phases are based on lipid layers curved in three dimensions. The midplanes of the layers are D, P, or G infinite periodic minimal surfaces, as denoted with the superscripts in the phase symbols.

The structures of three of these phases, Q^{230}, Q^{224}, and Q^{229}, are closely related to the Schoen Gyroid (G), the Schwarz (D), and the Schwarz (P) infinite periodic minimal surfaces (IPMS), respectively. IPMS is an intersection free surface periodic in three dimensions with a mean curvature that is everywhere zero.

Figure 5.8 shows the X-ray reflectivity curves of PLFE lipid (cells grown at 65 °C) membranes spin-coated from 10 mg/mL solution in chloroform/methanol/water (45:45:10 v/v/v, pH ~7.5 without adjustment with acid/alkali) at 97% RH adjusted with water vapor from saturated salt solution of K_2SO_4 [Lide 1995]. The temperature range covered was from room temperature, ~27 °C, to 70 °C. As can be clearly seen,

four to five orders of lamellar Bragg reflections are visible over this temperature range.

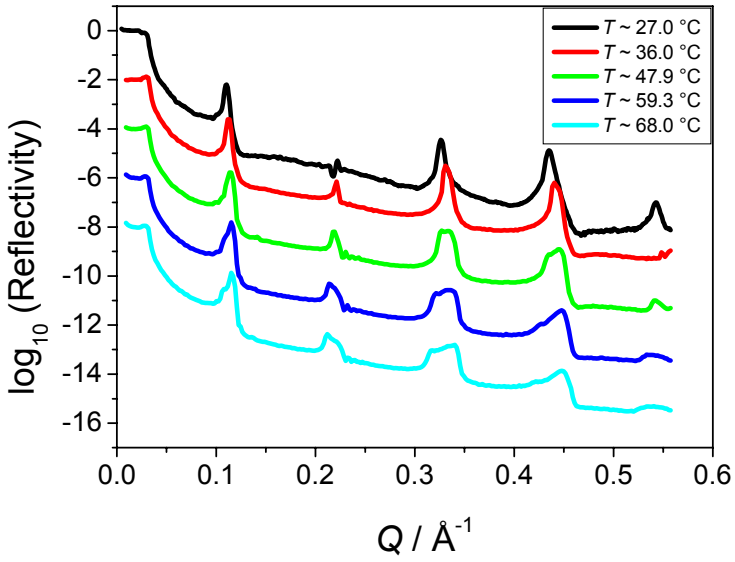

Figure 5.8: X-ray reflectivity measurements of PLFE (cells grown at 65 °C) samples prepared from lipid solutions at a concentration of 10 mg/mL by spin coating. All the curves are measured at different temperatures at 97% RH (pH ~7.5)

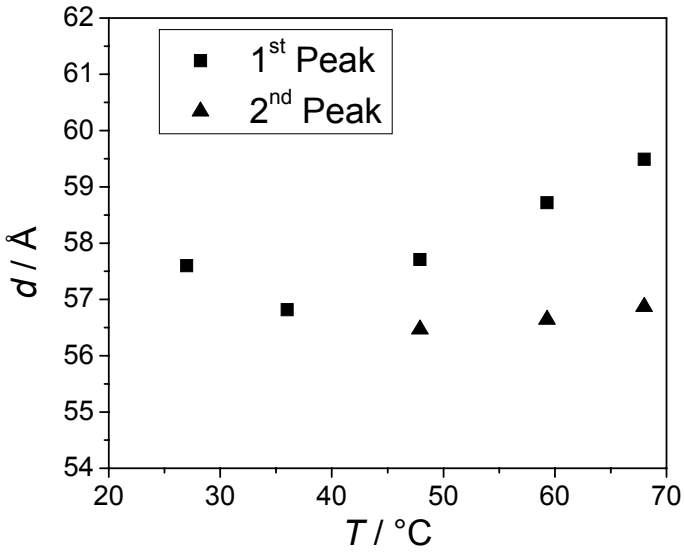

Figure 5.9: Structural transitions of PLFE, (cells grown at 65 °C) showing the temperature dependence of the lamellar repeat unit at a relative humidity of ~97%.

The lamellar repeat distances *d* calculated from the Bragg peaks are shown in Figure 5.9. The lamellar repeat distance, *d*, at a temperature of ~47.9 °C is calculated from the third and fourth order Bragg peaks. The lamellar repeat distance at *T* ~59.3 and 68 °C is calculated from second, third and fourth order Bragg peaks where the two peak structure is more pronounced. The structures observed between 27 °C and 70 °C may be attributed to a lamellar phase region. As shown in Figure 5.9, a lamellar to lamellar phase separated transition with minor structural changes seem to take place at ~38 °C observed with two different bilayer thicknesses. This small change in lamellar repeat distance as a function of temperature in the range 27 °C-70 °C can, for example, be due to changes in the tilt angle of the lipid molecules with respect to the lipid layer normal, due to the degree of hydration at the polar headgroups, or due to the lateral and transverse rearrangement of lipid components, or most likely, due to minor changes in lipid conformation with increasing temperature, due to an increase in the population of gauche conformers. There are no major phase transformations at 97% RH. As the lipid system consists of a complex mixture of GDGT and GDNT lipid molecules, no pure one-phase regions and hence no sharp transformations between phases might be expected. Instead, more or less broad phase coexistence regions may be envisaged.

Figure 5.10A displays the two temperature scans at 27 °C and at 49.8 °C at full hydration and Figure 5.10B shows the blow up of the normalized curve (at 49.8 °C) of Figure 5.10A in the Q-range of 0.01-0.25 $Å^{-1}$. The lamellar repeat distance, *d*, at a temperature of ~27 °C is not determined due to the absence of the pronounced and sharp Bragg reflections. A major phase transformation at 49.8 °C in the reflectivity profile is observed. This indicates the transition from a lamellar to a nonlamellar structure. The reflectivity data at 49.8 °C are in agreement with a phase coexistence region between a diminishing lamellar and developing nonlamellar phases of cubic symmetry.

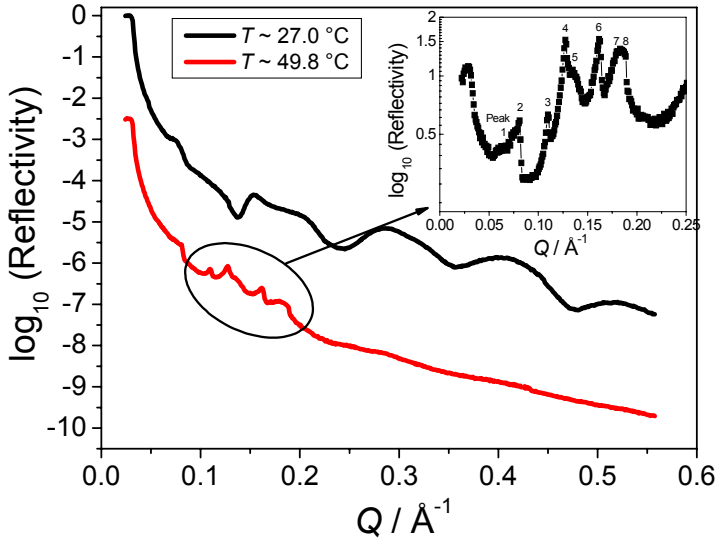

Figure 5.10A: X-ray reflectivity measurements of PLFE (cells grown at 65 °C) samples prepared from lipid solution at a concentration of 10 mg/mL by spin coating. The red curve is measured at a temperature of ~49.8 °C. Both curves are measured at ~100% RH. (pH ~7.5) and shifted vertically for clarity.

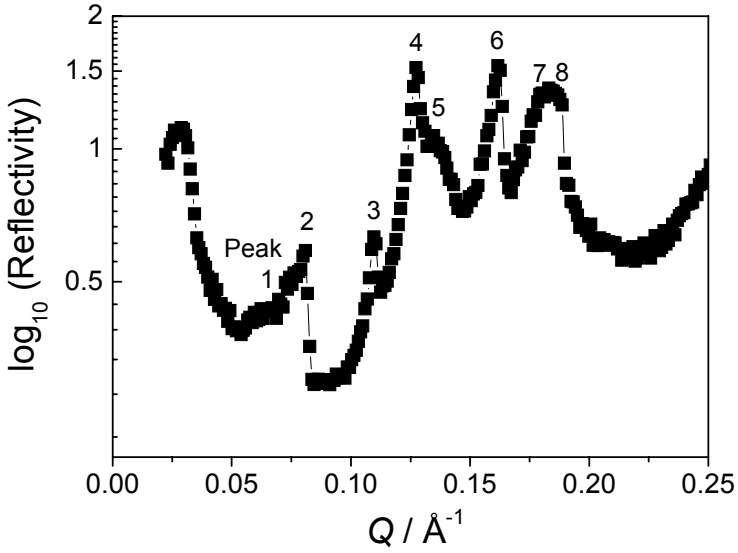

Figure 5.10B: Blow up of the normalized red curve of Figure 5.10A in the Q-range of 0.01-0.25 Å^{-1}.

The reciprocal spacing of the new, cubic phases can tentatively be assigned to two coexisting bicontinuous cubic phases, which can be indexed assuming a coexistence of the inverse bicontinuous cubic structures Q_{II}^{D} and Q_{II}^{P} with lattice constants of 117 and 151 Å, respectively. Interestingly, the ratio of the lattice constants of the cubic structures Q_{II}^{D} and Q_{II}^{P}, $a(Q_{II}^{D})/\ a(Q_{II}^{P})$ is 1.28, which is indeed what is expected theoretically (1.279) for these two bicontinuous cubic structures being in equilibrium with each other in excess water, and thus supports the tentative peak assignment.

Cubic phases Q_{II}^{D} and Q_{II}^{G} (rather than Q_{II}^{P}) have previously been detected in the total polar lipid extract (PLE) from the plasma membrane of *Sulfolobus solfatarius*, a thermoacidophilic archaeon with lipid compositions resembling those in *S. acidocaldarius* [Gulik 1985]. In addition, Q_{II}^{G} was detected in the PL fraction [Gulik 1988] and in the hydrolyzed GDNT lipids of the PLE from *S. solfataricus*. However, in the studies of Gulik et al. [Gulik 1985, Gulik 1988] no cubic phase was reported for the P2 lipid fraction from *S. solfataricus*, which is similar to the PLFE lipid fraction from *S. acidocaldarius* with regard to lipid composition. This discrepancy may be attributed to the differences in experimental conditions (e.g., pH and water content) or subtle differences in lipid composition. It is already reported that at a given growth temperature, the number of cyclopentane rings in tetraether lipids has a broad range, rather than a fixed value. The average number and the distribution of the ring may vary with growth conditions in a species-dependent manner.

The lamellar repeat distance of PLFE was also calculated by varying the relative humidity in the sample cell. The relative humidity was controlled by keeping various saturated salt solutions inside the reservoir of the sample cell (details in section 4.3.3). The plot of lamellar repeat distance *d* with respect to relative humidity (RH) is shown in Figure 5.11. The change in lamellar repeat distance is observed as we increase or decrease the relative humidity by saturated salt solutions. As the relative humidity in the sample increases, the thickness of the film increases corresponding to an increase in the thickness of the intervening water layer.

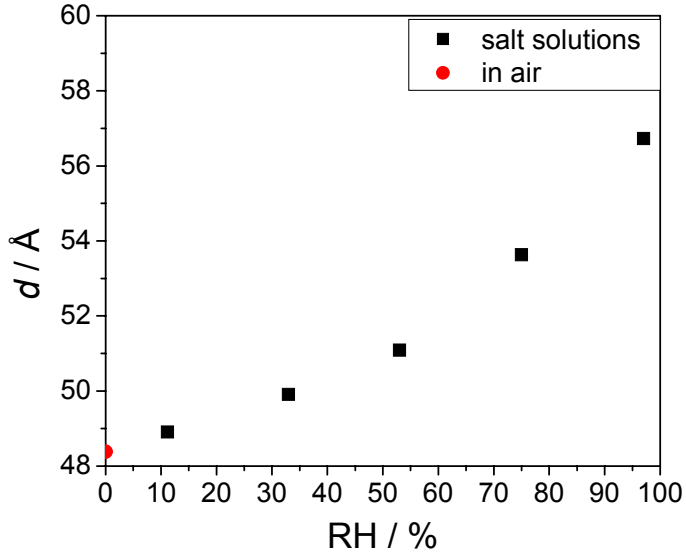

Figure 5.11: The hydration dependence of the lamellar repeat unit of PLFE (cells grown at 65 °C) as obtained by using saturated salt solutions at a temperature of ~25 °C.

The lamellar repeat distance (*d*) of PLFE lipid (growth temperature 65 °C) was 57±0.5 Å at 97% RH, and decreases to 49 ± 0.5 Å at ~11% RH measured at a temperature of 25 °C.

In the present study, at 97% RH, a lamellar to lamellar phase separated transition at a temperature of ~38 °C with minor structural changes seems to occur and the lamellar to cubic phase transition was observed at 49.8 °C (at 100% RH). The corresponding lamellar repeat distances were also determined.

5.2.2 DSC and PPC Measurements

Differential scanning calorimetry (DSC) and pressure perturbation calorimetry (PPC) were used to characterize thermal phase transitions, membrane packing and volumetric properties in multilamellar vesicles (MLVs) composed of the polar lipid fraction E (PLFE) isolated from the thermoacidophilic archaeon *Sulfolobus acidocaldarius* grown at a temperature of 65 °C.

5.2.3 DSC Thermograms Measured at pH 7.0 for PLFE MLVs Derived From Cells Grown at 65 °C

The effect of pH on the DSC thermograms for PLFE MLVs derived from the cells grown at 65 °C was examined. Figure 5.12 shows three consecutive DSC heating scans measured at pH 7.0. The first heating scan in this figure shows one endothermic peak (lamellar-to-lamellar) centered at 43.7 °C and a broad exothermic peak (lamellar-to-cubic phase) at 85.5 °C. Figure 5.12 also shows that the high-temperature exothermic transition (at 85.5 °C) in PLFE MLVs at pH 7.0 disappears in the second and third heating scan. The ΔH value for the lamellar-to-lamellar transition in PLFE MLVs at pH 7.0 (Peak 1 in Fig. 5.12) is 10.0-16.0 kJ/mol (Table 5.3).

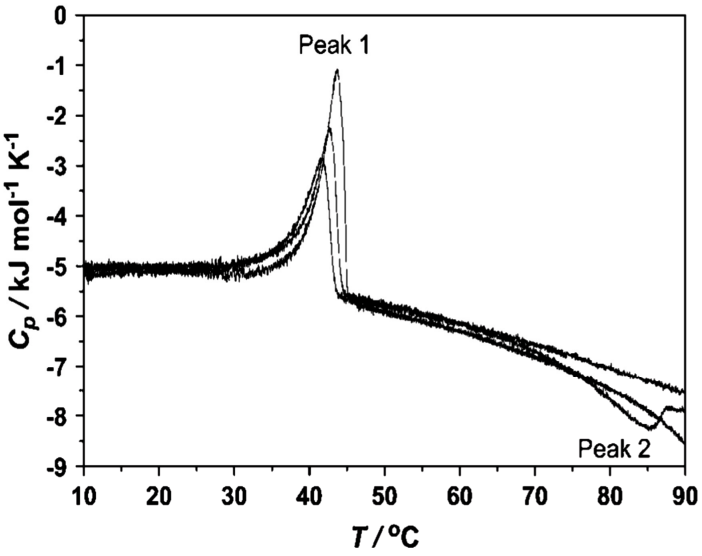

Figure 5.12: DSC profiles, measured at pH 7.0, of PLFE MLVs derived from cells grown at 65 °C.

The parameters associated with the endothermic lamellar to-lamellar phase transition in all three scans in Figure 5.12 are given in Table 5.3. The ΔH value of this phase transition is 10.0–16.0 kJ/mol, which is ~2-3 times higher than that of the corresponding transition in PLFE MLVs derived from cells grown at 78 °C (3.5-4.2 kJ/mol, [Chong 2005]).

Table 5.3: DSC and PPC parameters of PLFE MLVs derived from cells grown at 65 °C

		Peak 1	
DSC (pH 7.0)	T_{tr} (°C)	ΔH (kJ/mol)	$T_{1/2}$ (°C)
Scan 1	43.7	16.0	3.14
Scan 2	42.8	12.1	3.12
Scan 3	41.7	10.0	4.33
		Peak 1	
PPC	T_{tr} (°C)	$\Delta V/V$ (%)	$T_{1/2}$ (°C)
pH 7.0	43.0	0.56	4.0
pH 2.1	42.0	0.25	4.0

Again, the increase in ΔH with decreasing cell growth temperature can be explained by a decrease in the number of cyclopentane rings at a lower growth temperature, as discussed earlier. Taken together, it appears that the cell growth temperature (or, inferentially, the number of cyclopentane rings) is an important factor governing the thermodynamic properties of PLFE lipid membranes.

5.2.4 PPC Scans Measured at pH 7.0 and 2.1 for PLFE MLVs Derived from Cells Grown at 65 °C

PPC measurements were also performed on PLFE MLVs derived from cells grown at 65 °C. A decrease in growth temperature should decrease the number of cyclopentane rings in the dibiphytanyl chain of PLFE lipids [Lo 1990]. It is then of interest to know how this structural change affects $\Delta V/V$ in PLFE liposomes. $\Delta V/V$ can originate from the volume change in the dibiphytanyl (hydrophobic) regions, from the polar headgroup regions where it has been suggested that an extensive hydrogen-bond network exists [Elferink 1993, Vilalta 1996], or from both. In the polar headgroup regions, the changes in PLFE hydration could contribute to the change in the partial specific volume of PLFE. For PLFE MLVs derived from cells grown at 65 °C, the temperature dependence of α shows only one transition (~42-43 °C) (Fig. 5.13) with

$\Delta V/V$ values of 0.56% (measured at pH 7.0) and 0.25% (measured at pH 2.1) (Table 5.3)

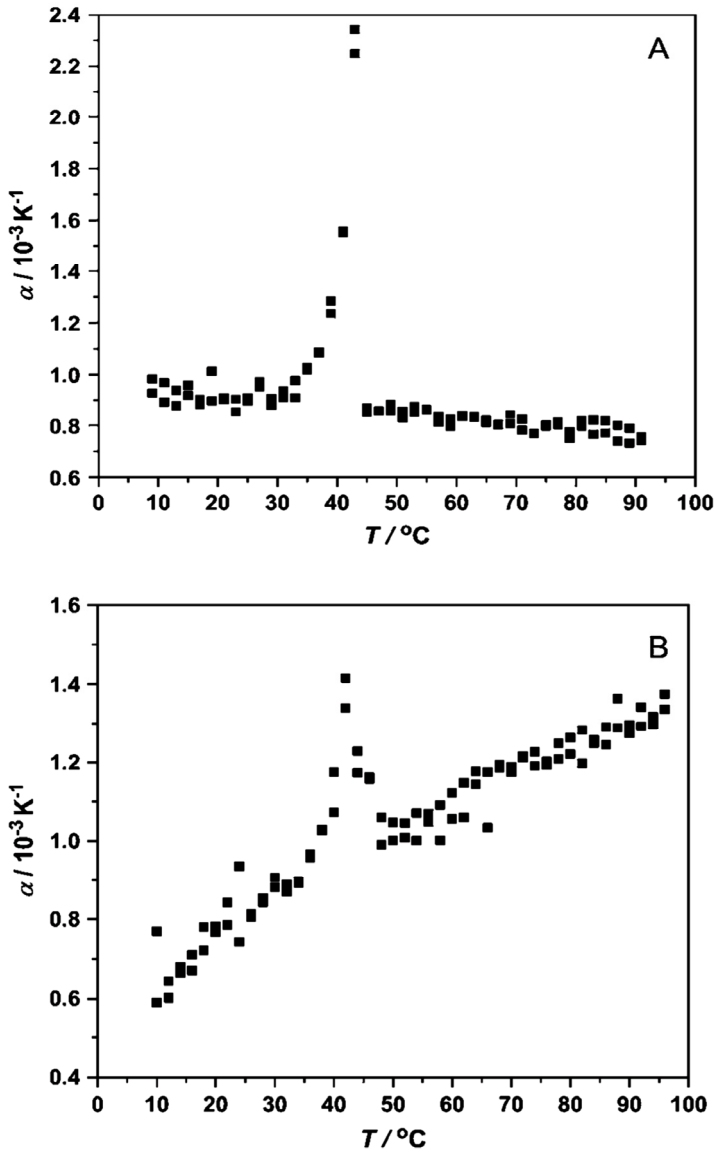

Figure 5.13: Plot of thermal expansion coefficient α versus temperature of PLFE liposomes at (A) pH 7.0 and (B) pH 2.1. PLFE was derived from cells grown at 65 °C.

As mentioned earlier, the first heating DSC scan of this sample (Fig. 5.12 for measurement at pH 7.0) shows one endothermic peak centered at 43.7 °C (pH 7.0) due to a lamellar-to-lamellar phase transition and a broad exothermic peak at 85.5 °C (pH 7.0) due to a lamellar-to-cubic phase transition. Thus, the PPC plot presented in

Figure 5.13 is consistent with the DSC data and shows once again that the lamellar-to-cubic phase transition detected at high temperatures (85.5 °C) in the DSC thermograms (Fig. 5.12) does not involve any significant volume change. The $\Delta V/V$ value of the phase transition measured at pH 2.1 (0.25%) is ~2.1 times smaller than that measured at pH 7.0 (0.56%), suggesting that a decrease in pH from 7.0 to 2.1 tightens membrane packing. As previous molecular modeling study [Gabriel 2000] suggested, a decrease in the number of cyclopentane rings will make the PLFE membrane less tight and less rigid. Thus, it is reasonable that a higher $\Delta V/V$ is detected for the phase transition in PLFE MLVs derived from a lower growth temperature. A smaller $\Delta V/V$ for the phase transitions of lipid membranes derived from thermoacidophilic cells grown at a higher temperature explains why those cells can sustain a range of high growth temperatures without having membrane disruptions [Chong 2005].

5.2.5 Temperature Dependence of Thermal Expansion Coefficient (α) in PLFE MLVs

In addition to $\Delta V/V$ through the phase transitions, PPC measurements provide information on the temperature dependence of the thermal expansion coefficient α. For PLFE MLVs derived from cells grown at 65 °C, the decrease of α (measured at pH 7.0) with temperature is much less steep (Fig. 5.13 A), changing from ~0.95×10^{-3} K^{-1} at 10 °C to 0.75×10^{-3} K^{-1} at 90 °C. In this case, the negative slope of α versus temperature can be attributed to the release of some water from the polar headgroups. However, when measured at pH 2.1, PLFE MLVs derived from cells grown at 65 °C exhibit an increase of α with increasing temperature (Fig. 5.13 B). The effect of pH on the temperature dependence of α revealed in Figure 5.13, A and B, may be due to changes in polar headgroup hydration and conformation as a result of changes in the degree of ionization on the phosphoinositol moiety of PLFE lipids. As the pH is changed from 2.1 (Fig. 5.13 B) to 7.0 (Fig. 5.13 A), the phosphoinositol group becomes more negatively charged, which would increase the hydration layer. Then,

more water can be steadily released with increasing temperature, producing a negative slope in the plot of α versus temperature (Fig. 5.13 A). It is interesting to note that whereas PLFE (a mixture of bipolar tetraether lipids) MLVs exhibit a negative slope in the plot of α versus temperature in some cases (Fig 5.13 A), monopolar diester liposomes usually yield a positive slope. Using the same PPC technique, Heerklotz and Seelig [Heerklotz 2002] showed that α was 0.7×10^{-3} K^{-1} below the pretransition and 0.9×10^{-3} K^{-1} above the main transition for DMPC MLVs. A similar positive slope of α versus temperature in DPPC vesicles was found in our study (Fig. 5.14). This positive slope was also found in unsaturated monopolar diester liposomes made of 1-palmitoyl-2-oleoyl-L-α-phosphatidylcholine and dioleoyl-L-α-phosphatidylcholine [Heerklotz 2002] and detected by non-PPC volumetric measurements on DMPC MLVs [Böttner 1993].

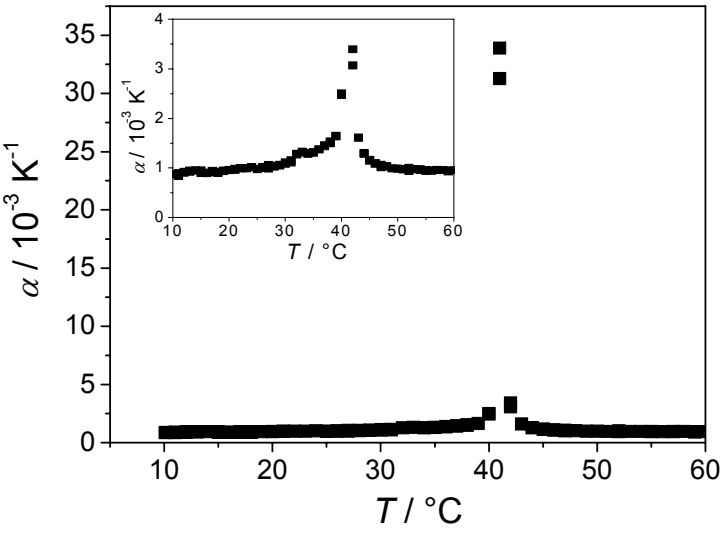

Figure 5.14: Plot of thermal expansion coefficient α versus temperature of DPPC vesicles (pH 7.0). Inset: expansion of the low-α data before and after the main transition temperature.

5.2.6 DSC Thermograms Measured in Pure Water for PLFE MLVs Derived from Cells Grown at 65 °C

Figure 5.15 shows three consecutive heating DSC scans of MLVs composed of PLFE lipids isolated from *S. acidocaldarius* grown at 65 °C. The sample was measured in pure water.

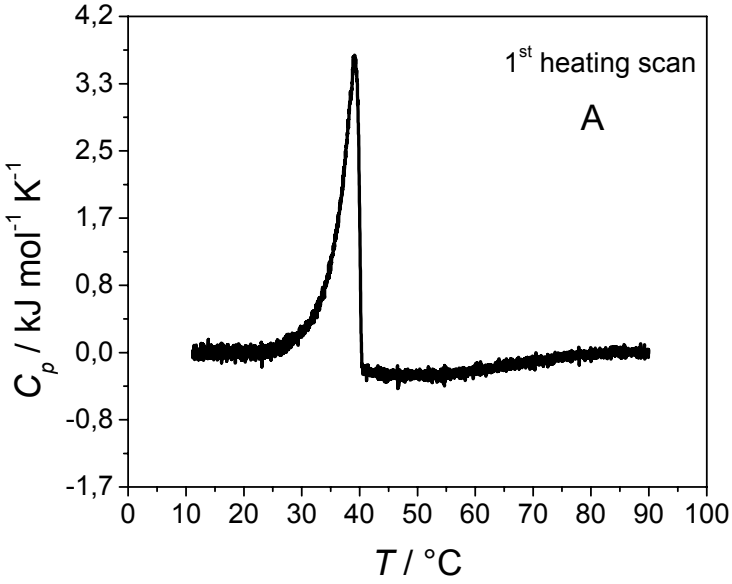

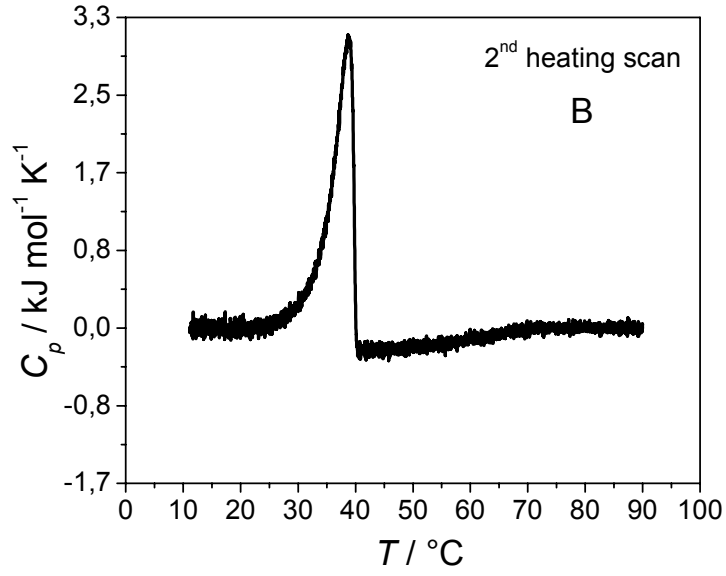

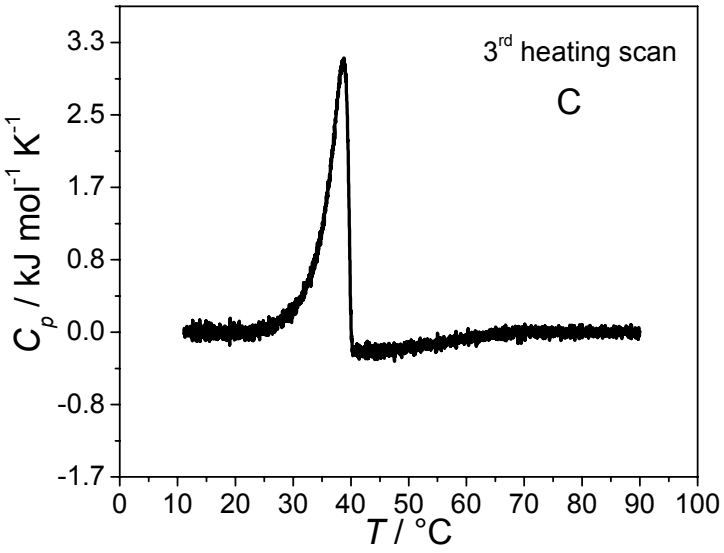

Figure 5.15: DSC profiles measured in pure water: first heating scan (A) second heating scan (B) and third heating scan (C) of PLFE MLVs derived from cells grown at 65 °C.

The first scan displays an endothermic peak at ~39 °C, which is in good agreement with the lamellar-to-lamellar phase transition that is observed at pH 7.0 but at slightly different T_{tr} values (Table 5.3). The transition temperature changes a little from ~39 to 38.5 °C in three consecutive heating scans (Fig. 5.15). In addition to the transition temperature (T_{tr}), the DSC thermograms have been used to determine the enthalpy change (ΔH) of the phase transition (Table 5.4). The ΔH value of the endothermic peak in all three heating scans obtained from PLFE MLVs (Table 5.4) is ~4 times smaller than that for the main phase transition of MLVs composed of dimyristoyl-L-α-phosphatidylcholine (DMPC) [Koynova 1998] and DPPC [Mabrey 1976] respectively. The low ΔH value for PLFE MLVs suggests that the lamellar-to-lamellar phase transition involves restricted trans-gauche conformational changes in the PLFE dibiphytanyl chains due to the presence of the cyclopentane ring, branched methyl groups, and the bipolar nature of the PLFE lipids, and due to the spanning of the dibiphytanyl chains through the membrane. The parameters associated with the

endothermic lamellar-to-lamellar phase transition in all three heating scans (Fig. 5.15) are given in Table 5.4.

Table 5.4: DSC and PPC parameters of PLFE MLVs in pure water derived from cells grown at 65 °C

		Peak 1	
DSC (in pure water)	T_{tr} (°C)	ΔH (kJ/mol)	
Scan 1	38.9	11.3±0.09	
Scan 2	38.4	11.0±0.08	
Scan 3	38.45	10.8±0.08	
		Peak 1	
PPC	T_{tr} (°C)	$\Delta V/V$ (%)	$T_{1/2}$ (°C)
Scan 1	38.0	0.45±0.05	3.98
Scan 2	38.0	0.39±0.05	3.99
Scan 3	38.0	0.37±0.05	3.99

5.2.7 PPC Scans Measured in Pure Water for PLFE MLVs Derived from Cells Grown at 65 °C

Figure 5.16 shows the PPC results obtained from PLFE MLVs derived from cells grown at 65 °C. Both DSC and PPC were run at the same effective scan rate (20 °C/h) and the PPC scans were performed at the same sample after the completion of the DSC scans. The plot of the thermal volume expansion coefficient ($\alpha = (1/V)(\partial V/\partial T)_p$) (measured in pure water) versus temperature exhibits a transition at ~38 °C. This transition temperature coincides with the lamellar-to-lamellar phase transition detected by DSC (Fig. 5.15). Interestingly, the PPC measurements reveal a relative volume change ($\Delta V/V$, the area under the peak in the plot of α versus T) of 0.37-0.45% (Table 5.4) for these transitions, shown in Figure 5.16. These $\Delta V/V$ values are much smaller than the $\Delta V/V$ values of the main gel-to-fluid phase transition of saturated diacyl monopolar diester lipids, such as DMPC

(2.8% [Heerklotz 2002]) and DPPC (~3%; see Fig. 5.14 and Table 5.5), and more comparable to the $\Delta V/V$ value (0.03–0.04%) of the pretransition in DPPC vesicles (Table 5.5) determined by the same PPC technique.

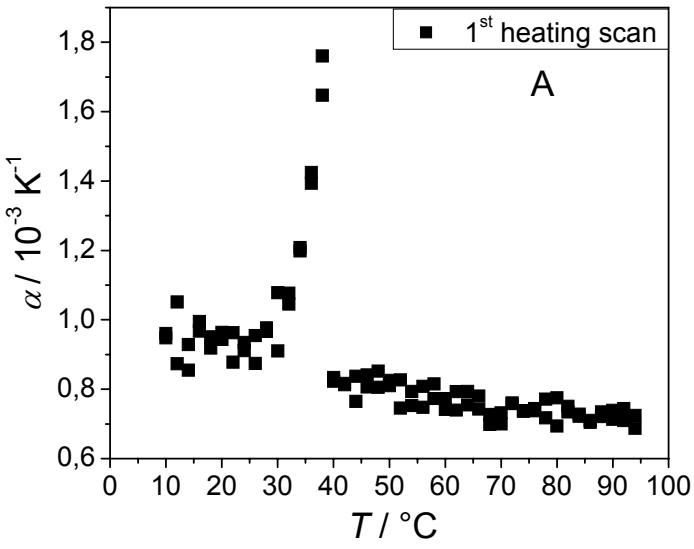

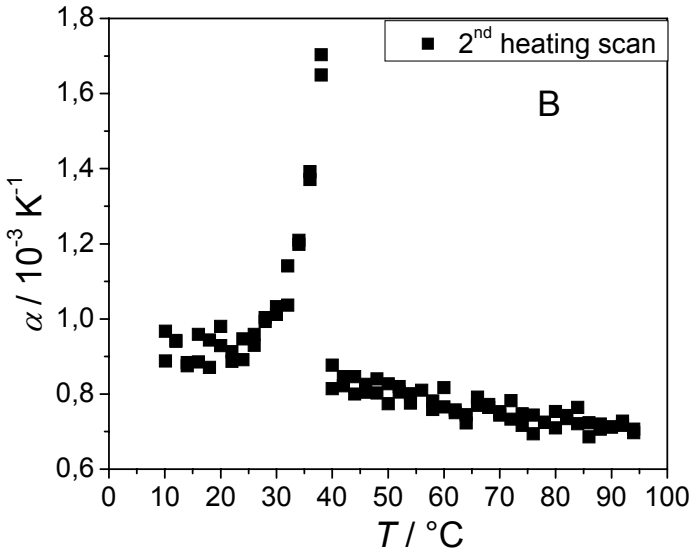

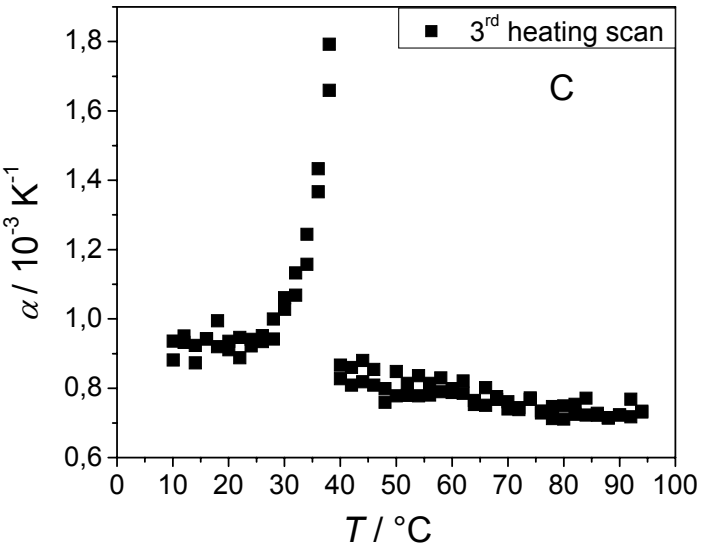

Figure 5.16: Plot of thermal expansion coefficient α versus temperature of PLFE liposomes in pure water, (A) first heating scan, (B) second heating scan, and (C) third heating scan. PLFE was derived from cells grown at 65 °C.

Table 5.5: PPC data of DPPC vesicles at pH 7.0

Peak 1			Peak 2		
T_{pre} (°C)	$\Delta V/V$ (%)	$T_{1/2}$ (°C)	T_m (°C)	$\Delta V/V$ (%)	$T_{1/2}$ (°C)
34.0	0.03-0.04	2.0	41.0	3.0±0.3	1.98

Peak 1 corresponds to the pretransition (at T_{pre}), and Peak 2 to the main phase transition (at T_m).

The relatively low $\Delta V/V$ and small ΔH involved in the phase transitions help to explain why PLFE liposomes are remarkably thermally stable (discussed by Kanichay et al. [Kanichay 2003]) and also echo the proposal that PLFE liposomes are generally rigid and tightly packed [Chang 1994, Bagatolli 2000, Khan 2000].

In summary, the phase transitions of PLFE lipid have been determined from DSC and PPC data. The values of enthalpy changes (ΔH) and the relative volume changes ($\Delta V/V$) at the phase transitions were also determined.

5.2.8 Temperature Dependent FT-IR Spectroscopic Measurements of PLFE in D_2O

FT-IR spectroscopy was used to gather further information about the conformational and molecular order of the acyl chains as well as structural changes of PLFE (growth temp. 65 °C) in excess D_2O. The positions and intensities of IR absorption bands were analyzed to monitor the conformational properties of PLFE [Mantsch 1991, Reis 1996, Reis 1998]. The carbon hydrogen stretching vibrations give rise to bands in the spectral region between 2800 and 3100 cm^{-1}. The CH_2 antisymmetric stretching mode at ~2920 cm^{-1} and the CH_2 symmetric stretching mode at ~2850 cm^{-1} are the strongest bands that can be observed in lipid IR spectra.

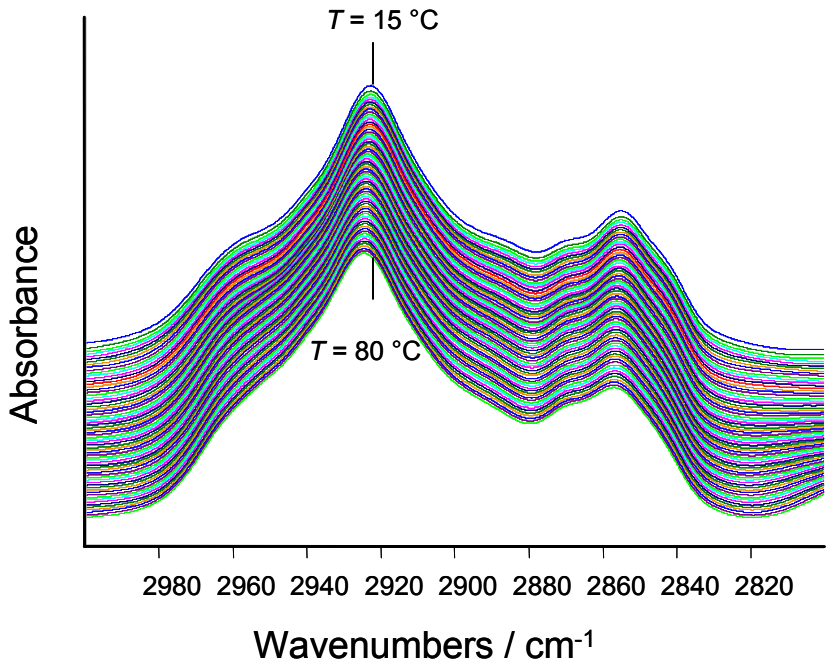

Figure 5.17: Temperature dependence of the IR spectra of PLFE in D_2O in the CH_2 symmetric and antisymmetric stretching mode region

The position of these bands is conformation sensitive and thus provides qualitative information about temperature induced changes of the trans/gauche ratio in the lipid

acyl chains. Temperature dependent measurements were performed in the range 15-80 °C and spectra were recorded in steps of about 1 degree centigrade. Figure 5.17 shows the infrared spectra of PLFE multilamellar dispersions in the wavenumber region from 3000 to 2800 cm^{-1} at different temperatures.

Absorption bands at ~2855 and ~2923 cm^{-1} are assigned to CH_2 symmetric and antisymmetric stretching vibrations of PLFE respectively. The absorption bands in PLFE are much broader in contrast to those of monopolar diester phospholipids [Reis 1996], which might be due to overlapping bands of the lipid components GDNT and GDGT. The biphytanyl chains of PLFE contain also branched methyl groups and cyclopentane rings but their absorption bands could not be detected with sufficient accuracy.

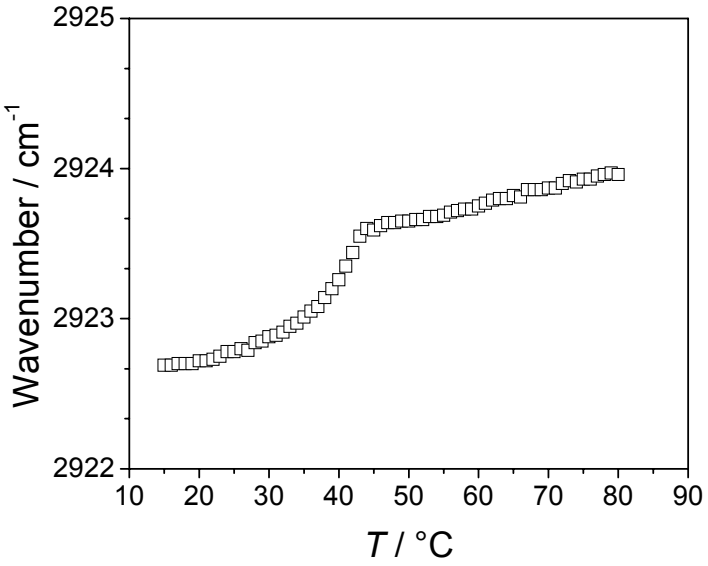

Figure 5.18: Effect of temperature on the wavenumber of the antisymmetric CH_2 stretching mode of PLFE (growth temperature 65 °C) in D_2O

The symmetric and antisymmetric CH_2 stretching frequency as a function of temperature is shown in Figure 5.18 and Figure 5.19.

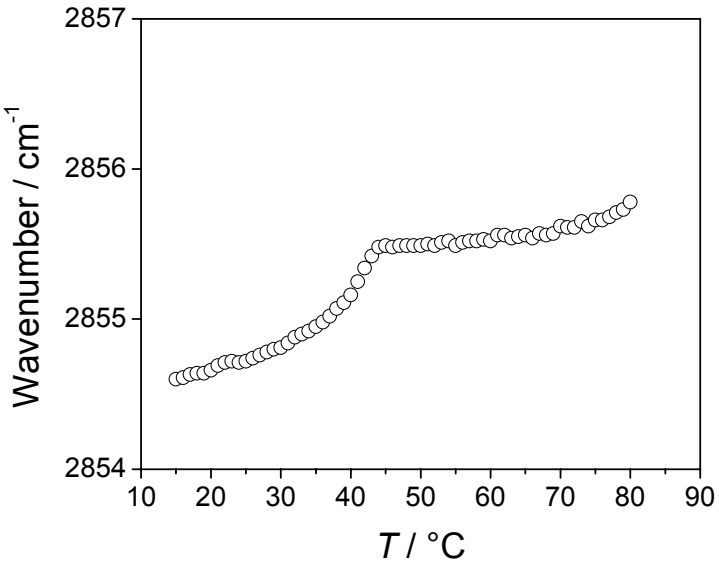

Figure 5.19: Effect of temperature on the wavenumber of the symmetric CH_2 stretching mode of PLFE (growth temperature 65 °C) in D_2O

These studies show that as the temperature increases, the wavenumber of the symmetric and antisymmetric CH_2 vibration increases overall by ~2 cm^{-1} due to increasing elastical repulsive interactions between the lipid chains, indicating a transition from a largely ordered to a conformationally disordered phase at ~ 38 to 40 °C, which is in good agreement with the DSC and PPC measurements performed before.

5.3 The Two Component System DPPC/Ergosterol

Cholesterol and ergosterol are well-known sterols, which play an essential role in the cell membrane of eukaryotic organisms. Sterols are essential components of eukaryotic cells both as structural membrane components and as initiators and regulators of biological processes, and as such regulate membrane fluidity and permeability. The main example from this group of compounds is cholesterol. It is often found distributed non-randomly in domains in biological and model membranes. These domains are believed to be important for the maintenance of membrane structure and function. Lipid lateral organization is an important issue in membrane biophysics because cell membranes are extremely complex; a molecular understanding of membrane lipid lateral organization is a must, which may come from simple model systems such as two-component lipid bilayers as chosen in our studies.

While cholesterol is the major sterol present in plasma membranes of animal cells, ergosterol is the major component present in plant cells such as certain protozoa, yeast, fungi, and in insects such as Drosophila. One of the primary roles of sterol in eukaryotic cells is to modulate the physical properties of the plasma membrane's phospholipid bilayer. Ergosterol is quite similar to cholesterol in structure, but differs from that of cholesterol in having two additional double bonds (at positions C_7 and C_{22}) and a methyl group at C_{24} of the side chain (see Fig. 5.20)

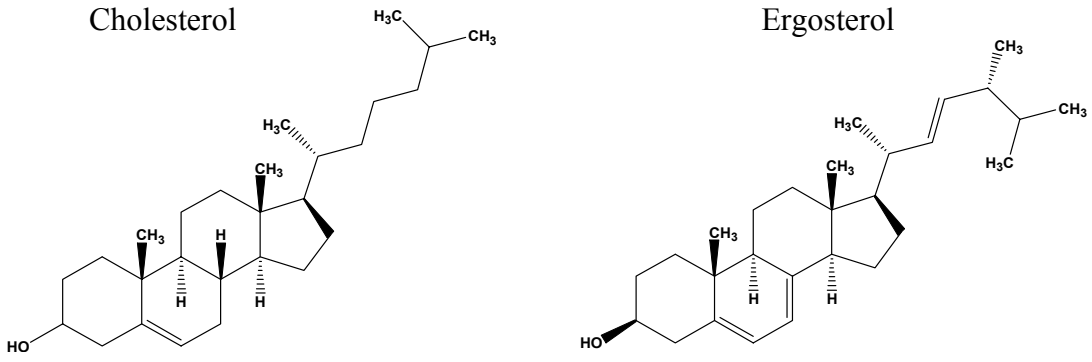

Figure 5.20: Structural formula for cholesterol and ergosterol

Interestingly, lipid rafts have recently been isolated from organisms such as yeast and Drosophila which have ergosterol as their major sterol component [Arora 2004]. Although a detailed biophysical characterization of the effect of cholesterol on membranes is well documented, the effect of ergosterol on the organization and dynamics of membranes has not been studied in detail, especially using small-angle neutron scattering (SANS) and X-ray reflectivity.

In our studies, the DPPC/ergosterol two component model membrane system was used to illustrate the lateral membrane organization, phase behavior and effect of ergosterol on a phospholipid bilayers. DPPC is a well-studied phosphatidylcholine with two 16-carbon saturated acyl chains. Ergosterol was used because its effect on the organization of membranes is not well established.

The gel phase of pure phospholipid bilayers is referred to as the solid ordered (s_o) phase, the liquid crystalline phase of pure lipid bilayers is referred to as the liquid-disordered (l_d) phase, and the β-phase of Vist and Davis [Vist 1990] (which is found at higher cholesterol concentrations) is referred to as the liquid-ordered (l_o) phase. The term solid and liquid are used to characterize the nature of the phase whereas the words ordered and disordered indicate the conformational nature of the lipid acyl chains. Ergosterol stabilizes the liquid-ordered phase in the same manner as cholesterol [Bagnet 2000, Mouritsen 2004]. It is also evident that ergosterol has a multiplicity of functions in the regulation of yeast growth.

5.3.1 X-ray Reflectivity Measurements

The X-ray reflectivity measurements were performed at the synchrotron X-ray wiggler beamline W1.1 at HASYLAB/DESY in Hamburg. At this beamline, the experiments were performed using a wavelength of 1.18 Å. The *Q* range covered for the experiments was from 0.01-0.55 $Å^{-1}$. The measurements were performed on DPPC/ergo samples as a function of temperature and at selected concentrations of ergosterol in DPPC dispersions as shown in Figure 5.21, 5.22 and 5.23.

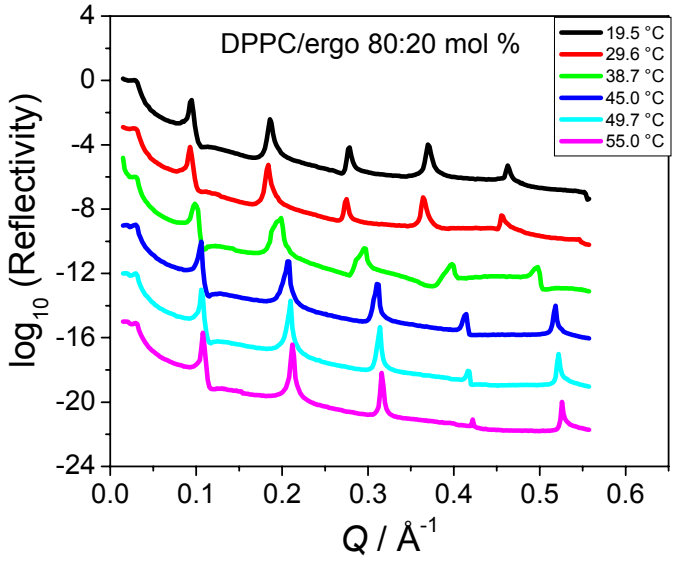

Figure 5.21: X-ray reflectivity measurements of DPPC/ergosterol (80:20 mol%) samples prepared from lipid solutions at a concentration of 20 mg/mL by spin coating. The curves were measured at different temperatures and at full hydration. The curves are shifted vertically for clarity.

In Figure 5.21, the reflected intensity of solid supported membranes of the DPPC/ergo system (80:20 mol%) is plotted as a function of Q, where Q is the momentum transfer vector ($Q = (4\pi/\lambda)\sin\theta$, λ is the wavelength of the radiation used and 2θ is the scattering angle). The reflectivity curve of pure DPPC shows the pretransition at 37 °C and a main transition at 42 °C, respectively (as discussed in section 5.1 on page 48). The lamellar repeat unit increases from ~63 Å in the $L_{\beta'}$ phase to ~67 Å in the ripple gel phase $P_{\beta'}$, and further decreases in the L_α phase to about 59 Å due to the highly disordered chains in the fluid L_α phase at high temperatures.

The reflectivity curves as shown in Figures 5.21, 5.22 and 5.23 are measured on DPPC/ergo systems over a temperature range from 20 °C to 55 °C. Incorporation of ergosterol into DPPC lipid membranes has a drastic effect on their structure and phase behavior. It is generally assumed that addition of sterol causes conformational disorder in phospholipids below their gel to liquid-crystalline phase transition temperature, and increases the rigidity in phospholipids at temperatures above T_m [Winter 2002].

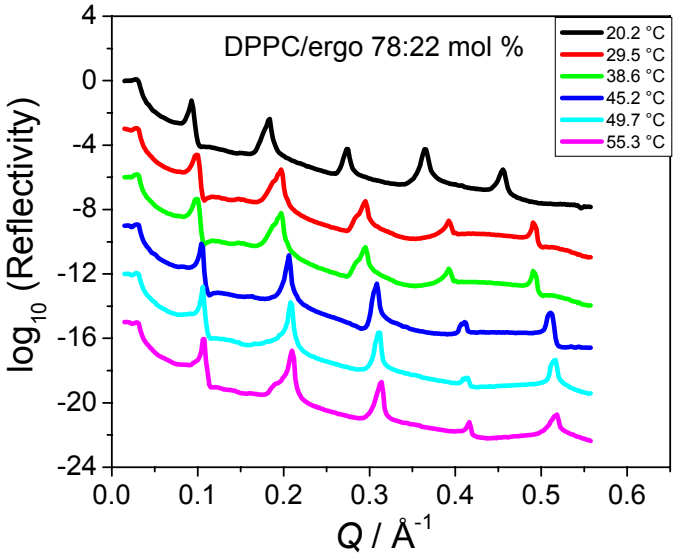

Figure 5.22: X-ray reflectivity measurements of DPPC/ergosterol (78:22 mol%) samples prepared from lipid solutions at a concentration of 20 mg/mL by spin coating. The curves were measured at different temperatures and at full hydration. The curves are shifted vertically for clarity.

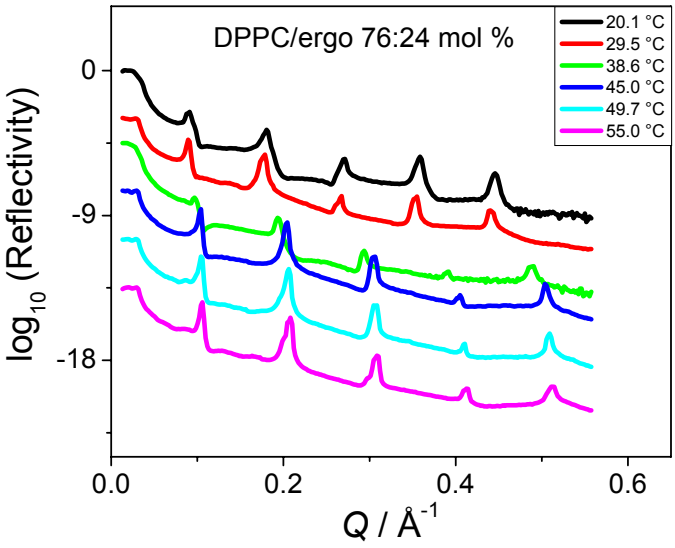

Figure 5.23: X-ray reflectivity measurements of DPPC/ergosterol (76:24 mol%) samples prepared from lipid solutions at a concentration of 20 mg/mL by spin coating. The curves were measured at different temperatures and at full hydration. The curves are shifted vertically for clarity.

The reflectivity curves measured (Figs. 5.21, 5.22, and 5.23) show five orders of Bragg reflections over the whole *Q*-range covered. At temperatures of about 38 °C and 55 °C, two distinguishable Bragg reflections were observed suggesting a two phase liquid ordered/liquid disordered (l_o+l_d) coexistence region, which is in accord with the data from the ^{2}H-NMR spectroscopy studies shown in the phase diagram of DPPC/ergosterol as shown in Figure 5.24 [Hsueh 2005].

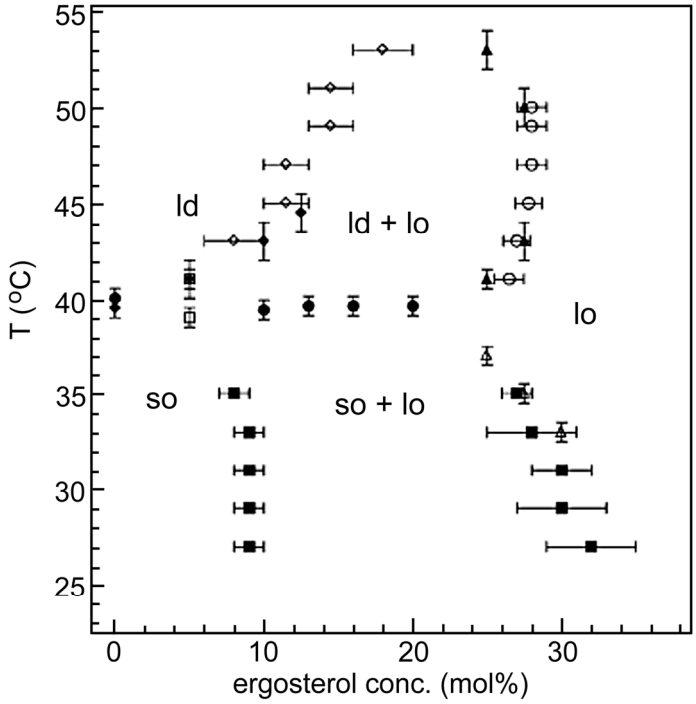

Figure 5.24: Partial phase diagram of the DPPC/ergosterol system developed from ^{2}H-NMR and DSC studies (adapted from [Hsueh 2005]).

The best fit of the reflectivity curve of the 78:22 mol% DPPC/ergo system is obtained by the Parratt program [Parratt 1954] and is shown in Figure 5.25. The simulated curve shows systematic deviations from the measured curve which causes hindrance to obtain a reasonable electron density profile. However the fundamental parameters such as bilayer thickness and water layer thickness can be correctly discerned from the experiments.

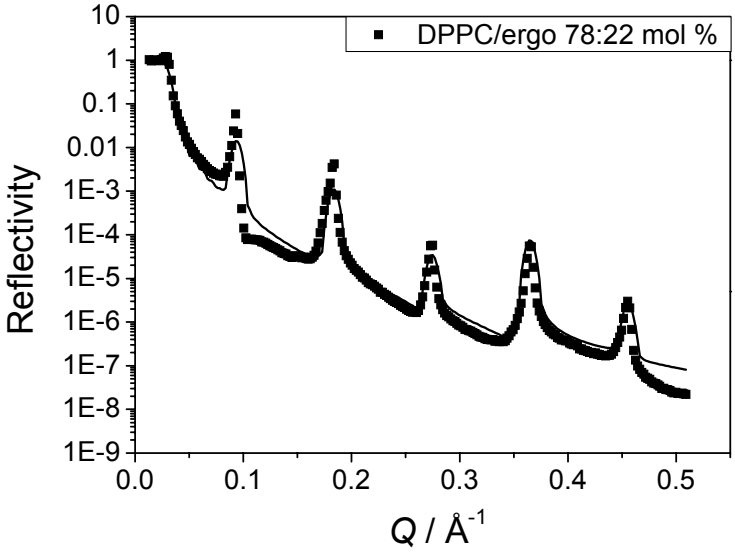

Figure 5.25: X-ray reflectivity curve of 78:22 mol% of the system DPPC/ergo (■) at 100% RH along with the simulated curve by the Parratt program (solid line).

The lamellar repeat distance, *d,* is calculated from the Bragg reflections observed ($Q = 2\pi / d$) and is depicted in Figure 5.26.

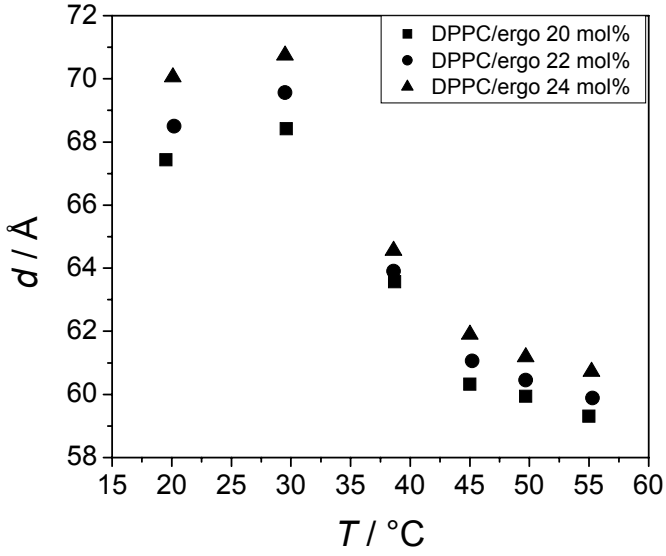

Figure 5.26: Comparison of the temperature dependence of the lamellar repeat unit at a relative humidity of ~100% of the DPPC/ergosterol system at three different ergosterol concentrations in DPPC lipid bilayers. The average value of the highest d-values is calculated and is plotted in this Figure.

The lamellar repeat distance, *d,* comprises the sum of the lipid bilayer thickness and the thickness of one adjacent interlamellar water layer. The lamellar repeat distance increases as the concentration of ergosterol in the DPPC bilayer increases (Fig. 5.26). At low temperatures of about 20 and 30 °C, a large lamellar repeat distance is observed at all the concentrations studied. The lamellar repeat distance, *d*, of 67, 68.5 and 70 Å is observed at ergosterol concentrations of 20, 22 and 24 mol% respectively, indicating the coexistence of a two-phase (s_o+l_o) region at low temperatures. The coexistence of s_o and l_o phases indicates that ergosterol induces l_o domains in the DPPC bilayers. The proportion of the l_o component increases as the ergosterol concentration increases and thus leads to larger lamellar repeat unit. As the temperature increases, the lamellar repeat distance decreases because of the disorder in the lipid acyl chains in the liquid-crystalline or liquid-disordered (l_d) phase. A minimum lamellar repeat distance of ~60 Å is observed at ~55 °C and two distinguishable Bragg reflections were also observed at the same temperature and at a concentration of 22 and 24 mol% of ergosterol in DPPC bilayers, which according to the phase diagram presented in Figure 5.24 comprises liquid ordered/liquid disordered (l_o+l_d) coexistence region.

5.3.2 Small-Angle Neutron Scattering (SANS) Experiments

The aim of this study was to explore how the phase behavior of the system DPPC/ergosterol changes with respect to the concentration of the ergosterol and temperature, and the second aim was to contribute to the molecular level understanding of the lateral organization of phase-separated binary-lipid mixtures exhibiting strong non-ideal mixing behavior by direct structural measurements. To address this problem, small-angle neutron scattering (SANS) measurements in combination with the H/D contrast variation technique were performed. Neutron scattering allows the detection of short-lived structural features with lifetimes of picoseconds, and the contrast variation technique has already proven to be a very

powerful technique for the analysis of phase separation phenomena in lipid bilayers [Knoll 1981].

The SANS measurements were performed at the SANS-II diffractometer (λ = 6.37 Å) of the Swiss Spallation neutron source at the Paul Scherrer Institute (PSI), Switzerland. Neutron scattering in combination with the H/D contrast variation technique was applied to study the compositional fluctuations and lateral organization of the binary lipid mixture 1, 2-dipalmitoyl-*sn*-glycero-3-phosphocholine and ergosterol (DPPC/ergo) as a function of temperature and concentration. One of the lipid components DPPC, was, deuterated in part, thus having a relatively high scattering length density (ρ (DPPC-d_{62}) = 5.087 × 10^{10} cm^{-2}), whereas the scattering length density of ergosterol was significantly lower due to the smaller scattering length density of H-atoms (ρ (ergosterol-H) = 0.415 × 10^{10} cm^{-2}). The desired concentration mixtures of DPPC-d_{62} and ergosterol, characterized by a mean scattering length density (details in Table 4.4 of section 4.7), were then dispersed in a H_2O-D_2O solvent mixture of the same scattering length density. Under these so called matching conditions, scattering arises essentially from the inhomogeneous distribution of the lipid components in the vesicles.

The range of momentum transfer was 0.005-0.05 $Å^{-1}$, covering a range of lengths of 1256-125 Å (length $2\pi / Q$). The differential scattering cross section per unit volume of the sample can be written as

$$\frac{d\Sigma}{d\Omega} = (\Delta\rho)^2 V_p^2 P(Q) S(Q), \qquad (5.1)$$

where V_p denotes the particle volume, and $\Delta\rho = \rho_p - \rho_s$ the contrast, i.e., the difference in mean scattering length density of the particles (ρ_p) and the solvent (ρ_s). $P(Q)$ is the form factor of the particles, and $S(Q)$ is the structure factor describing the spatial distribution of the particles. By setting $P(Q) = 1$, we treat the

molecules as point particles and the sample as consisting of two phases, each of which has a constant scattering length density, described by $S(Q)$.

To measure quantitatively the randomness of samples, the concept of fractal geometry is commonly used. For 3-dimensional fractal objects, which show self-similarity over a range of length scales, the structure factor can be deduced as [Czeslik 1997, Winter 1999]:

$$S(Q) = 1 + \frac{1}{(Qa)^{D_m}} \frac{D_m \Gamma(D_m - 1)}{\left(1 + \frac{1}{Q^2 \xi^2}\right)^{(D_m - 1)/2}} \sin\left[(D_m - 1)\arctan(Q\xi)\right] \qquad (5.2)$$

where $\Gamma(x)$ is the gamma-function and D_m is the fractal dimension for the so-called mass fractals which relates the size r of the object to its total mass $(m \propto r^{D_m})$. $S(Q)$ reduces to

$$S(Q) \propto Q^{-D_m}, \qquad (5.3)$$

when $\xi^{-1} < Q < a^{-1}$; ξ is the cut-off distance of the fractal object and a is the characteristic dimension of the individual scatterers. For scattering from 3-dimensional objects with fractal surfaces, having the property that the surface area varies as a non-integer power of length, the power law exponent in Eq. (5.3) is replaced by $-(6 - D_s)$, where D_s is the fractal dimension of the surface $(2 \le D_s < 3)$. $D_s = 2$ represents a smooth surface.

For analysis of critical concentration fluctuations of correlation length ξ, the Ornstein-Zernike approximation [Damay 1984] is generally used, which relates $S(Q \to 0)$ to the concentration-concentration structure factor $S_{CC}(0)$, the isothermal compressibility χ_T and the correlation length ξ of the concentration fluctuations:

$$S(Q \to 0) \approx 1 + \frac{A n_p k_B T \chi_T + B^2 n_p^2 S_{cc}(0) - 1}{1 + Q^2 \xi^2}. \qquad (5.4)$$

A and B are constants containing the scattering lengths and partial molar volumes of the components. The isothermal compressibility term can often be neglected.

The measured intensity distributions were corrected for absorption, sample thickness, inelasticity and background. The background has been subtracted from the data by taking into consideration the lowest curve from all the concentrations at different temperatures. The linear fit is obtained from the Q range 0.025-0.05 $Å^{-1}$ for the background. The value of the intercept and slope obtained from the linear fit in this Q range is used to calculate the intensity over the whole Q range studied for all the measurements. This method was used to overcome the problem of negative counts of the measured intensity data, and was needed to analyze the data accurately. The negative counts obtained were due to the very weak scattering of the samples and has statistical reasons. It simply means (in our case), that the matching of the samples was that perfect that sometimes the electronic noise, sample cell and other background contributions were slightly larger than the measured signal simply due to poor statistics.

Figures 5.27, 5.28 and 5.29 show the SANS curves for the DPPC/ergo mixtures at different concentrations of incorporated ergosterol and at selected temperatures (below and above the melting transition temperature T_m of DPPC-d_{62} (T_m ~39 °C)). The studies carried out at these temperatures lie within the two phase regions of all the samples, as known from the phase diagram presented in Figure 5.24.

It is clearly seen from Figure 5.27 that the largest scattering is observed at a temperature of 25 °C. As the temperature increases, the scattering intensity decreases. At 25 °C, the solid ordered/liquid ordered (s_o+l_o) two phase region exists, and as the temperature increases, the solid ordered phase (s_o) of the DPPC/ergo system changes to the liquid-crystalline or liquid-disordered (l_d) phase thus leading to a (l_o+l_d) two phase region, which is in accord with the phase diagram shown in Figure 5.24.

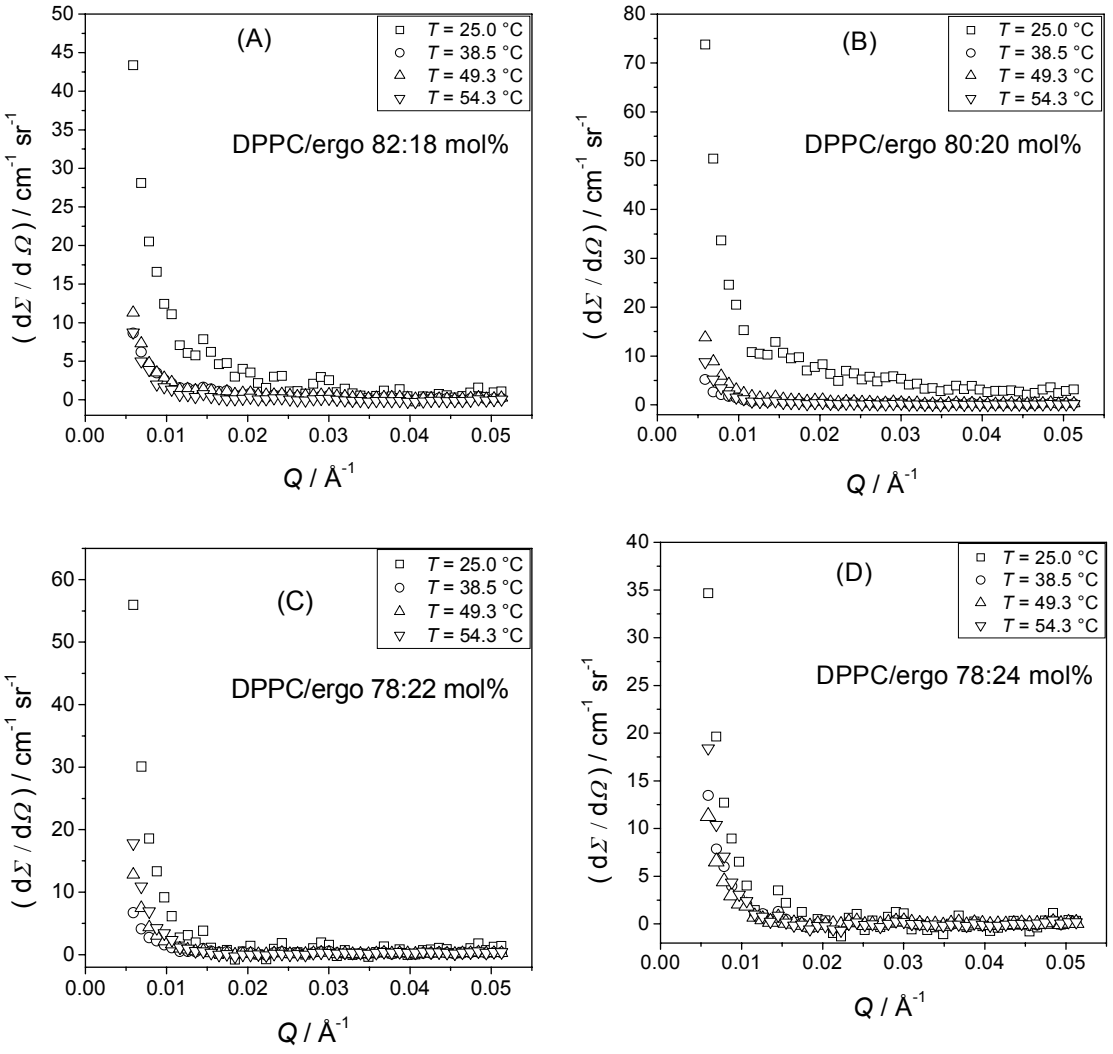

Figure 5.27: Temperature dependent SANS diffraction patterns ($d\Sigma/d\Omega$) of the DPPC(d)/ergo(h) system at selected concentrations of ergosterol: (A) at 82:18 mol%, (B) at 80:20 mol%, (C) at 78:22 mol%, and (D) at 76:24 mol%. All the measurements were performed in a contrast-matched H_2O/D_2O solvent mixture (Details in section 4.7)

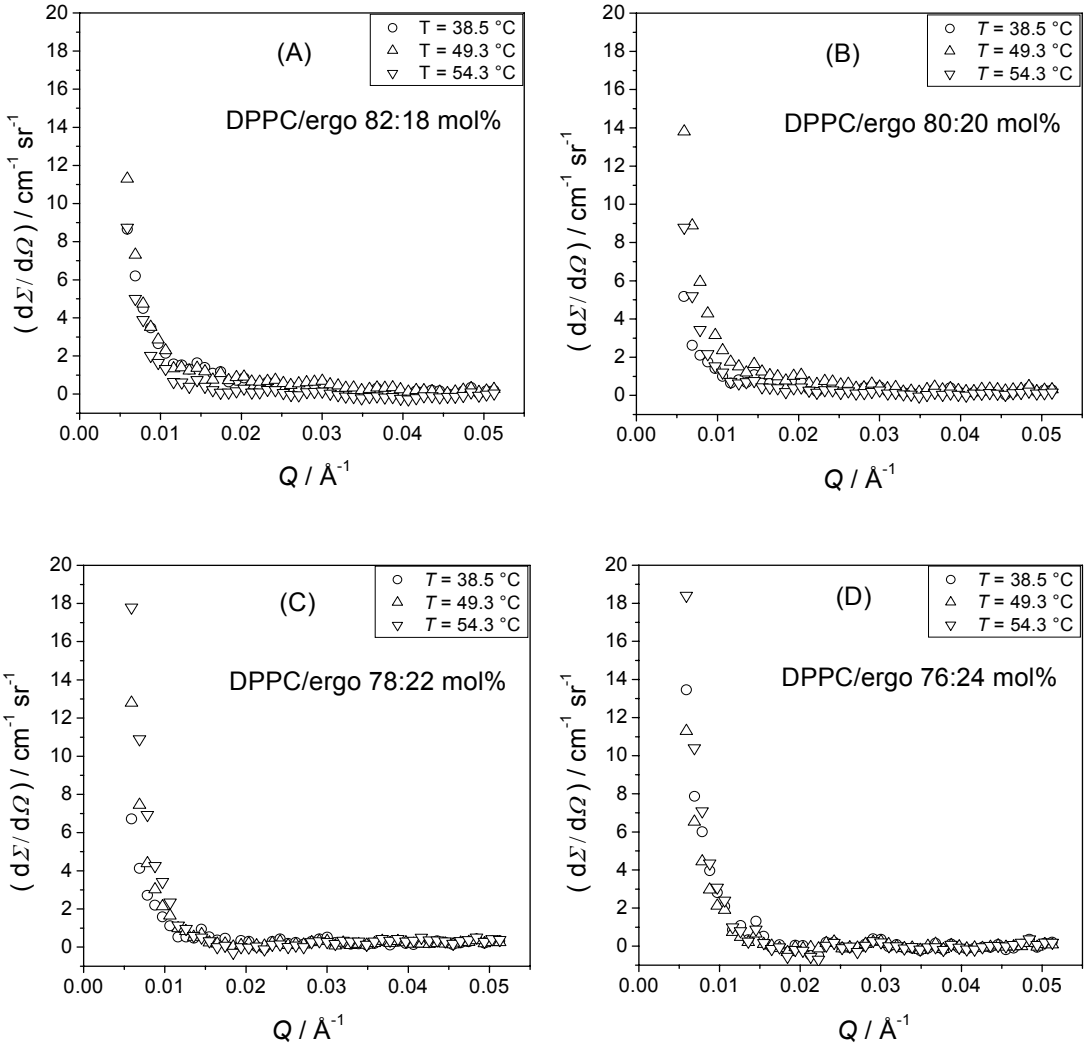

Figure 5.28: Temperature dependent SANS diffraction patterns ($d\Sigma/d\Omega$) of the DPPC(d)/ergo(h) system at selected concentrations of ergosterol: (A) at 82:18 mol%, (B) at 80:20 mol%, (C) at 78:22 mol%, and (D) at 76:24 mol%. All the measurements were performed in a contrast-matched H_2O/D_2O solvent mixture

The scattering at high temperatures as shown in Figure 5.28, which, according to the phase diagram presented in Figure 5.24 should comprise a (l_d+l_o) two phase region. Rather high scattering at ~54.3 °C (for the 78:22 and 76:24 mol% of DPPC/ergo

mixtures) is observed as shown in Figure 5.28, which may be due to the critical like composition fluctuations present.

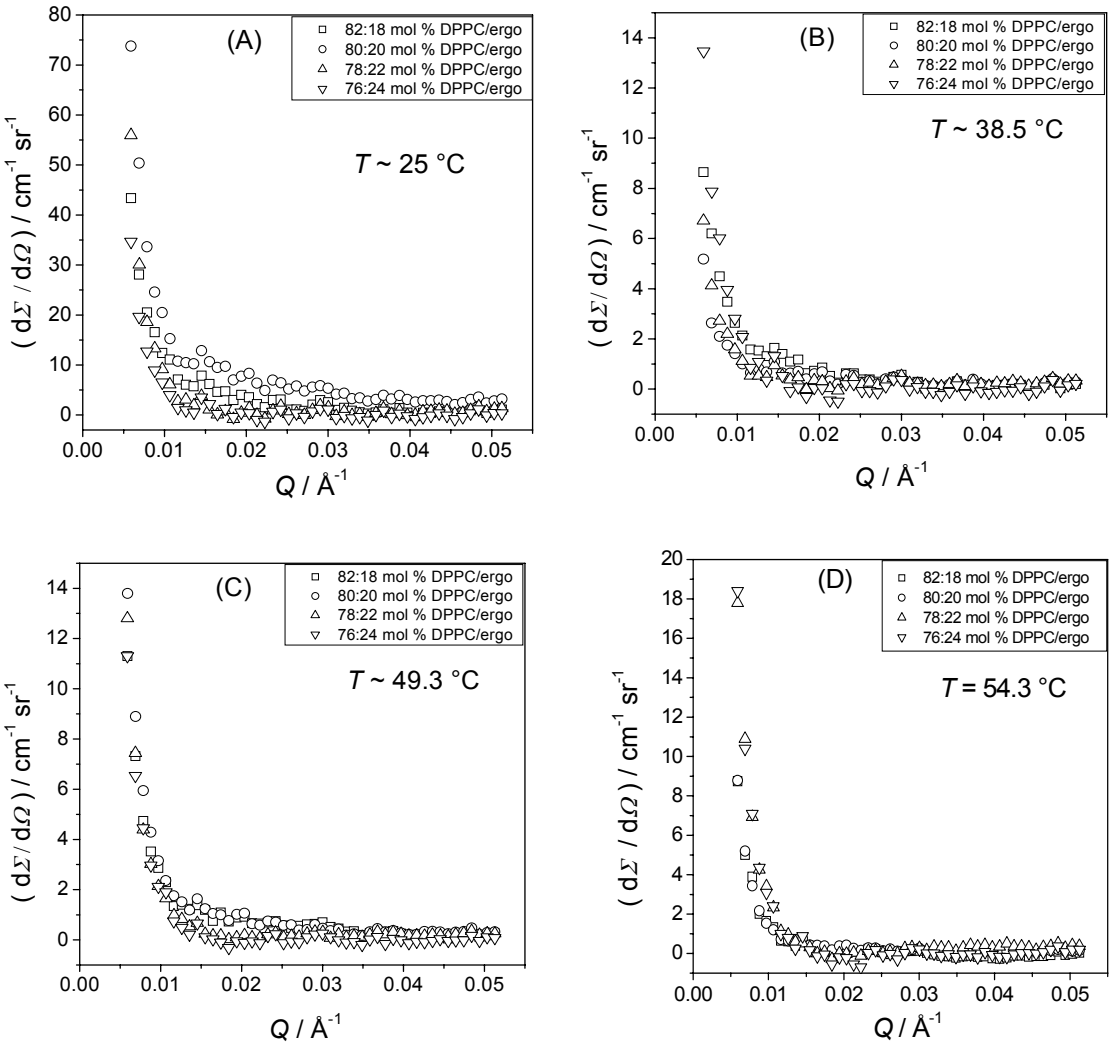

Figure 5.29: Concentration dependent SANS diffraction patterns ($d\Sigma/d\Omega$) of the DPPC(d) /ergo(h) system at selected temperatures: (A) at 25 °C, (B) at 38.5 °C, (C) 49.3 °C, and (D) at 54.3 °C. All the measurements were performed in a contrast-matched H_2O/D_2O solvent mixture

Figure 5.29 shows the SANS curves plotted as a function of concentration of ergosterol in DPPC multilamellar vesicles (MLVs). It can be clearly seen that with increasing temperature the scattering intensity of 78:22 and 76:24 mol% of the DPPC/ergo system also increases.

The Ornstein-Zernike law (plots of $(d\Sigma/d\Omega)^{-1}$ vs Q^2, (Eq. 5.4)), which represents the critical concentration fluctuations, does not hold in the Q range covered (Fig. 5.30) and indicates the absence of a classical bulk critical point in the phase diagram of the DPPC/ergo binary mixture (Fig. 5.24) in the temperature/concentration range covered. If critical fluctuations are present, then an extrapolation of the curve in the Ornstein-Zernike plot to $(d\Sigma/d\Omega)^{-1} = 0$ on the $-Q^2$ axis will yield the ξ-value of critical like composition fluctuations [Nicolini 2004]. In our case, no such behavior is observed, indicating that such kind of critical-like spatial composition fluctuations is not present in these systems at the concentrations and the temperatures measured.

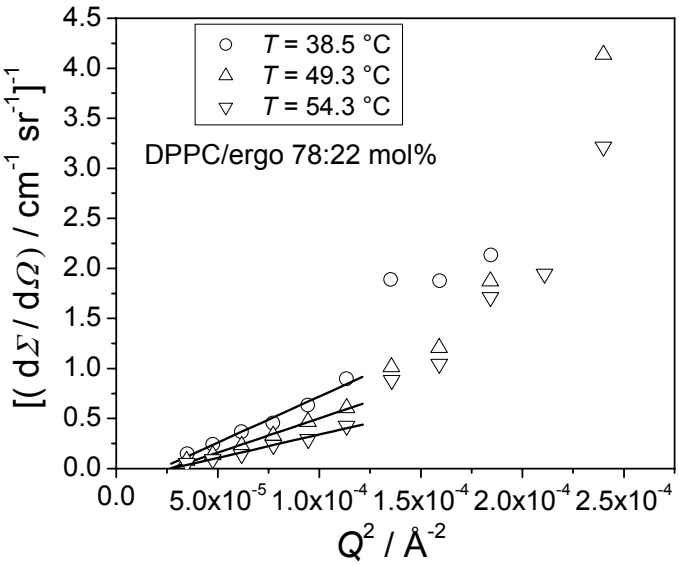

Figure 5.30: Ornstein-Zernike plot, $(d\Sigma/d\Omega)^{-1}$ vs. Q^2, of the SANS curves of DPPC/ergo 78:22 mol% at selected temperatures (10 wt% aqueous lipid dispersion, under H/D contrast matching conditions). If the Ornstein-Zernike law holds, extrapolation of the experimental curve to $(d\Sigma/d\Omega)^{-1} = 0$ on the $-Q^2$ axis will yield the correlation length ξ of critical-like composition fluctuations. In our studies, no such behavior is observed, indicating that such kinds of fluctuations are not present here.

Interestingly, however, ln(dΣ/dΩ) vs ln(Q) plots (see Eq. (5.3)) give straight lines inside the two phase (l_o+l_d) coexistence region over the whole Q-range covered where the maximum scattering is observed as shown in Figure 5.31.

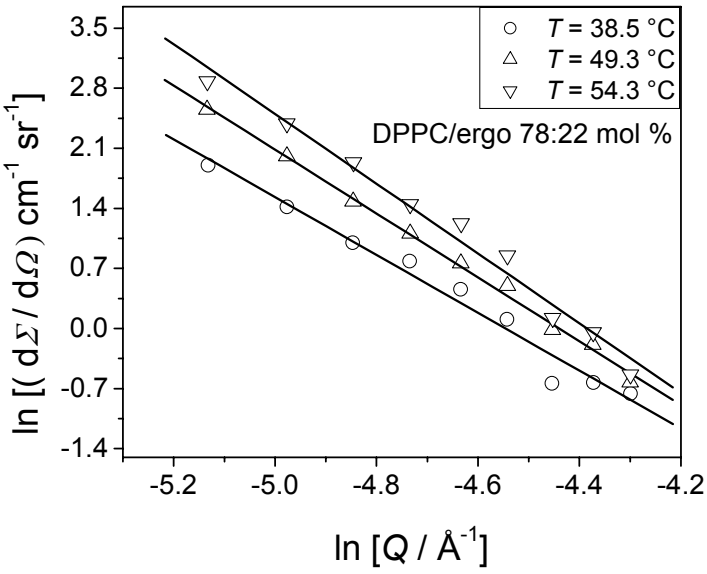

Figure 5.31: Double logarithmic plots (ln(dΣ/dΩ) vs ln(Q)) of the SANS curves of the system 78:22 mol% DPPC/ergo at selected temperatures. The line is a fit to the linear part of the data points (slope for T = 38.5 °C: -3.37 ± 0.1, for T = 49.3 °C: -3.72 ± 0.1, for T = 54.3 °C: -3.7 ± 0.3).

This diffuse scattering pattern is indicative of a fractal like behavior of the sample. If the value of the slope is between 3 and 4 ($2 < D_s < 3$), the domains are compact clusters whose surface scales are independent of the mass (surface fractals) [Winter1999]. From the double-logarithmic plot, a slope of -3.37 ± 0.1, -3.72 ± 0.1 and -3.7 ± 0.3 (at 38.5, 49.3 and 54.3 °C of the system 78:22 mol% DPPC/ergo) is obtained which corresponds to surface fractal dimensions D_s of 2.63 ± 0.1, 2.28 ± 0.1 and 2.3. ± 0.3, respectively. These fractal dimensions were calculated from the slope

of the linear plots as shown in Figure 5.31 for the system 78:22 mol% DPPC/ergo. The results of all measurements are listed in Table 5.6.

Table 5.6: Values of the slope of the double-logarithmic plot by performing a linear fit (of different DPPC/ergo concentrations at different temperatures) and the calculated dimensions D_s for surface fractals and D_m for mass fractals. N.A. means linear fit at that concentration and temperature is not applicable.

DPPC/ergo	T / °C	Slope	D_m	D_s
82:18	25.0	-2.48 ± 0.1	2.48 ± 0.1	
82:18	38.5	-2.34 ± 0.1	2.34 ± 0.1	
82:18	49.3	-2.75 ± 0.1	2.75 ± 0.1	
82:18	54.3	N.A.	-	
80:20	25.0	-2.53 ± 0.2	2.53 ± 0.2	
80:20	38.5	-2.4 ± 0.3	2.4 ± 0.3	
80:20	49.3	-2.96 ± 0.1	2.96 ± 0.1	
80:20	54.3	-3.31± 0.2		2.69 ± 0.2
78:22	25.0	-4.05 ± 0.1		1.95 ± 0.1
78:22	38.5	-3.37 ± 0.1		2.63 ± 0.1
78:22	49.3	-3.72 ± 0.1		2.28 ± 0.1
78:22	54.3	-3.7 ± 0.3		2.3 ± 0.3
76:24	25.0	N.A.		-
76:24	38.5	-4.05 ± 0.4		1.95 ± 0.4
76:24	49.3	-3.2 ± 0.4		2.8 ± 0.4
76:24	54.3	-4.1± 0.3		1.9 ± 0.3

In these studies, a fractal-like behavior is observed in the thermodynamic region of the binary lipid mixtures investigated.

5.4 The Three component System POPC/SM/Chol ("Lipid Raft" Mixture)

In recent years, increasing evidence has accumulated for the existence of lipid microdomains in cell membranes called lipid rafts. These lipid rafts may play an important role in many biological processes, such as signal transduction, apoptosis, cell adhesion and protein sorting [Simons 1997, Anderson 2002, Munro 2003, Janosch 2004]. Membrane proteins and lipidated peptides or proteins would either reside in or be excluded from these rafts, depending on their physico-chemical properties. Hence, it is important to study their properties, such as the lateral organization, structure of lipid rafts and their influence on the conformation and activity of membrane proteins etc. A suitable model system for studying biophysical properties of lipid rafts are lipid vesicles composed of three component lipid mixtures, such as POPC/Sphingomyelin/Cholesterol [Dietrich 2001, de Almeida 2003], which exhibit a rich phase diagram, including raft-like liquid-ordered/liquid-disordered phase coexistence regions, which are thought to be of physiological relevance.

The physical state of the lipids in lipid rafts can be described by the concept of the liquid-ordered (l_o) phase. The liquid-ordered (l_o) phase is explained as an intermediate between the gel and fluid state, in which the acyl chains are still stretched (i.e., ordered) but lack a hexagonal lateral arrangement of the molecules and show fast diffusion (i.e., liquid) [Ipsen 1987]. For pure lipids, both these properties change simultaneously upon melting from the gel (i.e., solid ordered, s_o) to the fluid (liquid disordered, l_d) phase, but both properties can be decoupled in the presence of cholesterol. It has been predicted theoretically that a l_o phase can coexist in equilibrium with a l_d one [Ipsen 1987, Ipsen 1989, Mouritsen 1994, Nielsen 2000]. At high cholesterol content of 30 mol % and more, the gel phase is typically abolished in favor of a l_o phase, which is then transformed into a l_d phase with increasing temperature. This applies to 1, 2-dipalmitoyl-*sn*-glycero-3-phosphocholine (DPPC)-cholesterol (Chol) [Ipsen 1987, Ipsen 1989, Vist 1990, Sankaram 1991], 1-palmitoyl-2-oleoyl-*sn*-glycero-3-phosphocholine (POPC)-Chol [Thewalt 1992], and 1-palmitoyl-2-petroselinoyl-sn-glycero-3 phosphocholine (PPetPC)-Chol [Miao 2002,

Nielsen 2000], and a similar behavior has also been found for palmitoyl SM-Chol [Estep 1979]. In our study, the temperature and pressure dependent phase behavior and fluidity of such canonical lipid raft systems consisting of POPC/SM/Chol mixtures has been explored by using X-ray reflectivity. Besides X-ray reflectivity we also applied thermodynamic methods to detect temperature dependent phase changes, DSC and PPC. The latter is a rather new tool that measures the heat consumed or released by the sample after sudden small pressure jumps of a few bar, yielding precise values of the apparent coefficient of thermal expansion of the lipid bilayer [Heerklotz 2002b, Ravindra 2003].

Additionally, we incorporated a linear polypeptide antibiotic, gramicidin D, into these model raft systems and explored its effect on the temperature and pressure dependent phase behavior of the heterogeneous lipid matrix. Gramicidin is capable of transporting ions through biological membranes [Wallace 1990]. Naturally occurring gramicidin D contains approximately 80-85% of gramicidin A, 6-7% of gramicidin B, and 5-14% of gramicidin C. Gramicidin A is a linear polypeptide with the sequence formyl-L-Val-Gly-L-Ala-D-Leu-L-Ala-D-Val-L-Val-D-Val-(L-Trp-D-Leu)$_3$-L-Trp-ethanolamide [Sarges 1965, Wallace 1990]. Either phenylalanine or tyrosine replaces tryptophan at position 11 in case of gramicidin B and gramicidin C, respectively. The primary sequence of gramicidin consists of 15 amino acid residues of alternative L and D chirality, and all side-chains are non polar. As a consequence, the peptide is able to adopt conformations of β-helices, which would be unacceptable for an all L-amino acid peptide. The helices can be right or left handed and they can differ in the number of amino acid residues per turn and hence in length and diameter [Wallace 1990]. A common form is the head-to-head dimer of two right-handed single-stranded β-helices. The conformation with 6.3 residues per turn ($\beta^{6.3}$-helix) is one of the possible active ion channel structures; it has a hydrophobic length of ~24 Å (channel diameter 4 Å) (Fig. 5.32).

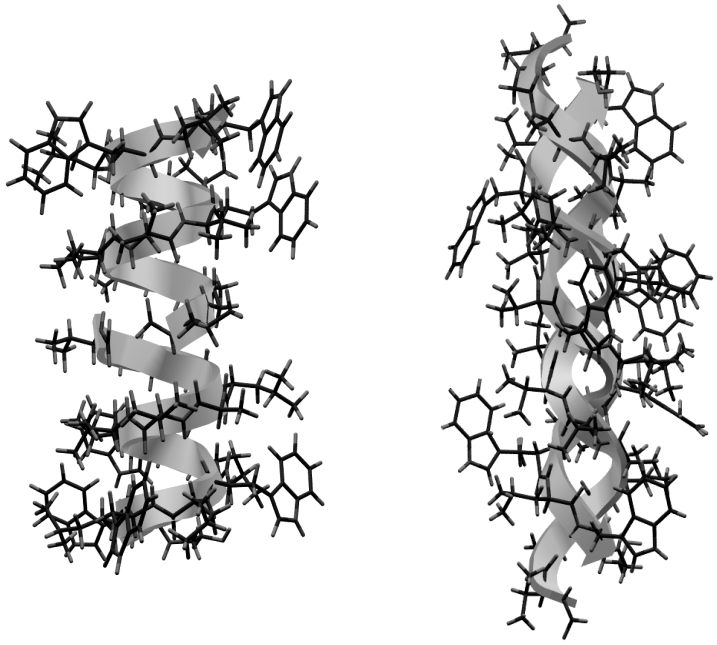

Figure 5.32: Schematic representation showing the polypeptide backbone of a helical dimer (left) and double-helical (right) form of gramicidin.

A further form is the left-handed antiparallel double stranded $\beta^{5.6}$-helix, being approximately 31 Å long (Fig. 5.32), which has been observed in particular organic solvents and long-chain or gel phase lipid bilayer systems [Wallace 1990, Zein 2000].

5.4.1 X-ray Reflectivity Measurements

The X-ray reflectivity measurements were performed at the wiggler beamline (W1.1) of the DORIS storage ring, Deutsche synchrotron (DESY), Hamburg, Germany. The X-rays used were of 10.5 keV energy (wavelength, λ, of 1.18 Å). The thermotropic phase behavior of the ternary mixture of POPC/SM/Chol (2:1:1) of concentration 20 mg/mL spin coated at 3000 rpm on silicon substrate was determined by keeping the sample in a humidity and temperature controlled sample cell as described previously (section 4.8) in this thesis. The measurements were performed over a temperature

range from 11 to 77 °C. Reflected intensity versus Q (momentum transfer vector) plots is shown in Figure 5.33.

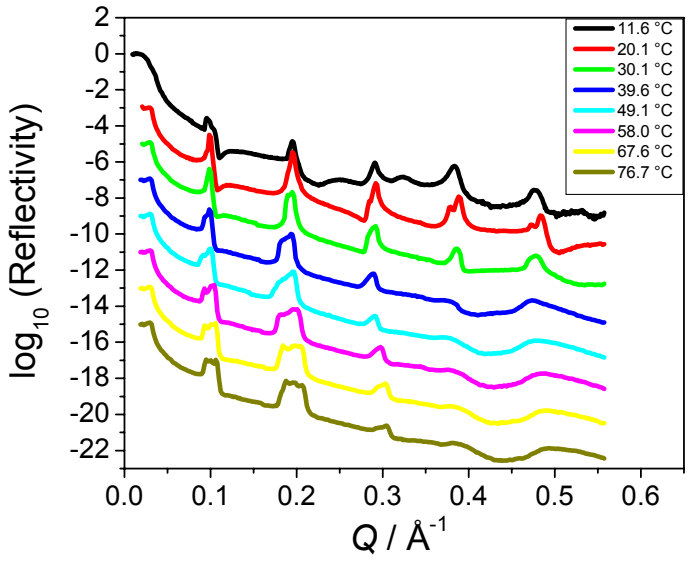

Figure 5.33: X-ray reflectivity measurements of lipid raft mixtures POPC/SM/Chol (2:1:1) prepared from lipid solutions at a concentration of 20 mg/mL by spin coating at 3000 rpm. All the curves are measured at different temperatures at 100% RH. The curves are shifted vertically for clarity.

The positions of Bragg reflections were analyzed to determine the topology of the lipid mesophases and the lamellar repeat distances of the corresponding structures. X-ray reflectivity curves of the three component system POPC/SM/Chol (2:1:1) from ~11 °C to 77 °C are depicted in Figure 5.33. The lamellar repeat distance, d, as obtained from Bragg reflections are displayed as a function of temperature in Figure 5.34. Different lattice constants were observed at each temperature, which indicates the coexistence of lamellar phases. The lamellar repeat distance, d, were obtained from the first order peaks of the reflectivity curves at all the temperatures studied expect for the reflectivity curves measured at ~20 and 30 °C. At ~20 °C, d is calculated from the third and fourth order Bragg peaks and at ~30 °C d is calculated from second order Bragg peak where the two peak structure is more pronounced.

According to the phase diagram of the ternary system POPC/SM/Chol as given in de Almeida et al., [de Almeida 2003], this raft mixture (2:1:1) which contains more fluidizing lipid POPC shows a large binary coexistence region of liquid disordered (l_d) and liquid-ordered (l_o) domains.

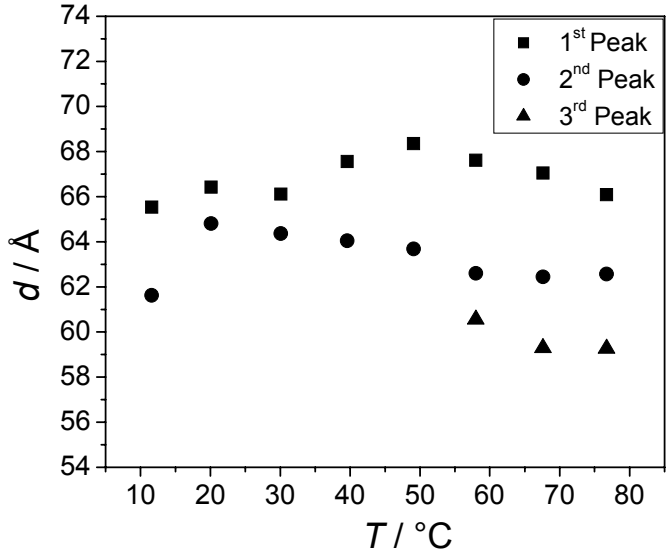

Figure 5.34: Temperature dependence of the lamellar repeat unit at 100% RH of lipid raft mixtures POPC/SM/Chol (2:1:1).

It is clearly seen from Figure 5.33 that the Bragg reflections are resolved into two or three peaks over the whole temperature range studied and indicates the coexistence of phases, such as the l_o+l_d phases. The lamellar repeat distance, *d*, is decreased by ~8 Å overall at ~77 °C probably due to the dominating l_d phase in the two phase l_o+l_d coexistence region.

5.4.2 Differential Scanning and Pressure Perturbation Calorimetry (DSC/PPC)

Additional DSC and PPC studies were carried out from 5 to 95 °C at different sample compositions of ternary raft mixtures. Figure 5.35A shows PPC and DSC curves of lipid vesicles in buffer solution (150 mM NaCl, 100 mM sodium phosphate in H_2O,

pH 7.4) composed of an equimolar ratio of the lipid mixture POPC/SM/Chol. The DSC and PPC data reveal a transition between 5 and 50-65 °C with a broad maximum appearing at ~20 °C. As already discussed by Heerklotz [Heerklotz 2002a], the interpretation of such a broad peak is not straightforward. According to the FT-IR and SAXD data [Nicolini et al., in press], this broad peak corresponds to the continuous transition from the $l_d+l_o+s_o$ three phase region to the l_o+l_d two-phase coexistence region, reaching an overall l_d state above about 55 °C.

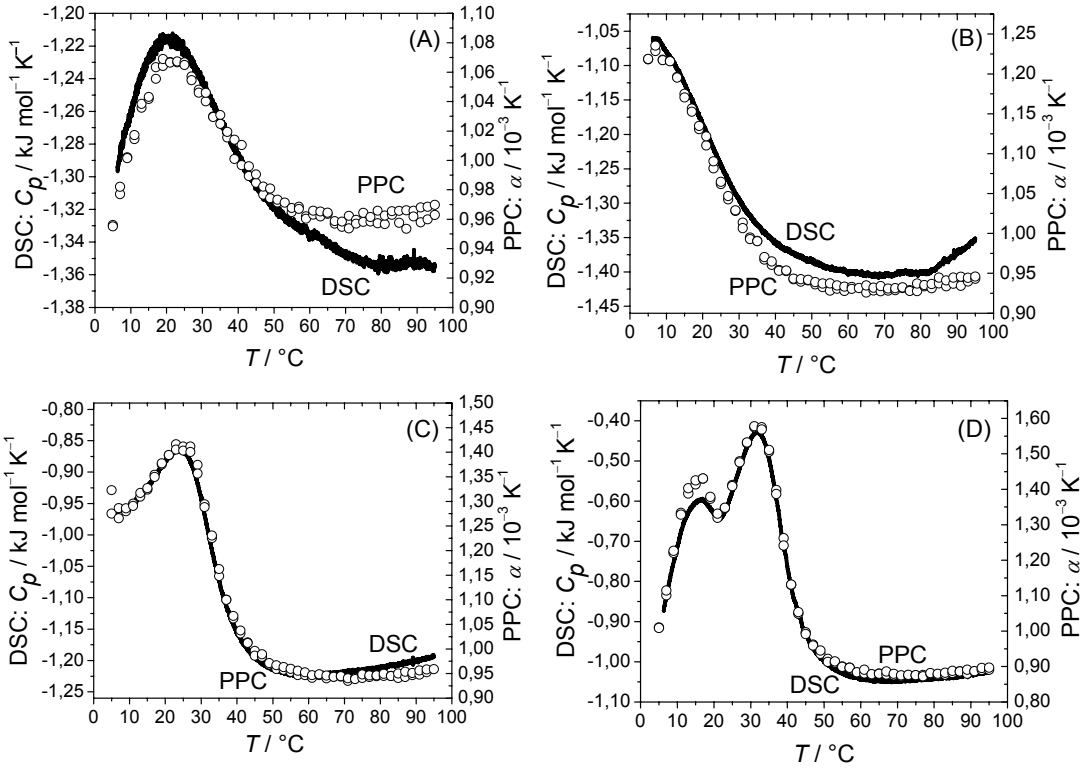

Figure 5.35: (A) The heat capacity C_p (DSC curve, left axis, solid line) and temperature dependence of the thermal expansion coefficient α (PPC curve, right axis, with ○) of a lipid raft mixture of the composition POPC/SM/Chol (1:1:1) in phosphate buffer. (B), (C) and (D) correspond to DSC and PPC curves of the molar ratio 2:1:1, 3:3:1 and 2.5:6.5:1 of POPC/SM/Chol, respectively.

An integration of the DSC and PPC peaks to determine an overall enthalpy change (ΔH) and volume change (ΔV), respectively, for this sample is hampered by the problem of computing a realistic baseline in the low temperature region.

Figure 5.35B displays the data for the 2:1:1 POPC/SM/Chol mixture. For this lipid mixture, which contains more fluidizing lipid POPC, the overall fluid phase is reached already at about 40 °C. The DSC and PPC data of the 3:3:1 and 2.5:6.5:1 lipid mixture, having an increasing SM content (which has a strong ordering effect on the acyl chains) are displayed in Figures 5.35C and 5.35D, respectively. The maxima due to the $l_d+l_o+s_o$ to l_o+l_d transition appear at 25 °C and 32 °C for the 3:3:1 and 2.5:6.5:1 lipid mixtures, respectively. For the latter mixture, with a concentration of more than 40 mol% SM, a pretransitional peak is visible, which is probably due to the transition from an overall ordered l_o+s_o to $l_d+l_o+s_o$ transition. Interestingly, for all lipid mixtures, the overall fluid-like, liquid-disordered state is reached in a rather similar temperature region of about 40-55 °C.

Table 5.7: PPC data of ternary raft mixtures (POPC/SM/Chol) at different molar ratios

POPC/SM/Chol	Integration range (°C)	T_m (°C)	$\Delta V/V$ (%)	$T_{1/2}$ (°C)
1:1:1	5-55	19.02	0.32±0.03	27.9
3:3:1	5-45	27.00	0.51±0.04	15.9
2.5:6.5:1	5-45	33.02	1.28±0.03	27.9
2.5:6.5:1(1^{st} Peak)	5-31	13.01	0.31±0.02	10.01
2.5:6.5:1(2^{nd} Peak)	11-45	33.02	0.80±0.05	14.01

The relative volume changes $\Delta V/V$ at the l_o+s_o to $l_d+l_o+s_o$ and the $l_d+l_o+s_o$ to l_d+l_o transitions are of the order of 0.3 % and 0.8 %, respectively, as listed in Table 5.7. The corresponding heat capacity changes for these transitions amount 15 and 10 kJ/mol, respectively. For comparison, the relative volume and enthalpy changes at the gel to fluid transition of phospholipid bilayers are much larger. For simple, one-component phospholipid membranes undergoing a melting transition, changes in enthalpy by 20-40 kJ/mol and in volume by about 3-4 % are reported [Cevc 1993, Böttner 1994].

5.4.3 Comparison of DSC and PPC Data of Ternary Raft Mixtures Containing an Equimolar Mixture of POPC/SM/Chol and DOPC/SM/Chol

The DSC and PPC studies have also been performed on an equimolar mixture of DOPC/SM/Chol to explore the effect of lipid acyl chain length and unsaturation on the phase behavior of the raft mixtures investigated.

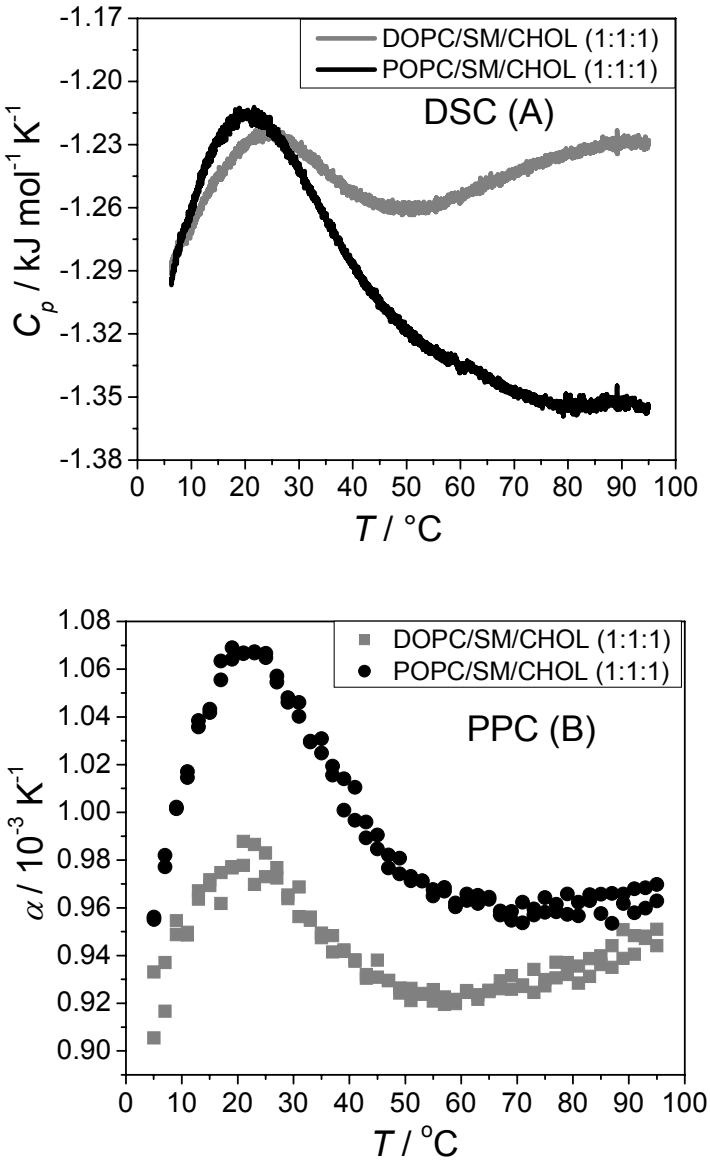

Figure 5.36: (A) the heat capacity C_p (DSC curve, left panel, solid line) of POPC/SM/Chol (1:1:1) (black curve) and DOPC/SM/Chol (1:1:1) (grey curve). (B) Temperature dependence of the thermal expansion coefficient α (● and ■), of lipid raft mixtures of the composition POPC/SM/Chol (1:1:1) (●) and DOPC/SM/Chol (1:1:1) (■) measured in phosphate buffer at pH 7.4.

The comparison between an equimolar mixture of DOPC/SM/Chol and POPC/SM/Chol is depicted in Figure 5.36. It can be clearly seen from the DSC and PPC curves of DOPC/SM/Chol (Fig. 5.36) that there is a shift in the maximum of the $l_d+l_o+s_o$ to l_d+l_o phase transition, which is ~4 °C higher than that of the POPC/SM/Chol mixture, and the l_d phase is reached at a relatively low temperature of about 40 °C rather than at ~50 °C in the case of the POPC containing raft mixture. This could be attributed to the different chain melting temperature of DOPC (two *cis* double bonds, T_m = -20 °C) and POPC (one *cis* double bond, T_m = -5 °C) indicating that DOPC has a more disordering tendency than POPC. Hence, the l_d+l_o compositional difference should be more pronounced in DOPC than in POPC containing membranes. The relative volume changes $\Delta V/V$ of the DOPC/SM/Chol mixture at the $l_d+l_o+s_o$ three phase region to l_d+l_o two phase coexistence region is of the order of 0.27 ± 0.03%.

5.4.4 The Effect of Gramicidin D Incorporation

The effect of incorporating 5 mol% GD on the temperature dependence of 1:1:1 POPC/SM/Chol mixture is shown in Figures 5.37.

Addition of the polypeptide leads to a more broader phase coexistence region over the whole temperature range covered and there is a shift in the transition temperature of the $l_d+l_o+s_o$ to l_d+l_o phase coexistence region. According to the ^{2}H-NMR, FTIR and fluorescence spectroscopic studies [Zein 2000, Eisenblätter 2005, Periasamy et al., in press] addition of the polypeptide increases the overall order parameter profile in the l_o+l_d two-phase coexistence regions, probably by selectively partitioning into l_d domains. The PPC data of POPC/SM/Chol with 5 mol% GD reveals the relative volume changes $\Delta V/V$ at the $l_d+l_o+s_o$ to l_o+l_d transition of the order of 0.27 ± 0.03%. Apart from that, no markedly different phase behavior is observed with incorporation of 5 mol% GD.

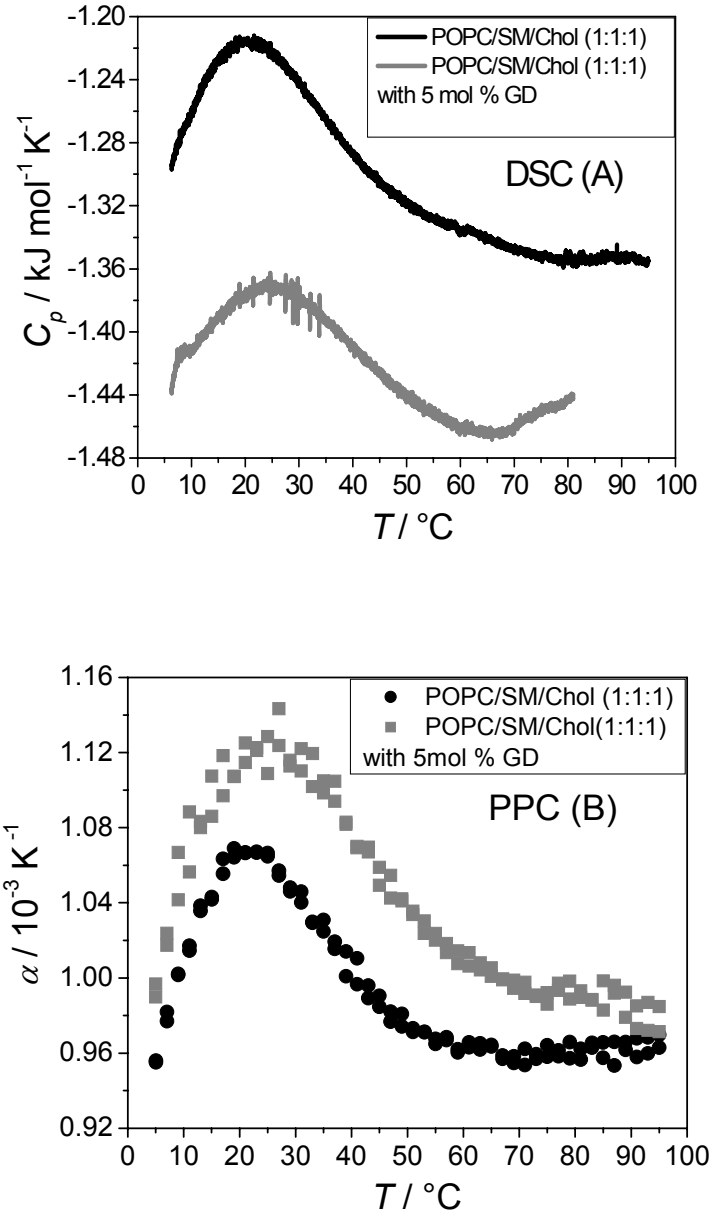

Figure 5.37: (A) DSC and (B) PPC curve of the lipid mixture POPC/SM/Chol 1:1:1 without and with addition of 5 mol% GD.

In these studies, the thermodynamic parameters (ΔH, $\Delta V/V$) of the ternary raft mixtures (POPC/SM/Chol) have been derived by DSC and PPC techniques. Interestingly, it has been found that the liquid-disordered/liquid-ordered (l_d+l_o) phase coexistence region extends over a very wide temperature range of about 50 °C.

6 Summary

In this thesis, highly oriented multilamellar lipid membranes in the state of full hydration and at partial hydration on planar solid supports (silicon wafers) have been investigated using X-ray reflectivity. Artificial lipid membranes were prepared by the spin coating and spreading by organic solution methods. The spreading by the organic solution method gives thick stacks of lipid membranes in hundreds where the control of the number of deposited bilayers is difficult. Advantageously, by the spin coating procedure, one can vary the number of deposited bilayers depending upon the concentration of the lipid and the rotating frequency of the substrate.

As an essential requirement for investigation of solid supported lipid bilayers, the design and construction of a temperature and humidity controlled sample cell was accomplished successfully. One of the important objectives was to study the structural properties of solid supported model biomembranes, a second one was to get insight into the mesophasic behavior of the lipid membranes as a function of temperature and relative humidity. With the new sample cell, the temperature and humidity controlled X-ray reflectivity measurements were carried out first on DPPC membranes. From the position of the Bragg reflections, the lamellar repeat distance *d* (thickness of the lipid bilayer and water layer) was calculated and the electron density profile was determined by fitting the reflectivity data using the Parratt program. The results obtained for DPPC were in good agreement with literature data, indicating that the new sample cell could control the relative humidity and temperature at the desired level. The design and construction of the cell, meeting the desired requirements, was significant towards carrying out studies on various other model lipid biomembrane systems.

X-ray reflectivity measurements on the polar lipid fraction E (PLFE) of archaebacterial lipids, isolated from *Sulfolobus acidocaldarius*, were carried out at the Wiggler beamline W1.1 of HASYLAB/DESY in Hamburg, Germany. The reflectivity data on PLFE samples showed lamellar Bragg reflections over the temperature range of 10 to 70 °C with partial hydration and at full hydration. A lamellar repeat distance *d* of 57.6 Å has been determined at a temperature of about 27 °C and at ~97% relative

humidity (RH). At ~97% RH, a lamellar to lamellar phase transition at ~36 °C and, interestingly, at full hydration a lamellar to cubic phase transition was detected at ~49.8 °C. The reciprocal spacings observed correspond to the coexistence of the inverse bicontinous cubic phases Q_{II}^{D} and Q_{II}^{P} with lattice constants of 117 Å and 151 Å, respectively. Differential Scanning Calorimetry (DSC) and Pressure Perturbation Calorimetric (PPC) techniques were also applied to get further information regarding the phase behavior and thermodynamic properties of PLFE liposomes. DSC and PPC data provide information on membrane packing, enthalpy and volumetric changes. For PLFE multilamellar vesicles (MLVs) derived from cells grown at 65 °C, the first heating scan exhibits an endothermic transition at 43.7 °C and a broad exothermic peak at 85.5 °C. For the PLFE MLVs derived from cells grown at 65 °C, we yield relative volume changes $\Delta V/V$ of ~0.56 % and ΔH=16 kJ/mol for the lamellar to lamellar phase transition. Temperature dependent Fourier-transform Infrared Spectroscopy (FT-IR) measurements were performed to acquire additional information on conformation changes of PLFE MLVs in D_2O. By FT-IR, the lamellar to lamellar phase transition is observed at a temperature of ~38-40 °C.

Studies on two-component DPPC/ergosterol mixtures have been carried out to get valuable information on the lipid membrane organization and domain-size distribution using the X-ray reflectivity and Small-angle Neutron Scattering (SANS) techniques. The lamellar repeat distance (d) of about 70 Å was obtained for the mixture of 16:24 mol% DPPC/ergosterol at 20 °C by X-ray reflectivity measurements. This lamellar repeat distance is higher as compared to 63 Å of pure DPPC membranes at the same temperature. This increase in lamellar repeat unit with incorporation of ergosterol into DPPC membranes may be due to a decrease of the tilt angle in the $L_{\beta'}$ phase or an increase in water layer thickness.

SANS measurements using the H/D contrast variation technique were performed on the system DPPC/ergosterol at selected concentrations and temperatures. From the SANS data, no critical concentration fluctuations or a critical point may be inferred for the temperature/concentration phase space covered. Interestingly, in the gel-fluid two-phase coexistence region, a fractal like scattering behavior is observed. The mass

fractal dimensions (D_m) of ~2.48 and ~2.40 are obtained at 18 mol% and 20 mol% of ergosterol in DPPC MLVs at a temperature of 25 °C and ~38 °C for describing the lateral organisation of the phase-separated lipid mixture in the (s_o+l_o) two phase region. At high concentrations of ergosterol, i.e., at 22 and 24 mol%, and at a temperature of 49.3 and 54.3 °C, respectively, surface fractal dimensions (D_s) of ~2.28 and 1.9 are deduced from the scattering data.

Natural biological membranes consist of many different types of lipids and proteins, which lead to strong membrane heterogeneity and phase separation, called lipid microdomains or "lipid rafts". These lipid rafts play an important role in many biological processes; hence it is important to study their properties such as the lateral membrane organization, phase behavior and their influence on the conformation and activity of membrane proteins/peptides. Towards this aim, we explored the temperature, pressure and concentration dependent phase behavior of the canonical model raft mixtures POPC/sphingomyelin/cholesterol using the X-ray reflectivity, DSC and PPC techniques. By X-ray reflectivity, a lamellar repeat distance *d* of the POPC/SM/Chol (2:1:1) mixture of ~65 Å is obtained, which decreases to ~59 Å at 77 °C, where the system is dominated by a liquid-disordered (l_d) phase. DSC and PPC were used to explore the thermodynamic behavior of these lipid raft mixtures. Interestingly, it has been found that liquid-disordered/liquid-ordered phase coexistence regions extend over a very wide temperature range of about 50 °C. The enthalpy change ΔH at the liquid-ordered/solid-ordered l_o+s_o to l_d+l_o+s_o and the l_d+l_o+s_o to l_d+l_o transitions amount 15 and 10 kJ/mol, respectively. The corresponding relative volume changes $\Delta V/V$ revealed by PPC are of the order of 0.3% and 0.8%, respectively. Incorporation of 5 mol% gramicidin D (GD) peptide slightly increases the overall order parameter profile in the l_o+l_d two-phase coexistence region by selectively partitioning into l_d domains.

The studies in this thesis provide valuable information regarding the phase behavior, lateral organization and thermodynamic properties of lipid membranes and will be significant in general for the understanding of the structure-property relationships of a wide variety of related systems.

7 Zusammenfassung

In dieser Arbeit wurden hochgradig orientierte, multilamellare Lipidmembranen, welche sich auf einer planaren Festkörperoberfläche (Siliziumplättchen) befanden, im Zustand vollständiger bzw. teilweiser Hydratation mittels Röntgenreflektometrie untersucht. Dabei wurden die Lipidmembranen mit der sog. *spin coating*-Technik und durch Spreitung organischer Lipidlösungen erzeugt. Mit letzterer Methode werden Stapel aus hunderten von Doppelmembranen erhalten. Eine Kontrolle der so erzeugten Schichtzahl ist schwierig. Die *spin coating*-Technik hingegen erlaubt eine Variierung der Schichtanzahl durch Einstellung der Lipidkonzentration oder Änderung der Drehfrequenz des Silizium-Substrats.

Um die auf dem Festkörper erzeugten Lipidmembranen unter kontrollierten Bedingungen zu untersuchen, wurde eine Messzelle erfolgreich entwickelt und konstruiert, welche die Einstellung definierter Temperaturen und Luftfeuchtigkeiten erlaubte. Ein Ziel dieser Arbeit war es einerseits, Modellbiomembranen auf Festkörperoberflächen zu untersuchen, andererseits das mesoskope Phasenverhalten der Lipidmembranen als Funktion von Temperatur und relativer Feuchtigkeit zu charakterisieren. Daher wurden zunächst die temperatur- und feuchtigkeitsabhängigen Messungen mit der neuen Zelle an DPPC-Membranen durchgeführt. Aus der Position der gemessenen Bragg-Signale kann die Dicke einer lamellaren Schicht d (d.h. die Dicke der Doppelmembran inklusive einer Wasserschicht) berechnet werden. Durch Anpassung einer Reflexionskurve kann mittels des Programms Parratt das Profil der Elektronendichte bestimmt werden. Die für DPPC gewonnenen Daten stehen in Einklang mit Literaturwerten und zeigen, dass mit der neu entwickelten Messzelle die gewünschten Temperaturen und Luftfeuchtigkeiten eingestellt werden konnten. Somit wurde die Grundlage für die Vermessung anderer Modell-Lipidmembranen gelegt.

Röntgenreflektometrische Messungen wurden an Membranen der polaren Lipidfraktion E (PLFE) aus dem thermoacidophilen Archaebakterium *Sulfolobus Acidocaldarius* an der *Wiggler-beamline* W1.1 des HASYLAB/DESY in Hamburg durchgeführt. Die Reflektivitätsdaten der PLFE-Proben wiesen lamellare Bragg-Reflexe im Temperaturbereich von 10 bis 70 °C unter partieller und unter voller

Hydratation auf. Eine Gitterkonstante *d* von 57,6 Å wurde bei einer Temperatur von 27 °C und ~ 97 % relativer Feuchtigkeit (RH) festgestellt. Bei einer RH von 97 % und etwa 36 °C wurde ein Übergang in eine andere lamellare Phase festgestellt. Interessanterweise konnte bei ~ 49,8 °C und voller Hydratation ein Übergang von einer lamellaren in eine kubische Phase bestimmt werden. Die beobachteten reziproken Netzebenenabstände korrelieren mit der Koexistenz zweier inverser, bikontinuierlicher kubischer Phasen Q_{II}^{D} und Q_{II}^{P} mit Gitterkonstanten von 117 und 151 Å. Mittels der mikrokalorimetrischen Methoden DSC (*Differential Scanning Calorimetry*) und PPC (*Pressure Pertubation Calorimetry*) wurden weitere Informationen bezüglich des Phasenverhaltens und der Konformation der PLFE-Liposomen erhalten. DSC und PPC erlauben Rückschlüsse auf die Packung sowie die enthalpischen und volumetrisches Eigenschaften von Membranen. Für multilamellare Vesikel (MLV) aus PLFE, das aus Zellen, die bei 65 °C heranwuchsen, erhalten wurde, konnte in der DSC-Kurve ein endothermes Signal bei 43,7 °C und ein breites, exothermes Signal bei 85,5 °C gefunden werden. Für ersteres Signal, das den Übergang von lamellarer zu lamellarer Phase anzeigt, konnte eine relative Volumenänderung von 0,56 % und eine Enthalpiedifferenz ΔH = 16 kJ/mol ermittelt werden. Temperaturabhängige Messungen mittels Fourier-Transform-Infrarotspektroskopie (FT-IR) wurden durchgeführt, um konformelle Änderungen und das Phasenverhalten der PLFE-MLV in D_2O zu untersuchen. Mittels FT-IR konnte der Übergang von lamellarer zu lamellarer Phase bei einer Temperatur von ca. 38-40 °C gefunden werden, was in guter Übereinstimmung mit den Werten der DSC- und PPC- Messungen ist, welche an den PLFE-MLV in reinem Wasser ermittelt wurden.
Es wurden zudem Untersuchungen an dem Zwei-Komponenten-System DPPC/ Ergosterol mittels Röntgenbeugung und Kleinwinkel-Neutronen-Streuung (SANS) durchgeführt, um Informationen über die Organisation der Lipidmembranen und die Verteilung der Domänengrößen zu erhalten. Für eine Mischung mit einem Molverhältnis von 16:24 (DPPC/Ergosterol) bei 20 °C konnte die Gitterkonstante *d* mittels Röntgenreflektometrie zu etwa 70 Å bestimmt werden. Diese ist größer als die Gitterkonstante reiner DPPC-Membranen (63 Å), welche ebenfalls untersucht

wurden. Der Anstieg der Gitterkonstante beim Einbau von Ergosterol in DPPC-Membranen kann auf eine Reduktion des Neigungswinkels der Acylketten order eine zunahme der interlamellaren wasserchicht-Dicke zurückgeführt werden, welche durch Ergosterol induziert wird.

SANS-Messungen unter Nutzung der H/D-Kontrastvariationstechnik wurden an dem DPPC/Ergosterol-System bei ausgesuchten Konzentrationen durchgeführt. Auf Basis dieser Daten konnten keine kritischen Konzentrationsfluktuation und kein kritischer Punkt in dem überstrichenen Temperatur/Konzentrationsbereich gefunden werden. Interessanterweise konnten in der Zweiphasen-Koexistenzregion gel/flüssig fraktal-ähnliches Strukturen beobachtet werden. Es wurde ein Massenfraktal mit einer Dimension (D_m) von ~ 2,48 und ~ 2,40 bei 18 mol-% bzw. 20-mol% Ergosterol in DPPC-MLV bei Temperaturen von 25 °C und ~ 38 °C gefunden. Bei hohen Ergosterolkonzentrationen, d.h. bei 22 und 24 mol-% und einer Temperatur von 49,3 bzw. 54,3 °C, liegt ein Oberflächenfraktal mit Dimensionen (D_s) von ~ 2,28 und 1,9 vor.

Natürliche biologische Membranen bestehen aus vielen unterschiedlichen Arten von Lipiden und Proteinen, welche zu einer starken Heterogenität der Membranen und einer Phasentrennung führen, welche als Mikrodomänen bzw. „*lipid rafts*“ bezeichnet werden. Diese *lipid rafts* spielen vermutlich eine wichtige Rolle in vielen biologischen Prozessen; daher ist eine Untersuchung des lateralen Aufbaus der Membranen, des Phasenverhaltens und ihres Einflusses auf die Konformation und die Aktivität von Membranproteinen und –peptiden sehr wichtig. Hinsichtlich dieses Ziels wurde das temperatur-, druck- und konzentrationsabhängige Verhalten einer ternären Mischung aus POPC, Sphingomyelin und Cholesterol mittels Röntgenreflektometrie, DSC und PPC untersucht. Die Gitterkonstante *d* der POPC/Sphingomyelin/Cholesteol (2:1:1)-Mischung konnte mittels Röntgenreflektometrie zu ~ 65 Å bestimmt werden, welche bei 77 °C auf ~ 59 Å abnimmt, wobei sich das gesamte System in einem flüssig-ungeordneten Zustand (l_d) befindet. Mittels DSC und PPC wurde das thermodynamische Verhalten dieser *lipid rafts*-Mischungen untersucht. Interessanterweise konnte festgestellt werden, dass sich

die Koexistenzregion der flüssig-ungeordneten und flüssig-geordneten Phase über einen sehr breiten Temperaturbereich von etwa 50 °C erstreckt. Die Änderung der Enthalpie ΔH an dem Übergang von flüssig-geordnet/fest-geordnet (l_o+s_o) zu l_d+l_o+s_o sowie von l_d+l_o+s_o zu l_d+l_o beträgt 15 bzw. 10 kJ/mol. Die entsprechenden relativen Volumenänderungen $\Delta V/V$ konnten mittels PPC zu etwa 0,3 % und 0,8 % bestimmt werden. Der Einbau von 5 mol-% Gramicidin D (GD) erhöht den Ordnungsparameter leicht in der Zweiphasen-Koexistenzregion l_o+l_d durch einen selektive Einbau in die l_d-Domänen.

Die Untersuchungen in dieser Arbeit geben wertvolle Informationen über das Phasenverhalten, die laterale Organisation und die thermodynamischen Eigenschaften von Lipid-Membranen und sind wichtig für ein generelles Verständnis der Beziehung zwischen Struktur und Eigenschaften ähnlicher Systeme.

8 References

Albon, N., J. M. Sturtevant, *Proc. Natl. Acad. Sci. U.S.A.* **75** (1978) 2258-2260.

Als-Nielsen, J., D. Jacquemain, K. Kjaer, M. Lahav, F. Leveiller, L. Leiserowitz, *Phys. Rep.* **246** (1994) 251-313.

Anderson, T. G., H. M. McConnell, *Biophys. J.* **81** (2001) 2774-2785.

Anderson, R. G. W., K. Jacobson, *Science* **296** (2002) 1821-1825.

Anthony, F. H., R. L. Biltonen, E. Freire, *Anal. Biochem.* **116** (1981) 161-167.

Arora, A., H. Raghuraman, A. Chattopadhyay, *Biochem. Biophys. Res. Commun.* **318** (2004) 920-926.

Bagatolli, L., E. Gratton, T. P. Khan, P. L.-G. Chong, *Biophys. J.* **79** (2000) 416-425.

Bagnat, M. S., A. Shevchenko, K. Simons, *Proc. Natl. Acad. Sci. U.S.A.* **97** (2000) 3254-3259.

Bahr, D., *Phys. Rev. B* **47** (1993) 4385-4393.

Bayerl, T. M., M. Bloom, *Biophys. J.* **58** (1990) 357-362.

Born, M., E. Wolf, Principles of optics, Pergamon press, Oxford, (1989).

Böttner, M., R. Winter, *Biophys. J.* **65** (1993) 2041-2046.

Böttner, M., D. Ceh, U. Jakobs, R. Winter, *Z. Phys. Chem.* **184** (1994) 205-218.

Brian, A. A., H. M. McConnell, *Proc. Natl. Acad. Sci. U.S.A.* **81** (1984) 6159-6163.

Cevc, G. (Ed.), Phospholipids Handbook, Marcel Dekker, New York, (1993).

Chang, E. L., *Biochem. Biophys. Res. Commun.* **202** (1994) 673-679.

Chapman, D., R. M. Williams, B. D. Ladbrooke, *Chem. Phys. Lipids*. **1** (1967) 445-475.

Chong, P. L.-G., M. Zein, T. P. Khan, R. Winter, *J. Phys. Chem. B* **107** (2003) 8694-8700.

Chong, P. L.-G., R. Ravindra, M. Khurana, V. English, R. Winter, *Biophys. J.* **89** (2005) 1841-1849.

Cordeiro, Y., J. Kraineva, R. Ravindra, L. M. T. R. Lima, M. P. B. Gomes, D. Foguel, R. Winter, J. L. Silva, *J. Biol. Chem.* **279** (2004) 32354-32359.

Crook, S. J., J. M. Boggs, A. I. Vistnes, K. M. Koshy, *Biochemistry* **25** (1986) 7488-7494.

Czeslik, C., J. Erbes, R. Winter, *Europhys. Lett.* **37** (1997) 577-582.

Daillant, J., A. Gibaud, (Springer-Verlag, Berlin, 1999).

Damay, P., F. Leclercq, P. Chieux, *J. Phys. Chem.* **88** (1984) 3734-3740.

de Almeida, R. F. M., A. Fedorov, M. Prieto, *Biophys. J.* **85** (2003) 2406-2416.

de Kruijff, B., R. A. Demel, L. L. van Deenen, *Biochim. Biophys. Acta.* **255** (1972) 331-347.

de Rosa, M., A. Gambacorta, A. Gliozzi, *Microbiol. Rev.* **50** (1986) 70-80.

de Rosa, M., A. Gambacorta, *Prog. Lipid Res*. **27** (1988) 153-175.

Dietrich, L. A., Z. N. Bagatolli, N. L. Volovyk, N. L. Thompson, M. Levi, K. Jacobson, E. Gratton, *Biophys. J.* **80** (2001) 1417-1428.

Dzwolak, W., R. Ravindra, J. Lendermann, R. Winter, *Biochemistry* **42** (2003) 11347-11355.

Edidin, M., *Ann. Rev. Biophys. Biomol. Struct.* **32** (2003) 257-283.

Elferink, M. G. L., J. G. de Wit, R. Demel, A. J. M. Driessen, W. N. Konings, *J. Biol. Chem.* **267** (1992) 1375-1381.

Elferink, M. G. L., J. G. de Wit, A. J. M. Driessen, W. N. Konings, *Eur. J. Biochem.* **214** (1993) 917-925.

Elferink, M. G. L., J. G. de Wit, R. Demel, A. J. M. Driessen, W. N. Konings, *Biochem. Biophys. Acta.* **1193** (1994) 247-254.

Estep, T. N., D. B. Mountcastle, Y. Barenholz, R. L. Biltonen, T. E. Thompson, *Biochemistry* **18** (1979) 2112-2117.

Fragneto, G., T. Charitat, F. Graner, K. Mecke, L. Perino-Gallice, E. Bellet-Amalric, *Europhys. Lett.* **53** (2001) 100-106.

Gabriel, J. L., P. L.-G. Chong, *Chem. Phys. Lipids.* **105** (2000) 193-200.

Gulik, A., V. Luzzati, M. de Rosa, A. Gambacorta, *J. Mol. Biol.* **182** (1985) 131-149.

Gulik, A., V. Luzzati, M. de Rosa, A. Gambacorta, *J. Mol. Biol.* **201** (1988) 429-435.

Harder, T., Philos. *Trans. R. Soc. Lond. B*. **358** (2003) 863-868.

Heerklotz, H., *Biophys. J.* **83** (2002a) 2693-2701.

Heerklotz, H., J. Seelig, *Biophys. J.* **82** (2002b) 1445-1452.

Holy, V., (Springer-Verlag, Berlin, 1999)

Hsueh, Y. W., K. Gilbert, C. Trandum, M. Zuckermann, J. Thewalt, *Biophys. J.* **88** (2005) 1799-1808.

Huang, F., X-ray reflectivity studies of thin films, Internal report (2005).

Ipsen, J. H., G. Karlstrom, O. G. Mouritsen, H. Wennerstrom, M. J. Zuckermann, *Biochem. Biophys. Acta.* **905** (1987) 162-172.

Ipsen, J. H., O. G. Mouritsen, M. J. Zuckermann, *Biophys. J.* **56** (1989) 661-667.

Israelachvili, J. N., Intermolecular & surface forces, Academic Press, London, 2.ed. (1992).

Janiak, M. J., D. M. Small, G. G. Shipley, *Biochemistry* **15** (1976) 4575-4580.

Janiak, M. J., D. M. Small, G. G. Shipley, *J. Biol. Chem.* **254** (1979) 6068-6078.

Janosch, S., C. Nicolini, B. Ludolph, C. Peters, M. Volkert, T. L. Hazlet, E. Gratton, H. Waldmann, R. Winter, *J. Am. Chem. Soc.* **126** (2004) 7496-7503.

Kalb, E., S. Frey, L. K. Tamm, *Biochim. Biophys. Acta.* **1103** (1992) 307-316.

Kanichay, R., L. T. Boni, P. H. Cooke, T. K. Khan, P. L.-G. Chong, *Archaea* **1** (2003) 175-183.

Khan, T. K., P. L.-G. Chong, *Biophys. J.* **78** (2000) 1390-1399.

Knoll, W., K. Ibel, E. Sackmann, *Biochemistry* **20** (1981) 6379-6383.

Koenig, B. W., S. Krueger, W. J. Orts, C. F. Majkrzak, N. F. Berk, J. V. Silverton, K. Gawrisch, *Langmuir* **12** (1996) 1343-1350.

Komatsu, H., P. L.-G. Chong, *Biochemistry* **37** (1998) 107-115.

Koynova, R., M. Caffrey, *Biochim. Biophys. Acta.* **1376** (1998) 91-145.

Landwehr, A., R. Winter, *Phys. Chem.* **98** (1994) 214-218.

Lide, D. R., (Ed.), Handbook of Chemistry and Physics, CRC Press, New York, 76.ed, (1995)

Lin, L.-N., J. F. Brandts, J. M. Brandts, V. Plotnikov, *Anal. Biochem.* **302** (2002) 144-160.

Lo, S.-L., E. L. Chang, *Biochem. Biophys. Res. Commun.* **167** (1990) 238-243.

London, E., D. A. Brown, *Biochem. Biophys. Acta.* **1508** (2000) 182-195.

Luzzati, V., F. Husson, *J. Cell. Biol.* **12** (1962) 207-219.

Mabrey, S., J. M. Sturtevant, *Proc. Natl. Acad. Sci. USA.* **73** (1976) 3862-3866.

Mantsch, H. H., R. N. McElhaney, *Chem. Phys. Lipids* **57** (1991) 213-226.

Mason, J. T., *Methods Enzymol.* **295** (1998) 468-494.

Mason, R. P., T. N. Tulenko, R. F. Jacob, *Biochim. Biophys. Acta* **1610** (2003) 198-207.

McConnell, H. M., T. H. Watts, R. M. Weis, and A. A. Brian, *Biochim. Biophys. Acta. 864* (1986) 95-106.

Mennicke, U., T. Salditt, *Langmuir* **18** (2002) 8172-8177.

Miao, L., M. Nielsen, J. Thewalt, J. H. Ipsen, M. Bloom, M. J. Zuckermann, O. G. Mouritsen, *Biophys. J.* **82** (2002) 1429-1444.

Mouritsen, O. G., K. Jorgensen, *Chem. Phys. Lipids.* **73** (1994) 3-25.

Mouritsen, O. G., M. J. Zuckermann, *Lipids* **39** (2004) 1101-1112.

Mukherjee, S., F. R. Maxfield, *Annu. Rev. Cell. Dev. Biol.* **20** (2004) 839-866.

Munro, S., *Cell* **115** (2003) 377-388.

Nagle, J. F., R. Zhang, S.-T. Nagle, W. Sun, H. I. Petrache, R. M. Suter, *Biophys. J.* **70** (1996) 1419-1431.

Nagle, J. F., S. Tristram-Nagle, *Biochim. Biophys. Acta.* **1469** (2000) 159-195.

Nicolini, C., J. Kraineva, M. Khurana, N. Periasamy, S. Funari, R. Winter, *Biochem. Biophys. Acta.* (in press).

Nielsen, M., J. Thewalt, L. Miao, J. H. Ipsen, M. Bloom, M. J. Zuckermann, O. G. Mouritsen, *Europhys. Lett.* **52** (2000) 368-374.

O'Brien, M. A., *J. Sci. Instrum.* **25** (1948) 73-76.

Parratt, L. G., *Physical Rev.* **95** (1954) 359-369.

Periasamy, N., R. Winter, *Biochem. Biophys. Acta.* (in press).

Petrache, H. I., S. T. Nagle, J. F. Nagle, *Chem. Phys. Lipids* **95** (1998) 83-94.

Pike, L. J., *J. Lipid Res.* **44** (2003) 655-667

Plotnikov, V. V., J. M. Brandts, L. N. Lin, J. F. Brandts, *Anal. Biochem.* **250** (1997) 237-244.

Quinn, P. J., *Subcell. Biochem.* **14** (1989) 25-95.

Radhakrishnan, A., T. G. Anderson, H. M. McConnell, *Proc. Natl. Acad. Sci. U.S.A.* **97** (2000) 12422-12427.

Ravindra, R., R. Winter, *Z. Phys. Chem.* **217** (2003) 1221-1243.

Ravindra, R., R. Winter, *ChemPhysChem* **5** (2004) 566-571.

Reis, O., R. Winter, T. W. Zerda, *Biochim. Biophys. Acta* **1279** (1996) 5-16.

Reis, O., R. Winter, *Langmuir* **14** (1998) 2903-2909.

Russell, T. P., *Mat. Sci. Rep.* **5** (1990) 171-271.

Sackmann, E., *Science* **271** (1996) 43-48.

Sankaram, M. B., T. E. Thompson, *Proc. Natl. Acad. Sci. U.S.A.* **88** (1991) 8686-8690.

Sarges, R., B. Witkop, A. V. Gramicidin, *J. Am. Chem. Soc.* **87** (1965) 2011-2020.

Scott, H. L., *Curr. Opin. Struct. Biol.* **12** (2002) 495-502.

Seul, M., M. J. Sammon, *Thin Solid Films* **185** (1990) 287-305.

Silvius, J. R., *Biochim. Biophys. Acta* **1610** (2003) 174-183.

Simons, K., E. Ikonen, *Nature* **387** (1997) 569-572.

Simons, K., D. Toomre, *Nat. Rev. Mol. Cell Biol.* **1** (2000) 31-39.

Simons, K., W. L. C. Vaz, *Ann. Rev. Biophys. Biomol. Struct.* **33** (2004) 269-295.

Singer, S. J., G. L. Nicolson, *Science* **175** (1972) 720-731.

Stewart, R. J., J. M. Boggs, *Biochemistry* **32** (1993) 10666-10674.

Tamm, L. K., H. M. McConnell, *Biophys. J.* **47** (1985) 104-113.

Thewalt, J. L., M. Bloom, *Biophys. J.* **63** (1992) 1176-1181.

Tillack, T.W., M. Wong, M. Allietta, T. E. Thompson, *Biochim. Biophys. Acta* **691** (1982) 261-273.

Tolan, M., (Springer-Verlag, Berlin, 1990).

Tolan, M., W. Press, *Z. Kristallogr.* **213** (1998) 319-336.

van Deenen, L. L. M., *Prog. Chem. Fats Lipids.* **8** (1965) 1-127

Vance., D. E., J. E. Vance, Biochemistry of lipids, lipoproteins and membranes, Elsevier, Amsterdam, 3.ed. (1996).

Vilalta, I., A. Gliozzi, M. Prats, *Eur. J. Biochem.***240** (1996) 181-185.

Vist, M. R., J. H. Davis, *Biochemistry* **29** (1990) 451-464.

Wallace, B. A., *Annu. Rev. Biophys. Chem.* **19** (1990) 127-157.

Wang, S.-L., R. M. Epand, *Chem. Phys. Lipids.* **129** (2004) 21-30.

Wasserman, S. R., T. Yu-Tai, G. M. Whitesides, *Langmuir*.**5** (1989) 1074-1087.

Watts, T. H., and H. M. McConnell, *Annu. Rev. Immunol.* **5** (1987) 461-475.

Winter, R., A. Gabke, C. Czeslik, P. Pfeifer, *Phys. Rev. E* **60** (1999) 7354-7359.

Winter, R., *Biochim. Biophys. Acta* **1595** (2002) 160-184.

Winter, R., R. Köhling, *J. Phys.: Condens. Matter* **16** (2004) S327-S352.

Zabel, H., *Appl. Phys. A* **58** (1994) 159-168.

Zein, M., R. Winter, *Phys. Chem. Chem. Phys.* **2** (2002) 4545-4551.